



**POLITECNICO**  
MILANO 1863

SCUOLA DI INGEGNERIA INDUSTRIALE  
E DELL'INFORMAZIONE

# Calibration of absolute Stimulated Raman Scattering cross-section for quantitative measurements

TESI DI LAUREA MAGISTRALE IN  
PHYSICS ENGINEERING - INGEGNERIA FISICA

Author: **Trezzi Samuele**

Student ID: 224743

Advisor: Prof. Dario Polli

Academic Year: 2024-25



# Abstract

This thesis explores advancements in achieving quantitative measurements in Stimulated Raman Scattering (SRS) microscopy, a technique that builds on the Raman scattering phenomenon to provide high-sensitivity, label-free imaging of molecular vibrations. Conventional microscopy techniques like bright-field and fluorescence microscopy offer spatial resolution and single-molecule sensitivity, yet often lack the chemical specificity and non-invasive nature provided by Raman techniques. While spontaneous Raman scattering offers a label-free approach, its incoherent and weak signal limits its effectiveness. SRS, a type of Coherent Raman Scattering (CRS), enhances Raman signals by synchronizing pump and Stokes laser pulses, allowing for amplified, coherent molecular responses that improve imaging speed, sensitivity, and three-dimensional sectioning capability.

This work starts from the recent introduction of a new SRS cross-section,  $\sigma_{SRS}$ , and focuses particularly on its calibration. To overcome the challenges presented by the small intensity variations typically buried within laser noise, a lock-in amplifier is employed for signal extraction. A key corrective factor for the lock-in measurement, the Filling Factor (FF), is introduced to account for the photodiode bandwidth and laser repetition rate, which becomes crucial when transitioning from arbitrary units to quantitative SRS measurements. This thesis investigates and applies a modified procedure for measuring  $\sigma_{SRS}$ , enabling more accurate and reproducible SRS data, with potential implications for improved chemical imaging across various fields.

**Keywords:** Stimulated Raman Scattering(SRS) microscopy, quantitative measurement, SRS cross-section, lock-in amplifier



## Abstract in lingua italiana

Questa tesi esplora i progressi nell'ottenimento di misurazioni quantitative nella microscopia Raman Stimolata (SRS), una tecnica che si basa sul fenomeno dello scattering Raman al fine di fornire immagini ad alta sensibilità e senza marcatori. Le tecniche di microscopia convenzionali, come la microscopia a campo chiaro e quella a fluorescenza, offrono una buona risoluzione spaziale e la sensibilità fino al livello della singola molecola, ma spesso mancano della specificità chimica e della non invasività tipiche delle tecniche Raman. Sebbene lo scattering Raman spontaneo offra un approccio senza marcatori, il segnale incoerente e debole limita la sua efficacia. L'SRS, un tipo di diffusione Raman coerente (CRS), migliora i segnali Raman sincronizzando gli impulsi laser di pompaggio e Stokes, permettendo risposte molecolari coerenti e amplificate, che aumentano la velocità di imaging, la sensibilità e la capacità di sezionamento tridimensionale.

Questo lavoro parte dall'introduzione recente di una nuova sezione d'urto per SRS,  $\sigma_{SRS}$ , in particolare sulla sua calibrazione. Per affrontare le sfide poste dalle così piccole variazioni di intensità spesso mascherate dal rumore laser, viene impiegato un amplificatore lock-in per l'estrazione del segnale. Un fattore correttivo chiave per le misurazioni lock-in, il Filling Factor (FF), è introdotto per tener conto della larghezza di banda del fotodiode e della frequenza di ripetizione del laser, diventando cruciale nel passaggio da unità arbitrarie a misurazioni quantitative di SRS. Questa tesi esplora e applica una procedura modificata per misurare  $\sigma_{SRS}$ , permettendo di ottenere dati SRS più accurati e riproducibili, con potenziali implicazioni per un imaging chimico migliorato in vari ambiti.

**Parole chiave:** Microscopia Raman scattering stimolato(SRS), misure quantitative, sezione d'urto SRS, amplificatore lock-in



# Contents

<b>Abstract</b>	<b>i</b>
<b>Abstract in lingua italiana</b>	<b>iii</b>
<b>Contents</b>	<b>v</b>
<b>1 Introduction</b>	<b>1</b>
<b>2 Theory</b>	<b>7</b>
2.1 Harmonic oscillator . . . . .	7
2.2 Molecular vibrational resonances . . . . .	10
2.2.1 Linear polarization . . . . .	11
2.2.2 Non-linear polarization . . . . .	14
2.3 Spontaneous Raman . . . . .	14
2.4 Coherent Raman scattering . . . . .	18
2.4.1 Harmonic oscillator solution . . . . .	18
2.4.2 Induced non-linear polarization . . . . .	19
2.5 SRS process . . . . .	20
2.5.1 Coherence and interferometry . . . . .	20
2.5.2 Single dipole . . . . .	20
2.5.3 Bulk material . . . . .	22
2.6 SRS cross-section . . . . .	24
2.6.1 Spontaneous Raman cross-section . . . . .	24
2.6.2 SRS cross-section introduction . . . . .	25
2.6.3 Stimulated VS spontaneous Raman cross-section . . . . .	26
2.6.4 SRS cross-section measurement . . . . .	28
<b>3 Filling Factor</b>	<b>31</b>
3.1 Lock-in amplifier . . . . .	31

3.1.1	Lock-in working principle . . . . .	31
3.1.2	Lock-in for $\Delta I$ measurement . . . . .	32
3.2	Introducing a corrective factor: the filling factor . . . . .	33
3.3	Experimental set-up for FF measurement . . . . .	36
3.4	Experimental results . . . . .	39
3.5	Data analysis . . . . .	46
<b>4</b>	<b>SRS cross-section</b>	<b>55</b>
4.1	Experimental set-up for $\sigma_{SRS}$ measurement . . . . .	55
4.2	$\Delta I/I$ measurement . . . . .	60
4.3	SRS cross-section . . . . .	63
4.3.1	Spatial distribution . . . . .	64
4.3.2	Temporal distribution . . . . .	68
4.3.3	Spectral distribution . . . . .	73
4.3.4	Results and considerations . . . . .	73
	<b>Conclusions and future perspectives</b>	<b>77</b>
	<b>Bibliography</b>	<b>79</b>
	<b>A Appendix A: FF independence on modulated over total amplitude</b>	<b>81</b>
	<b>List of Figures</b>	<b>83</b>
	<b>List of Tables</b>	<b>87</b>

# 1 | Introduction

This chapter frames the principal arguments and reasons behind the work presented in this thesis. Since always researchers aim to reach the smaller scale possible when we talk about microscopy, keeping at the same time a good spatial resolution. Different techniques aims to achieves this. Conventional bright-field microscopy is a widely used technique in life sciences as it provides information about the specimen's refractive index and absorption properties due to variations in the illuminations field[23] allowing visualisation of morphological details up to the sub-micrometre scale, but no information about chemical composition can be extracted. Fluorescent microscopy on the other hand, is due to visible light emanating from the specimen itself, allowing to reach even the single molecule sensitivity and a high selectivity. The problem is that often the specimen does not posses the necessary fluoescence characteristics. To overcome this, a fluorescent marker(e.g. a fluorophore or dyes) is attached to the desired molecule. This allows to use fluorescence microscopy for a wide variety of sample, but using a label intrinsically modify the sample itself. Raman microscopy is a microscopy technique based on the Raman Scattering(RS) that offers a solution to this problem. Predicted in 1923 by Smekal[21] and observed later by Raman and Krishnan[7, 19], Raman scattering is an inelastic scattering of photons by matter, where photons exchange energy with molecular vibrations,[24] in particular the molecule gain energy when a mechanical vibrational level is excited (Stokes) or lose energy when is de-excited(anti-Stokes). Since every molecule has unique energy levels, the frequency of scattered light from a molecule can describe the structural characteristics of its chemical bonds, Raman spectroscopy enables highly chemical-specific, high-sensitivity, high-accuracy analysis of molecular vibration modes and also is a label-free technique.[14].

This signature spectrum that could be obtained thanks to this technique presents, as we can observe in Fig.1, three principal regions:

- The fingerprint region in the low wavenumber region( $500 - 1800 \text{ cm}^{-1}$ ). This is the spectrum region where are present **identificative** vibrational peaks.
- The silent region( $1800 - 2700 \text{ cm}^{-1}$ ) where are typically present just triple bonds.
- The High Wavenumber(HW) region( $2700 - 3100 \text{ cm}^{-1}$ ), where are present hydrogen

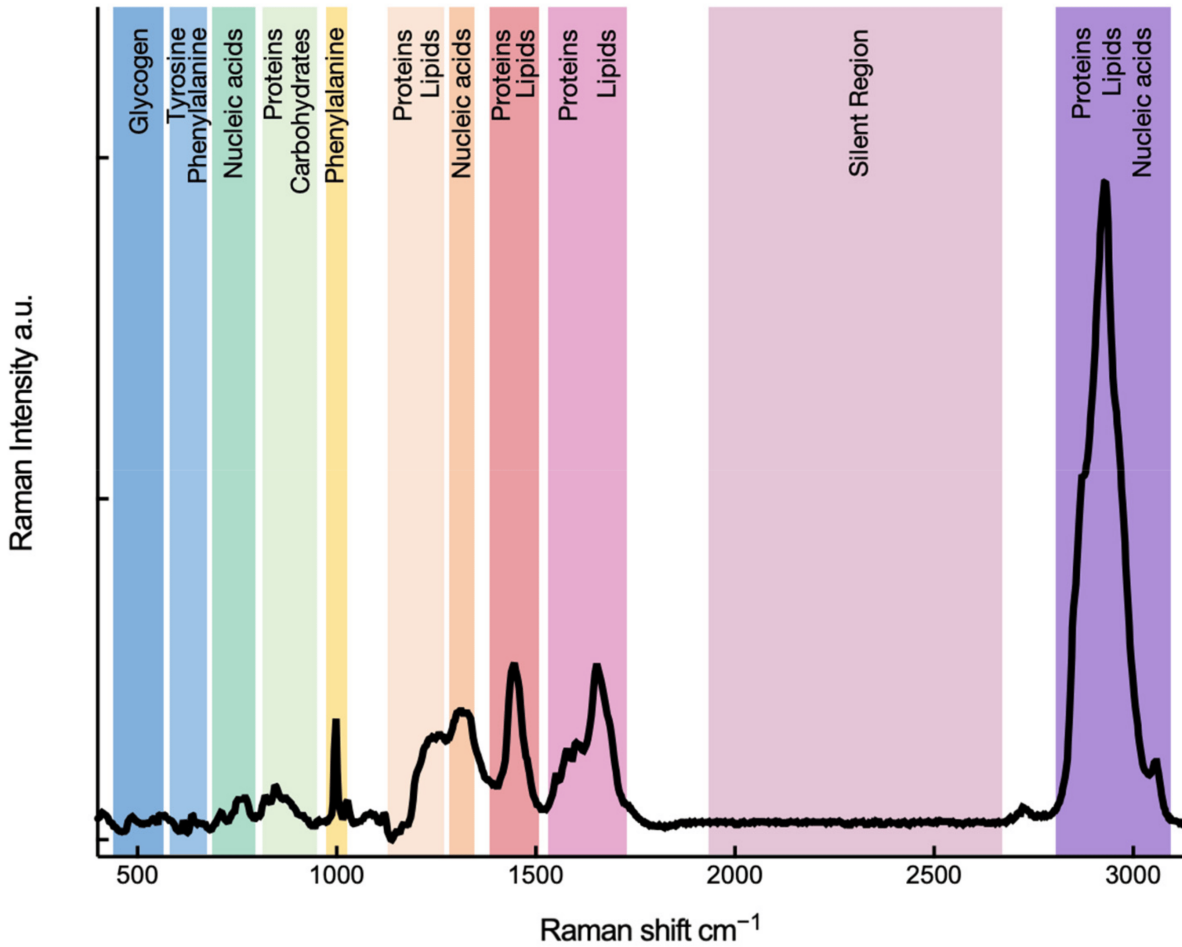


Figure 1.1: Raman spectrum of a single cell of human primary glioblastoma U87 cell line. The different highlighted regions shows the cell components.

bond vibrational levels ( C-H, N-H).

Water peaks are beyond  $3100\text{cm}^{-1}$ . Up to now we had described the spontaneous Raman scattering, where after the incident photon absorption, the anelastic one is emitted spontaneously. Even though this technique owns all the advantages presented before, due to its spontaneous and incoherent nature it is a slow and weak process. To better understand this concept it is convenient to take into account the Raman cross-section  $\sigma_{Raman}$ .  $\sigma_{Raman}$  is a parameter with the units of an area ( $\text{cm}^2$ ) that is implied in literature to characterize the strength of RS. In order to address the word weak to the process is wise to make a fair comparison, in particular we could compare  $\sigma_{Raman}$  with its electrical counterpart: the linear absorption cross-section  $\sigma_{Absorption}$ . Even though there is a conceptual problem since those two process belong to different light-matter interaction order, comparing them is sufficient to give us an overview on the strength of the processes and so on how suitable it is for microscopy purposes.

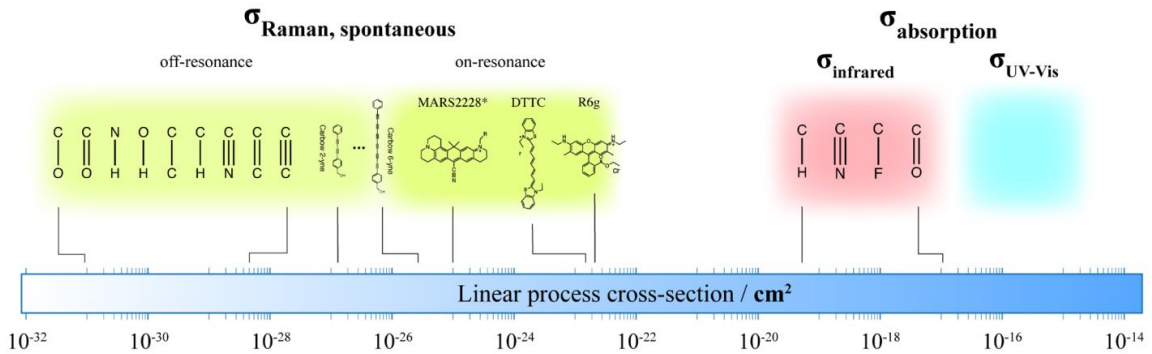


Figure 1.2: Cross-sections of spontaneous Raman scattering (in and off resonance) and linear absorption (IR and UV) for various molecules and bond. The difference in strength between the two process is easily observable. [9]

For the same molecules the  $\sigma_{\text{Raman}}$  can be 8-14 times smaller than the  $\sigma_{\text{Absorption}}$  (Fig.2), validating what we anticipated about his weakness. Even working on resonance, that is when the pump frequency matches the electronic transition of the molecule leading to a significant signal enhancement, it is not sufficient. The solution to these limitations of spontaneous Raman Scattering (RS) lies in Coherent Raman Scattering (CRS). CRS employs a sequence of spatially and temporally synchronized **narrowband** (compromise between time resolution e spectral selectivity) light pulses. Specifically, it employs two light pulses at frequencies  $\omega_p$  (pump) and  $\omega_s$  (Stokes), such that  $\Omega = \omega_p - \omega_s$  where  $\Omega$  is the vibrational frequency of interest. In the focal volume the interaction between the laser pulses and the molecules allows the latters to oscillate, and so emit, coherently. This leads to an enhancing of the resulting signal compared to the incoherent Spontaneous Raman counterpart. In the past two decades the popularity of CRS improves thanks principally to this enhancing in the Raman signal with respect to the spontaneous one. CRS naturally present also the intrinsic advantages of the Raman microscopy, so in general the advantages of CRS are [22]:

- It does not require fluorescent probes, it's a label-free technique .
- It is significantly more sensitive than spontaneous Raman microscopy, this leads to
  - Needs of only moderate average power for excitation, which is tolerable for most biological samples.
  - Higher imaging speeds.
- As a nonlinear microscopy technique with signal generation confined to the focal volume, it offers three-dimensional sectioning capability, similar to multi-photon-

induced fluorescence microscopy.

- The use of visible or near-infrared excitation reduces sample heating due to minimal water absorption and enables deep imaging penetration through thick tissues or cells.

CRS technique can be divided in two main techniques, the stimulated Raman scattering (SRS) and the coherent anti-Stokes Raman scattering (CARS). They both explore the vibrational energy level of the specimen, but they differ in the process explored and the acquired signal. In the SRS processes, the interactions with the pump and Stokes fields leads to a stimulated emission at the frequency of the Stokes beam, resulting in a Stokes-field amplification (stimulated Raman gain, SRG) and in a pump-field attenuation (stimulated Raman loss, SRL). While, in the CARS process, the vibrational information is retrieved by making the sample interact with a third beam, called probe beam, generating a coherent radiation at the anti-Stokes frequency ( $\omega_{as} = \omega_{pr} + \Omega$ ). Typically, this third beam is the pump itself, thus having  $\omega_{as} = \omega_{pu} + \Omega$ .

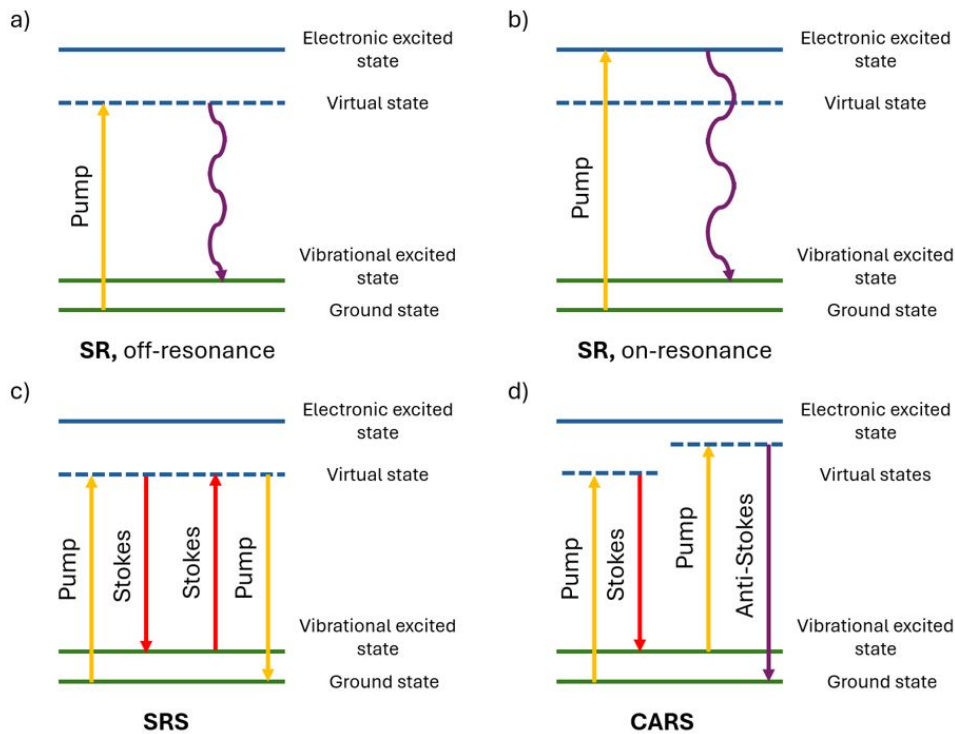


Figure 1.3: Different Raman processes in Jablonski representation. a) Spontaneous Raman off-resonance b) Spontaneous Raman on-resonance c) Stimulated Raman Scattering d) Coherent Anti-Stokes Raman Scattering

The following work is focused on SRS technique, as mentioned previously SRS signal is an increase (SRG) or a decrease (SRL) in the interested field, anyway the intensity changes,

$\Delta I$ , are small compared to the absolute intensity of the laser beam,  $I$  ( $\Delta I/I < 10^{-3}$ )[4], they are buried in the laser noise, which is typically a few percent. To retrieve this small signal, a lock-in amplifier is typically used. This will be discussed in detail in Chapter 3. The SRS signals or spectra in literature[4], are up to now represented as an intensity ratio  $\Delta I/I$ , a dimensionless quantity, or expressed in arbitrary units. The main reason in doing so are:

- It simplifies the comparison across various experimental setups or conditions, such as differing laser intensities or the use of different samples, without the need to concern oneself with specific units of intensity.
- SRS theory would be explored in detail in Chapter 2. In SRS the expression for  $\Delta I$  is presented only as a simple proportionality. This limitation makes impossible compare an absolute value of  $\Delta I$  across different set-ups.
- The shape of the spectrum, including the positions of the peaks and the relative intensities among them, is well preserved and accurately represented.

A fundamental principle of science is the reproducibility of experiments, which allows results to be verified in different contexts and times. To achieve reproducibility, two key elements are essential: first, the use of standardized units of measurement to provide a clear, quantitative representation of the variables being studied; and secondly use standard operating procedures (SOPs) throughout the experiment, including detailed documentation of the entire experimental setup. SRS signal representations up to now bypass those procedures. The main aim of this work is to perform a step towards the acquisition of **quantitative SRS signals**. More precisely we will focus on the work of very recent papers where there is an introduction of a new cross-section to represent the strength of the SRS process, the  $\sigma_{SRS}$ . [9] This would bring to an expression for a quantitative SRG/SRL signal. The introduction of this cross-section, since SRS requires two input fields, takes inspiration from an analogy with the famous two-photon absorption (TPA) process, which was first predicted by Maria GöppertMayer in 1931 [10] . Interestingly, the Raman effect was utilized as a motivation for two-photon absorption in the original prediction. We will try to measure the  $\sigma_{SRS}$  with a slightly different procedure than the authors and compare the results. To extract the  $\sigma_{SRS}$  is necessary the standard  $\Delta I/I$  that, as said before, must be acquired with a lock-in amplifier. Without entering in this chapter into details, due to the pulsed nature of the used fields, the measure requires a corrective factor, that we will call **Filling Factor** (FF). This is a factor used for the calibration of the  $\Delta I/I$  value, so crucial to consider it for quantitative SRS measurements. FF will be explored in details in Chapter 3.



## 2 | Theory

In this second chapter, the foundational theory required for understanding the SRS cross-section will be discussed. The following sections begins by presenting the mathematical framework, starting with the harmonic oscillator and progressing to the standard SRS imaging.

### 2.1. Harmonic oscillator

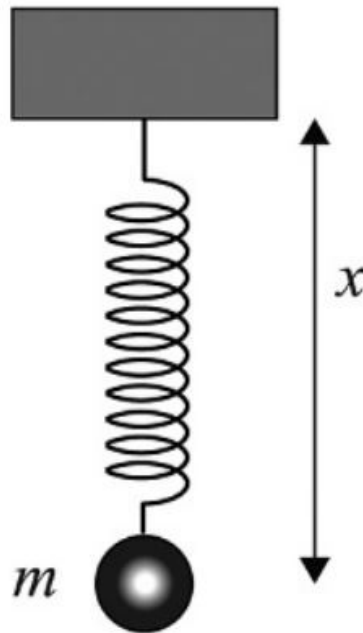


Figure 2.1: A body with mass  $m$  attached to a spring with stiffness  $k$  in presence of the gravitational acceleration  $g$ .

The harmonic oscillator is an idealized physical system characterized by temporal oscillations that follow a sinusoidal wave with a constant amplitude, where the oscillation frequency depends exclusively on the parameters of the system. This model appears widely across various fields of physics and serves as a reliable approximation for physical

systems near a stable equilibrium. In the context of mechanics, the simplest form of a harmonic oscillator consists of a mass  $m$  attached to a spring with stiffness  $k$ . When oriented vertically, as shown in Fig. 2.1 the mass experiences gravitational force  $g$ , and its center of mass can be described by

$$mg - kx_0 = 0 \quad (2.1)$$

Starting from fundamental principles of dynamics one could study the mass displacement  $x$  from its equilibrium position  $x_0$ . In particular is sufficient to start from the Newton law taking already into account (2.1), writing

$$ma = -kx \quad (2.2)$$

The acceleration  $a$  is the second derivative of the displacement  $x$  obtaining

$$\frac{d^2x}{dt^2} + \omega_0^2x = 0 \quad (2.3)$$

where  $\omega_0 = k/m$  is the system resonant frequency

Considering a real case, mass experiences force due to friction:  $F_{fric} = -2\gamma m(dx/dt)$ , where  $\gamma$  is the damping. This force is proportional to the mass speed so it will be zero just in the equilibrium position. The equation describing the mass movement is now

$$\frac{d^2x}{dt^2} + 2\gamma\frac{dx}{dt} + \omega_0^2x = 0 \quad (2.4)$$

We add now to the system a driven force  $F(t)$ . We consider the case where this force is periodic such that  $F(t) = F_0\cos(\omega t)$ , where  $F_0$  is the force amplitude and  $\omega$  its angular frequency. The mass movement equation becomes

$$\frac{d^2x}{dt^2} + 2\gamma\frac{dx}{dt} + \omega_0^2x = \frac{F(t)}{m} \quad (2.5)$$

For more simplicity is useful to express  $F(t)$  using the complex notation:  $F(t) = F_0e^{-i\omega t}$ . Since we are in presence of a periodic excitation, we now look for a displacement solution in the same form  $x(t) = x(\omega)e^{-i\omega t}$ . Inserting this generic solution in (2.5), it comes

$$(-\omega^2 - i2\gamma\omega + \omega_0^2)x(\omega)e^{-i\omega t} = \frac{F_0e^{-i\omega t}}{m} \quad (2.6)$$

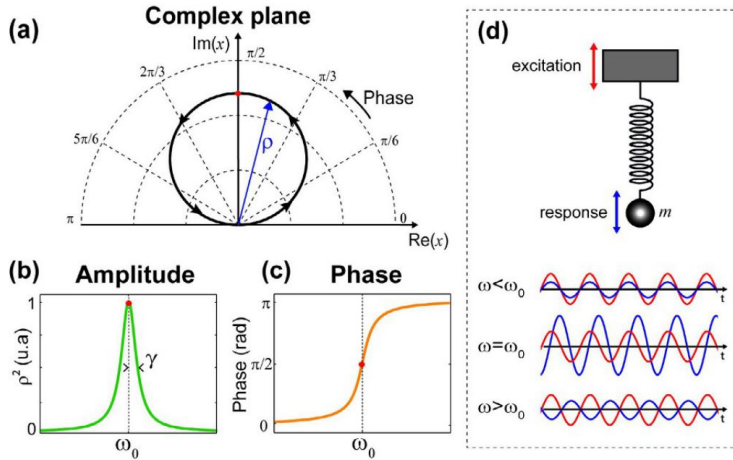


Figure 2.2: Damped forced harmonic oscillator close to resonance. a) Representation in the complex plane of  $x$  b) Amplitude of  $x$  ( $\rho$ ) in function of  $\omega$  c) Phase of  $x$  ( $\phi$ ) in function of  $\omega$  d) Time domain description of the three regimes: below, at, and above resonance [5]

where  $x(\omega)$  can be expressed as

$$x(\omega) = \frac{F_0/m}{\omega_0^2 - \omega^2 - i2\gamma\omega} \quad (2.7)$$

Close to the resonance ( $\omega \approx \omega_0$ ), and for small damping coefficient ( $\gamma \ll \omega_0$ ), the harmonic oscillator solution (2.7) can be approximated by a complex Lorentzian function

$$x(\omega) = \frac{-F_0/(2m\omega_0)}{(\omega - \omega_0) + i\gamma} \quad (2.8)$$

The complex plane  $[\text{Re}(x), \text{Im}(x)]$  shown in Fig. 2.2a, is a nice way to display this Lorentzian function as the displacement  $x(\omega)$  describes a circle when the angular frequency  $\omega$  varies [8]. Denoting  $\rho$  and  $\phi$  the amplitude and phase of the displacement, we can write  $x(\omega) = \rho(\omega)e^{i\phi(\omega)}$ . Depending on the value of  $\omega$ , there are three particular behavior around the resonance:(Fig. 2.2d):

1.  $\omega \ll \omega_0$ . The displacement amplitude is weak and its phase is close to zero. The oscillation is in phase with the excitation drive.
2.  $\omega = \omega_0$ . The displacement amplitude is strong and its phase is  $\pi/2$ . The oscillation is shifted around 90 degrees with respect to the excitation drive (phase quadrature).
3.  $\omega \gg \omega_0$ . The displacement amplitude is weak and its phase is close to  $\pi$ . The oscillation is lagging by 180 degrees with respect to the excitation drive (phase opposition).

Using a simple oscillator model, we have described the phenomenon of resonance. We will now move to vibrational molecular resonances where the driving force is provided by an

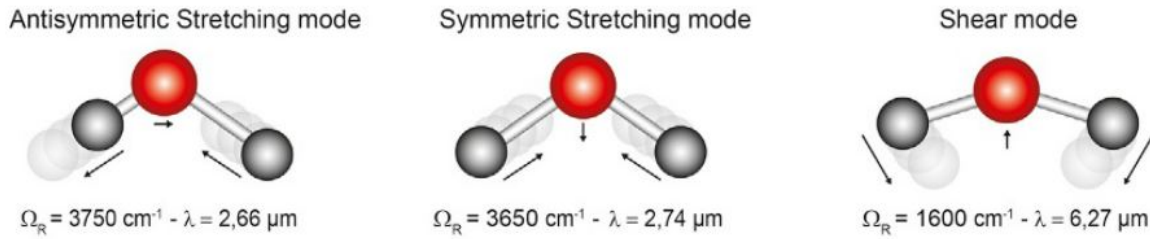


Figure 2.3: Representation of three vibrational modes of  $H_2O$  with their respective wavenumber and wavelength.[5]

electromagnetic wave.

## 2.2. Molecular vibrational resonances

A molecular structure sustains many vibrational and rotational intramolecular vibrations that can be described in terms of normal modes. Each of these “roto-vibrational” normal modes is independent of the other normal modes; it has a center of mass that is preserved and specific energy that is quantized as described by the quantum mechanical theory. The atomic mass, the number of involved chemical bonds, the atomic species, the molecule geometry and symmetry and the possible hydrogen bonds interactions affect the stiffness of the vibrational forces at work that, in the end, dictate the possible vibrational energies. All these vibrational energies belong to the infrared domain and can be probed by absorption spectroscopy. Rotational modes are only observable when molecules are in the gas phase and correspond to energies ranging from 10 to  $400\text{ cm}^{-1}$ , which correspond to the far-infrared electromagnetic domain (wavelengths between 25 and 10,000mm). Rotovibrational modes correspond to energies ranging from 1 to  $4000\text{ cm}^{-1}$  corresponding to the mid-infrared domain (wavelengths between 2.5 and 25mm). Near-infrared radiations ranging from  $4000$  to  $14,000\text{ cm}^{-1}$  (wavelengths from 0.7 to 2.5mm) can also excite overtones of these vibrations. A molecule having a geometry that is not linear and constituted of  $n$  atoms will have  $3n - 6$  normal vibration modes. For instance, water molecules ( $H_2O$ ) have three modes of vibrations that are shown in Fig.2.3, other molecules may exhibit other modes of vibration such as scissoring modes, twisting modes, rocking modes, torsion modes, and wagging modes [25]. A molecule having a linear geometry will have only  $3n - 5$  normal vibration modes because any rotation along its molecular axis keeps the molecule unchanged. Therefore, diatomic molecules ( $n = 2$ ) will have only one normal vibration mode.

As mentioned previously we are interested in considering the vibrational resonance under

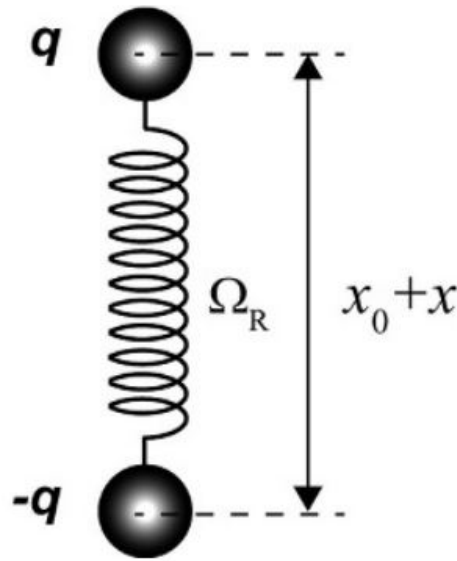


Figure 2.4:  
Schematization of  
a simple diatomic  
molecule.

electromagnetic forces. The reason behind this interest is that both linear and nonlinear optical effects can be understood as resulting from the interaction between the electric field component of electromagnetic radiation and the charged particles within a material or molecule. Typically, an applied electric field moves positively charged particles in the direction of the field and negatively charged particles in the opposite direction. The electric field associated with the visible and near-infrared regions of the electromagnetic spectrum oscillates at frequencies around the  $10^3$  THz range. These frequencies are too high for the nuclei to follow adiabatically. However, the electrons in the material or molecule are light enough to track the rapid oscillations of the driving field. As a result, optical resonances in this frequency range are primarily caused by the motions of electrons within the material.

### 2.2.1. Linear polarization

For clarification purpose, we will consider the case where the molecule is a single and isolated diatomic molecule. We suppose that this molecule is made with two nuclei, separated by  $x_0$ , that are considered as two points with masses  $m_1$  and  $m_2$ . We consider now that the elongation vibrational mode can be described by a simple harmonic oscillator with a resonant frequency  $\Omega_R$ . Within this simple picture, the cores are connected with a spring. We are now considering in particular, a **polar** diatomic molecule, as displayed in Fig. 2.4, where an asymmetric distribution of positive and negative charges induces a dipole moment  $\vec{\mu}$ . We suppose that the first atom holds the charge  $q$  whereas the second atom has the charge  $-q$ . The dipole moment of these two punctual charge systems can

then be expressed in vector form:

$$\vec{\mu} = q\vec{x} \quad (2.9)$$

where  $\vec{x}$  is the displacement vector oriented from the negative to the positive charge.

We consider now the molecule embedded in an electromagnetic field  $\vec{E}(t)$  with angular frequency  $\omega$  that is linearly polarized along the molecule axis. This electric field generates a force on the molecule  $F_{lorenz}(t) = qE_0e^{-i\omega t}$  and the elongation response of the molecule  $x$  follows a driven harmonic oscillation as in (2.5)

$$\frac{d^2x}{dt^2} + 2\gamma\frac{dx}{dt} + \Omega_R^2x = \frac{F_{lorenz}(t)}{\beta} \quad (2.10)$$

with  $\beta$  the reduced mass:  $\beta = m_1m_2/(m_1 + m_2)$ . The damping term  $\gamma$  now expresses the radiation loss of this oscillating dipole.

If instead of a single isolated molecule we consider a volume with  $N$  electric dipoles per unit of volume, the macroscopic polarization is (in a general form):

$$\vec{P} = N\vec{\mu} = Nq\vec{x} \quad (2.11)$$

When the applied electric fields are weak in comparison to the field that binds the electrons to the nuclei, the displacement is directly proportional to the applied electric field. This allows us to write the **linear** polarization in a general form as:

$$\vec{P}_L(t) = \epsilon_0\chi^{(1)}\vec{E}(t) \quad (2.12)$$

where:

$\epsilon_0$  is the electric permittivity in vacuum

$\chi^{(1)}$  is the **linear** material susceptibility

Under those condition (electric field polarized along the molecule in a linear regime) equation (2.12) can be reframed as:

$$P_L(\omega) = \epsilon_0\chi^{(1)}E(\omega) \quad (2.13)$$

This expression highlights that, in the weak field limit, the induced polarization in the material depends linearly on the magnitude of the applied field. Such linear dependence is the origin of all linear optical phenomena. In this context we can retrieve the vibrational

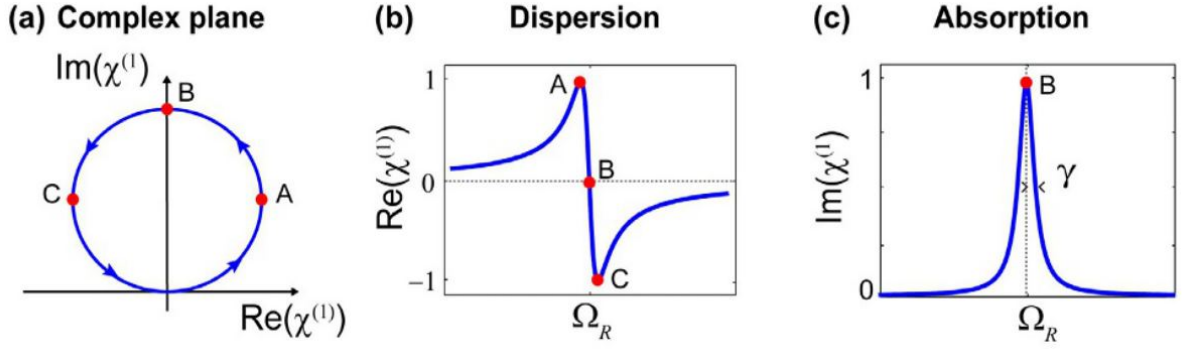


Figure 2.5: Angular frequency dependence of  $\chi^{(1)}$ . a) Representation in the complex plane b) The real part of  $\chi^{(1)}$  linked to the material dispersion c) The imaginary part of  $\chi^{(1)}$  linked to the material absorption[5]

contribution to susceptibility  $\chi^{(1)}$ . This is done by comparing equation (2.13) with equation (2.11), and introducing the solution  $x(\omega)$  of equation (2.10), obtaining:

$$\chi^{(1)}(\omega) = \frac{-\frac{Nq^2}{2\epsilon_0 m \Omega_R}}{(\omega - \Omega_R) + i\gamma} \quad (2.14)$$

For diluted media, the real part of  $\chi^{(1)}$  is related to the refractive index dispersion (Fig. 2.5b)

$$n_{mat}(\omega) = n_{mat0} - \frac{Re[\chi^{(1)}(\omega)]}{2n_{mat0}} \quad (2.15)$$

where  $n_{mat0}$  is the mean refractive index of the material. Whereas the imaginary part of  $\chi^{(1)}$  is related to the absorption coefficient of the medium (Fig. 2.5c):

$$\alpha(\omega) = \frac{2\pi}{\lambda_0 n_0} Im[\chi^{(1)}(\omega)] \quad (2.16)$$

where  $\alpha$  is often expressed in  $cm^{-1}$ , and is the key parameter involved in the Beer-Lambert law that describes the intensity ( $I$ ) loss of a light beam that propagates in a medium over the distance  $L$

$$I(L) = I(0)e^{-\alpha L} \quad (2.17)$$

### 2.2.2. Non-linear polarization

When instead it comes to deal with stronger field, the electron is farther displaced from its equilibrium position. For larger displacements, the binding potential can no longer be assumed to be harmonic as anharmonic effects become more significant. When the anharmonic shape of the potential becomes important, the dependence between the driving electric field and the induced polarization is not strictly linear, and corrections to the polarization will have to be made. Fig. 2.6 illustrates the nonlinearity between the driving field and the induced polarization in the presence of anharmonicity. If the anharmonic contributions to the harmonic potential are relatively small, the displacement  $x$  can be expressed as a power series in the field. This implies that the displacement of the electron is no longer linearly dependent on the field as nonlinear corrections grow in importance. In a similar fashion, the polarization can be written as a power series in the field to include the nonlinear electron motions:

$$\begin{aligned} P(t) &= \epsilon_0[\chi^{(1)}E(t) + \chi^{(2)}E(t)^2 + \chi^{(3)}E(t)^3 + \dots] \\ &= P^{(1)}(t) + P^{(2)}(t) + P^{(3)}(t) + \dots = P_L + P_{NL} \end{aligned} \quad (2.18)$$

where

$\chi^{(n)}$  is the n-th order susceptibility

$P^{(n)}$  is the n-th order polarization

The coherent Raman effects described in this work can all be understood as resulting from the third-order contribution to the polarization  $P^{(3)}$ . The magnitude of these effects is thus governed by the strength of the triple product of the incoming fields and the amplitude of the third-order susceptibility  $\chi^{(3)}$ . More details will be provided on the upcoming sections.

## 2.3. Spontaneous Raman

When a molecule scatters light, most of the scattered photons keep their original frequencies, which is a phenomenon known as elastic scattering or “Rayleigh scattering”. However, a small fraction of the incident light is scattered in an inelastic way, i.e., scattered with a frequency that is different from the original incoming light, a phenomenon known as the “Raman effect.”

To understand the Raman effect, let us consider again the diatomic molecule described earlier. The molecule is not necessarily polar but its polarizability (mostly from electronic

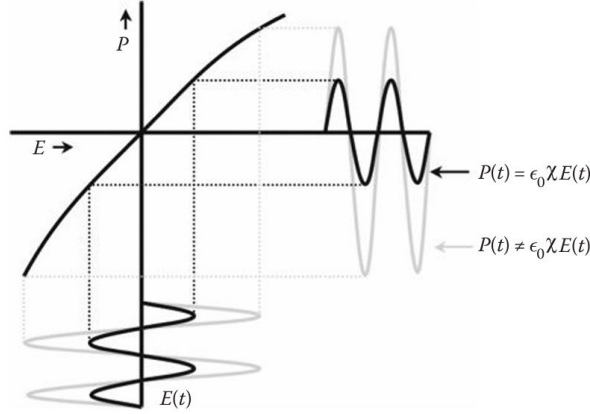


**Figure 2.6:** Relationship between the incident electric field and induced polarization. With weak electric fields (illustrated by the black sinusoidal line), only the harmonic part of the potential is significant, resulting in polarization that is directly proportional to the field. As the field strength increases (shown by the gray sinusoidal line), the anharmonic components of the potential begin to play a role, causing the polarization to respond nonlinearly to the applied field. In this regime, the polarization profile no longer follows the sinusoidal shape of the incoming field. [4]

origin) depends on the intramolecular distance  $x$ . This distance fluctuates at the resonant molecular bond frequency  $x(t) = x_f \cos(\Omega_R t)$ , where  $x_f$  is the amplitude fluctuation. For tiny displacements, it is possible to perform a Taylor expansion of the polarizability  $\alpha(t)$  near its initial value  $\alpha_0$

$$\alpha(t) = \alpha_0 + \left( \frac{\partial \alpha}{\partial x} \right)_0 x(t) + \dots \quad (2.19)$$

The exciting field  $E(t) = E_0 \cos(\omega_p t)$  induces a dipole moment into the molecule

$$\vec{\mu}(t) = \epsilon_0 \alpha(t) \vec{E}(t) \quad (2.20)$$

Approximating the polarizability up to the first order and inserting it in equation (2.20), and considering again the electric field aligned with the molecule, we obtain

$$\begin{aligned} \mu(t) &= \epsilon_0 \left[ \alpha_0 + \left( \frac{\partial \alpha}{\partial x} \right)_0 x_f \cos(\Omega_R t) \right] E_0 \cos(\omega_p t) \\ &= \epsilon_0 \alpha_0 E_0 \cos(\omega_p t) + \frac{\epsilon_0 \left( \frac{\partial \alpha}{\partial x} \right)_0 E_0 x_f}{2} \cos[(\omega_p - \Omega_R)t] \\ &\quad + \frac{\epsilon_0 \left( \frac{\partial \alpha}{\partial x} \right)_0 E_0 x_f}{2} \cos[(\omega_p + \Omega_R)t] \quad (2.21) \end{aligned}$$

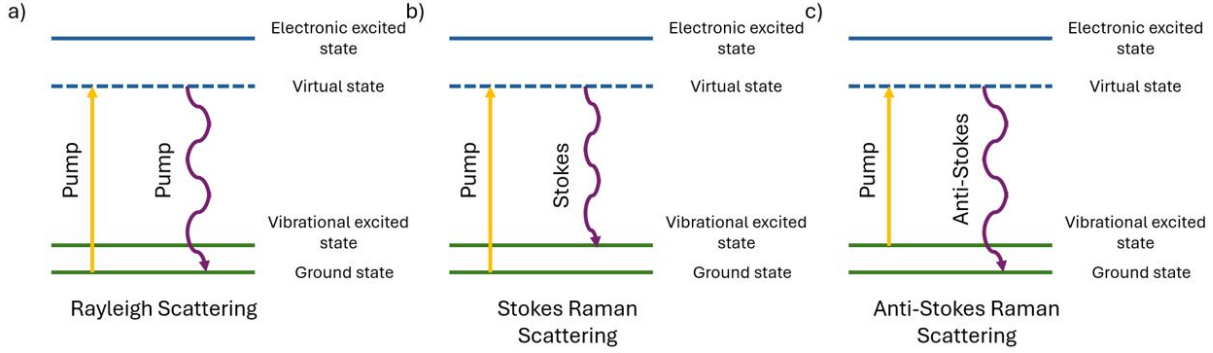


Figure 2.7: Jablonski representation of a) Rayleigh Scattering b) Stokes Raman Scattering c) Anti-Stokes Raman Scattering

The first term with frequency  $\omega_p$  describes the Rayleigh scattering (Fig. 2.7a). The second term with frequency  $\omega_s = \omega_p - \Omega_R$  describes a red-shifted scattering known as the Raman Stokes scattering (Fig. 2.7b). In this case, the molecule moves from its ground state to an excited vibrational state (phonon creation) whereas the incoming field loses energy. The third term with frequency  $\omega_{as} = \omega_p + \Omega_R$  describes a blue-shifted scattering known as the anti-Stokes Raman scattering (Fig. 2.7c) where the molecule goes from the excited vibrational level toward its ground state giving energy to the incoming photon (and absorbing a phonon). Experimentally, the anti-Stokes scattered intensity is lower than the Stokes scattered intensity. This is because at thermal equilibrium atomic level populations are described by the Boltzmann distribution so that the population in the excited vibrational level is lower than the ground state one. Stokes and anti-Stokes scattered intensities become equally intense only for infinite temperature where all the states are equally populated. The amplitude of the Stokes and anti-Stokes components are then proportional to the magnitude of the electric field radiated by the dipole at the shifted frequencies. The amplitude of the electric field at frequency  $\omega_s$ , radiated by the oscillating dipole along the vector position  $\vec{r}$  in the far field, is obtained from electrodynamics in scalar form as

$$E(\omega_s) = \frac{\omega_s^2}{4\pi\epsilon_0 c^2} |\mu(\omega_s)| \frac{e^{ikr}}{r} \sin(\theta) \quad (2.22)$$

where  $k$  is the wave vector of the radiated field,  $c$  is the speed of light,  $\theta$  is the angle relative to the dipole axis,  $r$  is the distance from the dipole location to the observation point and  $|\mu(\omega_s)|$  is the amplitude of the dipole at  $\omega_s$ . The expression for the anti-Stokes field is the same. Inserting  $|\mu(\omega_s)|$  from (2.21) in (2.22), the spontaneous Raman intensity

obtained from the field is

$$I(\omega_s) = \frac{\omega_s^4}{12\pi\epsilon_0 c^3} x_0^2 |E_0|^2 \left| \frac{\partial\alpha}{\partial x} \right|^2 \quad (2.23)$$

From equation (2.23) we see that the classical model predicts a  $\omega^4$  dependence of the intensity of the Raman scattered light. In addition, it scales with  $\left| \frac{\partial\alpha}{\partial x} \right|^2$  and with the intensity of the incident beam  $I_0 = |E_0|^2$ . The phase  $\phi$  of the Raman scattered light is dependent on the nuclear mode oscillation. At equilibrium, the nuclear vibrations of different molecules are uncorrelated, i.e., each molecule carries its own independent phase  $\phi_i$ . This implies that the phase of the radiated field from one dipole emitter is unrelated to the phase of the radiated field by a second dipole emitter elsewhere in the sample. Consequently, the signal is incoherent and the intensity of the total Raman emission is proportional to equation (2.23) multiplied by the total number of Raman scatterers in the sample. It is interesting to note that the first term in Equation (2.21), which represents elastic light scattering, is not dependent on the nuclear vibration, and thus does not acquire a random phase  $\phi$ . This is the reason why Rayleigh scattering is coherent while the Raman-shifted contributions are incoherent.

Experimentally it is useful to define the Raman signal strength in terms of a cross-section  $\sigma_{Raman}$ . The cross-section expresses the Raman scattering efficiency of a molecule in a manner analogous to the previously seen absorption cross-section in the Beer's law (2.17). Using the cross-section  $\alpha_{Raman}$ , the total scattered Raman-shifted light from a sample with length  $z$  and a molecular number density  $N$  is written as

$$I(\omega_s) = Nz\sigma_{Raman}(\omega_s)I_0 \left( \frac{\omega_s}{\omega_p} \right) \quad (2.24)$$

That can be equivalently written as

$$rate_{Raman}(\omega_s) = n\sigma_{Raman}(\omega_s)\Phi_p \quad (2.25)$$

where  $\Phi$  represent a photon flux, so the number of photons per unit of second and area  $photons/s \cdot cm^2$ ,  $n$  is the number of oscillator in the volume (adimensional), and  $rate_{Raman}$  is the number of Raman photons produced per unit of second at frequency  $\omega_s$ .

## 2.4. Coherent Raman scattering

Coherent Raman scattering (CRS) is a resonant and coherent process that allows gaining a factor of  $10^7$  in efficiency as compared to spontaneous Raman scattering [20].

### 2.4.1. Harmonic oscillator solution

Let us consider two incoming plane waves, that we denote pump and Stokes, with frequencies  $\omega_p$  and  $\omega_s$ , respectively. These waves interact with a medium having roto-vibrational vibrations  $\Omega_R$ . The total field can be written as

$$E(z, t) = A_p e^{i(k_p z - \omega_p t)} + A_s e^{i(k_s z - \omega_s t)} + c.c. \quad (2.26)$$

where "c.c." is the complex conjugate and  $z$  is the axial position.

The interference between these two fields generates a beating with the frequency  $\Omega = \omega_p - \omega_s$  as seen in the intensity term

$$\langle E^2(z, t) \rangle = A_p A_s^* e^{i(Kz - \Omega t)} + c.c. \quad (2.27)$$

where  $\langle \rangle$  is the time average over one optical period and  $K = k_p - k_s$ . If the frequency difference  $\Omega$  is set equal to  $\Omega_R$ , the roto-vibrational mode enters in resonance with the wave beating.

Let us consider again our driven harmonic oscillator describing a diatomic molecule

$$\frac{d^2 x}{dt^2} + 2\gamma \frac{dx}{dt} + \Omega_R^2 x = \frac{F(t)}{\beta} \quad (2.28)$$

The energy  $W$  necessary to create a dipolar moment  $\vec{\mu}(t) = \epsilon_0 \alpha(t) \vec{E}(t)$  is given by

$$W = \frac{1}{2} \langle \vec{\mu}(z, t) \cdot \vec{E}(z, t) \rangle = \frac{1}{2} \epsilon_0 \alpha(t) \langle E^2(z, t) \rangle \quad (2.29)$$

Similar to spontaneous Raman scattering, we assume that the polarizability is related to the intramolecular distance following equation (2.19). Inserting equation (2.27) in equation (2.29) gives the excitation force produced by the two incoming fields on the molecule:

$$F(t) = \frac{dW}{dx} = \epsilon_0 \left( \frac{\partial \alpha}{\partial x} \right)_0 [A_p A_s^* e^{i(Kz - \Omega t)} + c.c.] \quad (2.30)$$

Using this  $F(t)$  in equation (2.28) and looking for an oscillating solution, near the resonance the molecular vibration amplitude is given by

$$x(\Omega) = \frac{-\left(\frac{\epsilon_0}{2m\Omega_R}\right)\left(\frac{\partial\alpha}{\partial x}\right)_0 A_p A_s^*}{(\Omega - \Omega_R) + i\gamma} \quad (2.31)$$

If the beating frequency is such that  $\Omega = \Omega_r$ , the molecular vibration amplitude becomes large and the excitation fields will now also induce nonlinear polarization that will be specific to the molecular resonance.

### 2.4.2. Induced non-linear polarization

Inserting the solution of equation (2.31) in equation (2.11), and finally comparing with (2.18), the expression for the induced non-linear polarization  $P_{NL}$  is

$$P_{NL}(z, t) = N\epsilon_0 \left(\frac{\partial\alpha}{\partial x}\right)_0 [x(\Omega)e^{i(Kz-\Omega t)} + c.c.] \times [A_p e^{i(k_p z - \omega_p t)} + A_s e^{i(k_s z - \omega_s t)} + c.c.] \quad (2.32)$$

Expanding this equation, it comes out four different terms at four different frequencies composing the non linear polarization. Those frequencies are  $\omega_{as} = 2\omega_p - \omega_s$ ,  $\omega_{cs} = 2\omega_s - \omega_p$ ,  $\omega_p$  and  $\omega_s$ .

The polarization can thus be expressed as

$$P_{NL}(z, t) = P(\omega_{as})e^{-i\omega_{as}t} + P(\omega_{cs})e^{-i\omega_{cs}t} + P(\omega_p)e^{-i\omega_p t} + P(\omega_s)e^{-i\omega_s t} + c.c. \quad (2.33)$$

where the complex amplitudes  $P(\omega_i)$  are

$$P(\omega_{as}) = N\epsilon_0 \left(\frac{\partial\alpha}{\partial x}\right)_0 x(\Omega)A_p e^{i(2k_p - k_s)z} \quad (2.34)$$

$$P(\omega_{cs}) = N\epsilon_0 \left(\frac{\partial\alpha}{\partial x}\right)_0 x^*(\Omega)A_s e^{i(2k_s - k_p)z} \quad (2.35)$$

$$P(\omega_p) = N\epsilon_0 \left(\frac{\partial\alpha}{\partial x}\right)_0 x(\Omega)A_p e^{ik_p z} \quad (2.36)$$

$$P(\omega_s) = N\epsilon_0 \left(\frac{\partial\alpha}{\partial x}\right)_0 x^*(\Omega)A_s e^{ik_s z} \quad (2.37)$$

Those terms represent respectively the coherent anti-Stokes Raman scattering(CARS), the coherent Stokes Raman scattering (CSRS), the stimulated Raman loss(SRL) and the

stimulated Raman gain (SRG). The last two of them are grouped under a single expression, the stimulated Raman scattering (SRS), and from now on we will focus on just this one.

## 2.5. SRS process

In this section, we will describe in detail the SRG and SRL process, so more in general the SRS process.

### 2.5.1. Coherence and interferometry

Equations (2.36) and (2.37) can be reframed as

$$P(\omega_p) = 6\epsilon_0\chi_R^{(3)}(\omega_p) |A_s|^2 A_p e^{ik_p z} \quad (2.38)$$

$$P(\omega_s) = 6\epsilon_0\chi_R^{(3)}(\omega_s) |A_p|^2 A_s e^{ik_s z} \quad (2.39)$$

Where  $\chi^{(3)}$  is the third-order nonlinear susceptibility, a third-rank tensor that describes the possible interaction between the pump and Stokes exciting fields with the medium. In this simplified case, where we suppose that the pump and Stokes beams propagate along the  $z$  direction and with the same and linear polarization state, the third-order susceptibility is reduced to a scalar. Those two polarization behave as sources for weak non-linear fields,  $E_i^{(3)} = A_i^{(3)} e^{i(k_i z - \omega_i t)}$ , at the correspondent frequencies. Having the same frequencies, and being coherent, those weak non linear fields interfere with the input fields. As a result, the SRS signal can be viewed as the interference between a weak nonlinear field and the strong incoming field.

### 2.5.2. Single dipole

To better understand this phenomenon, let consider a simple situation where the nonlinear medium is a single dipole located in  $z = 0$ . The resulting intensity of this interference can be written as

$$I_p^{SRL} \propto |A_p + A_p^{(3)}|^2 \propto |A_p|^2 + |A_p^{(3)}|^2 + 2 |A_p A_p^{(3)}| \cos [\phi(A_p^{(3)}) - \phi(A_p)] \quad (2.40)$$

$$I_s^{SRG} \propto |A_s + A_s^{(3)}|^2 \propto |A_s|^2 + |A_s^{(3)}|^2 + 2 |A_s A_s^{(3)}| \cos [\phi(A_s^{(3)}) - \phi(A_s)] \quad (2.41)$$

The second term  $|A^{(3)}|^2$  is negligible with respect to  $|A|^2$ . The quantity  $|AA^{(3)}|$  instead can be significant and depends on the phase difference between the generated weak field

and the incoming strong field. Let us have a closer look to this phase difference term. From the induced polarization (2.38) and (2.39), we obtain

$$\begin{cases} \phi(A_p^{(3)}) - \phi(A_p) = \frac{\pi}{2} + \phi(\chi_r^{(3)}(\omega_p)) \\ \phi(A_s^{(3)}) - \phi(A_s) = \frac{\pi}{2} + \phi(\chi_r^{(3)}(\omega_s)) \end{cases} \quad (2.42)$$

Comparing (2.36) and (2.37) with (2.38) and (2.39), and inserting the expression of  $x(\Omega)$  computed in (2.31), we obtain the non linear susceptibilities involved in SRL and SRG processes

$$\begin{cases} \chi_R(\omega_p) = \frac{a/2}{(\Omega - \Omega_R) + i\gamma} \\ \chi_R(\omega_s) = \frac{a/2}{(\Omega - \Omega_R) - i\gamma} \end{cases} \quad (2.43)$$

where  $a$  is a negative constant that describes the oscillator strength of the molecular vibration  $a = -(2N\epsilon_0/6\beta\Omega_R)(\partial\alpha/\partial x)_0^2$ . We can note that the SRL and SRG processes are symmetrical  $\chi_R(\omega_s) = \chi_R(\omega_p)^*$ . At resonance the phases are  $\phi(\chi_R^{(3)}(\omega_p)) = \pi/2$  and  $\phi(\chi_R^{(3)}(\omega_s)) = -\pi/2$ .

Inserting equations (2.42) into (2.40) and (2.41), we obtain the SRS intensities at resonance in the case of a single dipole

$$\begin{cases} I_p^{SRL} \propto |A_p|^2 + 2|A_p A_p^{(3)}| \cos(\pi) \propto I_p - 2\sqrt{I_p I_p^{(3)}} \\ I_s^{SRG} \propto |A_s|^2 + 2|A_s A_s^{(3)}| \cos(0) \propto I_s + 2\sqrt{I_s I_s^{(3)}} \end{cases} \quad (2.44)$$

Where it clearly appears that, at resonance ( $\Omega = \Omega_R$ ), the pump intensity experiences a depletion whereas the Stokes field experiences a gain (Fig. 1.15). This is the origin of the terminologies “stimulated Raman loss” and “stimulated Raman gain.”

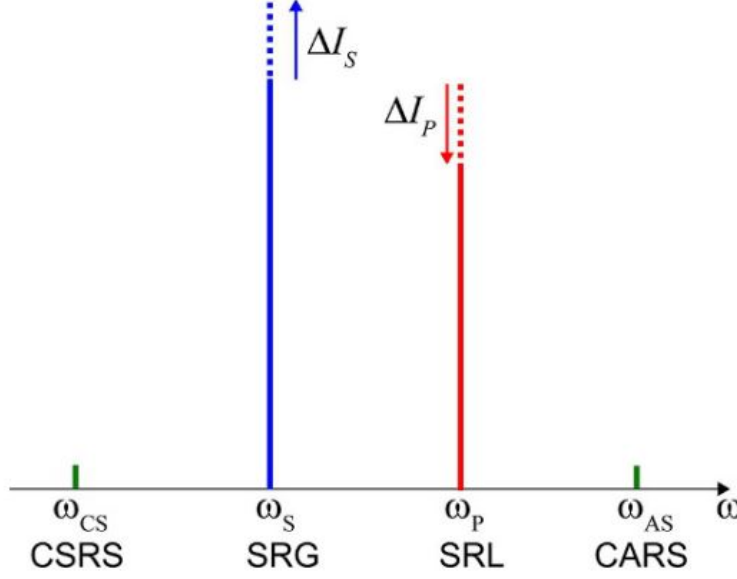


Figure 2.8: Representation of the CRS processes in the spectral domain. The dotted lines represent the intensity variation due to the SRS processes.

### 2.5.3. Bulk material

From the simple dipole, we advance to the interaction of the pump and Stokes fields within a nonlinear medium of length  $L$ . We start from the necessary propagation equations in third order non-linear medium.

In a general third-order process with four fields, where  $\omega_1 + \omega_3 = \omega_2 + \omega_4$ , starting from the Maxwell equation and remain under the slow varying envelope approximation (SVEA) the propagation equations are

$$\begin{cases} \frac{\partial A_1}{\partial z} = i f_1 A_2 A_4 A_3^* e^{i\Delta k z} \\ \frac{\partial A_2}{\partial z} = i f_2 A_1 A_3 A_4^* e^{-i\Delta k z} \\ \frac{\partial A_3}{\partial z} = i f_3 A_2 A_4 A_1^* e^{i\Delta k z} \\ \frac{\partial A_4}{\partial z} = i f_4 A_1 A_2 A_3^* e^{-i\Delta k z} \end{cases} \quad (2.45)$$

where  $f_i = 3\omega_i \chi_R^{(3)}(\omega_i) / cn_{mat}(\omega_i)$  and  $\Delta k = k_2 + k_4 - k_1 - k_3$ .

In the SRS process,  $\omega_1 = \omega_2 = \omega_p$  and  $\omega_3 = \omega_4 = \omega_s$ . This gives a huge advantage since the phase matching condition ( $\Delta k = 0$ ) is always fulfilled, therefore, the nonlinear field generated at distance  $z$  is always in phase with the nonlinear fields generated at any other distances  $z'$  in the medium.

The propagation equations now become

$$\begin{cases} \frac{\partial A_p}{\partial z} = i \frac{3\omega_p}{n_{mat}(\omega_p)c} \chi_R^{(3)}(\omega_p) |A_s(z)|^2 A_p(z) \\ \frac{\partial A_s}{\partial z} = i \frac{3\omega_s}{n_{mat}(\omega_s)c} \chi_R^{(3)}(\omega_s) |A_p(z)|^2 A_s(z) \end{cases} \quad (2.46)$$

Since the amplitude of those non-linear fields are small in comparison to the incoming one, a commonly adopted approximation is the so called "non-depletion approximation".

In this regime we state that  $A_p(z) = A_p(0)$  and  $A_s(z) = A_s(0)$ .

In this approximation equations (2.46) are simple derivative equations with exponential solution. In particular they are

$$\begin{cases} A_p(L) = A_p(0) \exp \left[ i \frac{3\omega_p}{n_{mat}(\omega_p)c} \chi_R^{(3)}(\omega_p) |A_s(0)|^2 L \right] \\ A_s(L) = A_s(0) \exp \left[ i \frac{3\omega_s}{n_{mat}(\omega_s)c} \chi_R^{(3)}(\omega_s) |A_p(0)|^2 L \right] \end{cases} \quad (2.47)$$

It is now useful to separate  $\chi_R^{(3)}$  into its real and imaginary part. Also, since  $\chi_R^{(3)}(\omega_p) = \chi_R^{(3)}(\omega_s)^*$  we set for simplicity  $\chi_R^{(3)} = \chi_R^{(3)}(\omega_p) = \chi_R^{(3)}(\omega_s)^*$ . We can thus write

$$\begin{cases} A_p(L) = A_p(0) \exp \left[ -\frac{3\omega_p}{n_{mat}(\omega_p)c} \text{Im}(\chi_R^{(3)}(\omega_p)) |A_s(0)|^2 L \right] \exp \left[ i \frac{3\omega_p}{n_{mat}(\omega_p)c} \text{Re}(\chi_R^{(3)}(\omega_p)) |A_s(0)|^2 L \right] \\ A_s(L) = A_s(0) \exp \left[ +\frac{3\omega_s}{n_{mat}(\omega_s)c} \text{Im}(\chi_R^{(3)}(\omega_s)) |A_p(0)|^2 L \right] \exp \left[ i \frac{3\omega_s}{n_{mat}(\omega_s)c} \text{Re}(\chi_R^{(3)}(\omega_s)) |A_p(0)|^2 L \right] \end{cases} \quad (2.48)$$

At this point it is interesting to look at the intensities after the interaction with the material

$$\begin{cases} I_p(L) = I_p(0) \exp \left[ -\frac{3\omega_p}{2n_{mat}(\omega_p)n_{mat}(\omega_s)\epsilon_0 c^2} \text{Im}(\chi_R^{(3)}(\omega_p)) I_s(0) L \right] \\ I_s(L) = I_s(0) \exp \left[ +\frac{3\omega_s}{2n_{mat}(\omega_p)n_{mat}(\omega_s)\epsilon_0 c^2} \text{Im}(\chi_R^{(3)}(\omega_s)) I_p(0) L \right] \end{cases} \quad (2.49)$$

In the microscopy context the length L where the SRS process is efficient (that corresponds to the volume where pump and Stokes beam are in focus), is sufficiently small for the quantity within the exponential to be much smaller than 1. Therefore, it is possible to perform the first-order development.

$$\begin{cases} I_p(L) \approx I_p(0) - \frac{3\omega_p L}{2n_{mat}(\omega_p)n_{mat}(\omega_s)\epsilon_0 c^2} \text{Im}(\chi_R^{(3)}(\omega_p)) I_s(0) I_p(0) \\ I_s(L) \approx I_s(0) + \frac{3\omega_s L}{2n_{mat}(\omega_p)n_{mat}(\omega_s)\epsilon_0 c^2} \text{Im}(\chi_R^{(3)}(\omega_s)) I_p(0) I_s(0) \end{cases} \quad (2.50)$$

Where the second terms respectively are the pump intensity loss  $\Delta I_p$  and the Stokes intensity gain  $\Delta I_s$ .

$$(2.51)$$

$$(2.52)$$

We note that these quantities are linked by  $\Delta I_p = (\omega_s/\omega_p)\Delta I_s$  and the SRS process can be viewed as an energy transfer from the pump beam toward the Stokes beam. Another feature that can be observed is that both loss and gain are proportional to  $Im(\chi_R^{(3)})$ , which is the key property that links directly SRS to spontaneous Raman [11]. So from the theory we predict the behavior that is simply observable

$$\begin{cases} (\frac{\Delta I}{I})_{SRL} \propto I_s \\ (\frac{\Delta I}{I})_{SRG} \propto I_p \end{cases} \quad (2.53)$$

## 2.6. SRS cross-section

In this section we will introduce the SRS cross-section.

We now consider equation (2.25), focusing specifically on the Raman cross-section  $\sigma_{Raman}$ . With dimensions of area,  $\sigma_{Raman}$  characterizes the strength of the interaction between light and molecules during inelastic scattering. The numerical values of  $\sigma_{Raman}$  are significantly smaller, by several orders of magnitude, than the linear absorption cross-sections  $\sigma_{Absorption}$  of similar molecular systems. This enormous gap has historically led researchers to view Raman scattering as an extremely weak phenomenon ever since its discovery.

### 2.6.1. Spontaneous Raman cross-section

Before proceeding, it is important to clarify a conceptual error in making this comparison. Linear absorption and Raman scattering belong to different orders of light-matter interaction. Specifically, linear absorption is a first-order process, governed by  $\chi^{(1)}$ , where there is one input field and one output field. In contrast, Raman scattering is a third-order nonlinear process, governed by  $\chi^{(3)}$ , where two input fields (input pump and Stokes) and two output fields (output pump and Stokes) are involved. This distinction explains the need for using the three-wave mixing propagation equation in Raman scattering.

However, spontaneous Raman scattering is a special case. In this process, the Stokes input field is empty, and we observe the transfer of photons from the pump input field to

the Stokes output field. In spontaneous Raman scattering,  $\sigma_{Raman}$  represents the power  $P_s$  (measured in  $J/s$ ) scattered into the Stokes channel, divided by the incident intensity of the pump beam (measured in  $J/s \cdot cm^2$ ). This relationship is expressed as:

$$\sigma_{Raman} = \frac{P_s}{I_p} \quad (2.54)$$

This conceptualization, where only one input field and one output field are taken into account, allows us to treat the process as 'virtually' linear. This makes it reasonable to compare  $\sigma_{Raman}$  with  $\sigma_{Absorption}$ . However, even for similar molecules,  $\sigma_{Raman}$  can be 8 to 14 orders of magnitude smaller than  $\sigma_{Absorption}$ , as shown in Fig. 1.2. This vast difference is one reason why Raman scattering was only observed relatively late, in 1928 [19], and why it has traditionally been considered a weak process in the literature.

### 2.6.2. SRS cross-section introduction

Until recently, there has not been a distinct parameter to describe the strength of Stimulated Raman Scattering (SRS), apart from the standard  $\sigma_{Raman}$ . While this parameter is useful for spontaneous Raman scattering, it is insufficient for SRS for two key reasons. The first, as discussed earlier, is that SRS is a third-order nonlinear effect, and unlike spontaneous Raman scattering, it cannot be approximated as a linear process. Consequently, comparing  $\sigma_{Raman}$  for SRS with linear absorption cross-sections lacks a conceptual sense. The second reason regards the numerical value implied. SRS is for sure not a weak process when compared to its electrical counterparts of the same order. Furthermore the same molecule can give rise to a small spontaneous signal and a strong stimulated signal, so there is no reason in using the same parameter  $\sigma_{Raman}$  to describe both[17]. The necessity of a new parameter is thus evident. We will follow from now on the reasoning and mathematical developments performed by Xin Gao and Wei Min in their recent papers[9, 17]. We took now into consideration one of the SRS electrical counterpart cited before. In particular we will focus and take inspiration from the two-photon absorption (TPA). Predicted by Maria Goöppert-Mayer in 1931 in her dissertation[10] and later observed in 1961[12]. TPA involves the simultaneous absorption of two lower-energy photons via short-lived intermediate states. As a result, the molecule is excited from the ground state to a higher energy electronic state. The TPA rate (unit in *photon/s*) of a given molecule is often described as

$$rate_{TPA} = \sigma_{TPA} \cdot \Phi^2 \quad (2.55)$$

where  $\sigma_{TPA}$  is defined as the TPA cross-section of the molecule[2, 25] and  $\Phi$  is the photon flux (unit in  $photons/s \cdot cm^2$ ), denoting the number of photons crossing a unit area per unit time, and is related to the beam intensity  $I$  by the photon energy  $\Phi = \frac{I}{h\nu}$ . The measurement unit of  $\sigma_{TPA}$  is GM(Göppert-Mayer), named after its prediction, where  $1GM = 10^{-50}cm^4 \cdot s$ . They proposed, in a very similar rate equation, an equation for the SRS rate, defined as the rate (unit in  $photon \cdot s^{-1}$  of ) photons generated via SRS excitation for one oscillator. This  $rate'_{SRS}$  is given by the equation

$$rate'_{SRS} = \sigma_{SRS} \cdot \Phi_p \cdot \Phi_s \quad (2.56)$$

This equation is just a renewed version of  $\Delta I_{SRS} \propto I_p I_s$  where the intensity variation is converted into a photons rate, the initial intensities into photons fluxes and all the constants and physical properties of the material are grouped into the  $\sigma_{SRS}$ . Extending equation (2.56) describing a single scatterer to a collection of scatterers within the excitation volume, we will have

$$rate_{SRS} = n \cdot \sigma_{SRS} \cdot \Phi_p \cdot \Phi_s = [c] \cdot V \cdot N_a \cdot \sigma_{SRS} \cdot \Phi_p \cdot \Phi_s \quad (2.57)$$

where  $n$ ,  $[c]$ ,  $V$  and  $N_a$  are the number of scatterers (adimensional), concentration ( $mol/L$ ), effective focal volume ( $L$ ), and Avogadro's number, respectively.

This new  $\sigma_{SRS}$ , in unit of GM, can now be fairly compared to  $\sigma_{TPA}$ , giving us an idea of the effective strength of the SRS process. A significant and unexpected finding is that  $\sigma_{SRS}$  compares favorably or can even surpass the electronic counterpart  $\sigma_{TPA}$ , as we can see in Fig. 2.9, in contrast to the prevailing perspective between  $\sigma_{Raman}$  and  $\sigma_{Absorption}$ .

### 2.6.3. Stimulated VS spontaneous Raman cross-section

It is now interesting to explore the link between the old and well known  $\sigma_{Raman}$  and this recently introduced  $\sigma_{SRS}$ . We start this procedure looking at the spontaneous Raman process under a different perspective. We will no longer consider the spontaneous Raman as a 'virtual' linear process, but we will start to consider it as the non-linear process that really is, in particular as a SRS process. At the first sight this could seem senseless since there is no Stokes field that can stimulate the process. We will now briefly consider once again an electrical counterpart, the spontaneous emission. When an atom in the vacuum is in an excited state, even though the electron is in an eigenstate of the atom, this will spontaneously decay. This phenomena takes place due to the ground-zero oscillation interacting, thanks to a virtual photon, with the atom. The idea for spontaneous Raman

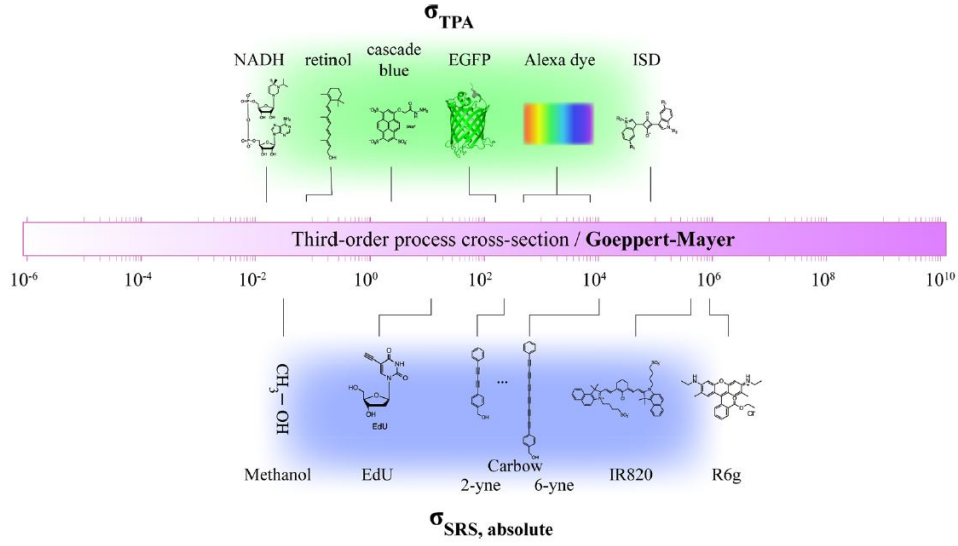


Figure 2.9: Comparison of  $\sigma_{TPA}$  and  $\sigma_{SRS}$  under the common GM framework. We can note how the two share a large window of value contrarily to their spontaneous counterpart [9]

is the same. We look at spontaneous Raman as an SRS process, where the Stokes role is played by the **vacuum oscillations**. In this vision equation (2.25) can be rewritten as

$$rate_{Raman}(\omega_s) = n \cdot \sigma_{SRS}(\Omega_R) \cdot \Phi_p \cdot \Phi_{vacuum} \quad (2.58)$$

where  $\Phi_{vacuum}$  is the contribution of the vacuum oscillation to the process. Maybe one could think, just for ease, at this  $\Phi_{vacuum}$  as a virtual photon flux, but this should be done with caution since we are mixing the concept of virtual photon, purely quantum, and a photon flux, used in classic vision. Anyway comparing equation (2.25) with (2.58) we can retrieve an important equation[16]

$$\sigma_{Raman}(\omega_s) = \sigma_{SRS}(\Omega_R = \omega_p - \omega_s) \cdot \Phi_{vacuum} \quad (2.59)$$

This important link allows us to understand better this duality of Raman.[17] Considering typical values for SRS experiments, it turns out that  $\Phi_{vacuum}$  is many orders of magnitude weaker than the peak photon flux produced by a typical pulsed Stokes beam at the microscope focus. Empirically, this “Stokes power” provided by vacuum fluctuation is about microwatt level, much lower than that in stimulated Raman experiments. Hence, it is the feeble  $\Phi_{vacuum}$  that makes  $\sigma_{Raman}$  appear so small and allows the contemporaneous presence of small  $\sigma_{Raman}$  and big  $\sigma_{SRS}$  in the same molecule. The expression for  $\Phi_{vacuum}$

is

$$\Phi_{Vacuum} = \frac{\omega_s \Gamma}{2\pi c^2 \omega_p} \quad (2.60)$$

where  $\Gamma$  is the FWHM of the peak, assuming a Lorentzian shape[17] .

#### 2.6.4. SRS cross-section measurement

We now focus on how to measure the  $\sigma_{SRS}$  starting from an usual SRS measurement set up. Normally when a SRS measurement is performed, the quantity taken into account is the  $\frac{\Delta I}{I}$  where  $\Delta I$  is the intensity variation due to the SRS process and  $I$  is the input intensity. Those value correspond to the Pump laser or to the Stokes one, depending on which process we are taking into account, respectively SRL or SRG. Without loss of generality we will now consider the SRG process, since is the one we will work on in this thesis. We start from an equivalence

$$\left( \frac{\Delta I}{I} \right)_{SRG} = \frac{rate_{SRS}}{\Phi_{Stokes} \cdot A} \quad (2.61)$$

Where  $A$  denote the effective area of the incident laser beams. The idea of equation (2.61) is that the normalized difference in the intensity is equal to the normalized difference of number of Stokes photons per second. Substituting equation (2.57) in (2.61) we obtain

$$\left( \frac{\Delta I}{I} \right)_{SRG} = \frac{[c] \cdot N_a \cdot V \cdot \sigma_{SRS}(\Omega) \cdot \Phi_p \cdot \Phi_s}{\Phi_s \cdot A} \quad (2.62)$$

At this point we can simplify the  $\Phi_s$  and isolate  $\sigma_{SRS}(\Omega)$

$$\sigma_{SRS}(\Omega) = \left( \frac{\Delta I}{I} \right)_{SRG} \cdot \frac{A}{[c] \cdot N_a \cdot V \cdot \Phi_p} \quad (2.63)$$

We now consider the fact that  $\Phi = P/h\nu$ , but we have to be careful. The power of the laser is often given or measured (with a powermeter) as the **average** power  $P_{ave}$ . What we should consider instead is the power arriving really at the sample so the **peak** power  $P_{peak}$ . So the correct expression to consider in (2.63) for  $\Phi_p$  is

$$\Phi_p = \frac{P_{p,peak}}{Ah\nu_p} = \frac{P_{p,ave}}{h\nu_p \tau RR} \quad (2.64)$$

where  $\tau$  is the temporal duration of the laser and  $RR$  is the repetition rate of the laser. The product  $\tau RR$  can be interpreted as a duty cycle. Substituting (2.64) into (2.63), and

considering the equivalence  $\nu = c/\lambda n_{mat}$ , we obtain the final expression

$$\sigma_{SRS}(\Omega) = \left( \frac{\Delta I}{I} \right)_{SRG} \cdot \frac{A^2 \tau R R h c}{[c] N_a V P_{p,ave} \lambda_p n_{mat}} \quad (2.65)$$

This is the equation we will start from in the next chapter.



# 3 | Filling Factor

We concluded the previous chapter with equation (2.65) where it is stated that the SRS cross-section  $\sigma_{SRS}$  requires the ratio  $\Delta I/I$  for its measurement. In this chapter, we will introduce a new corrective factor to take into account in order to precisely retrieve the  $\Delta I/I$  when a lock-in amplifier is involved for the measurement. This has, without a doubt, relevance in all situations where the lock-in is used to measure modulated energy variation in lasers, but on the path towards quantified SRS measures, it acquires even more relevance. For reasons that will be clarified within the chapter, we decided to name this correction as **Filling Factor** (FF)

## 3.1. Lock-in amplifier

As we saw in Chapter 2 the SRS signal effectively corresponds to a relative variation in the laser intensity, in particular to an increment of the Stokes and a decrease in the pump. One could assume to retrieve this variation easily, for example by using a power meter to measure directly the power variation or connecting a photodiode to an oscilloscope and look at the voltage variation. Those solutions are unfortunately not sufficient. The reason is that even if the SRS process is up to 7 orders of magnitude with respect to the spontaneous, typical value for  $\Delta I/I$  are in the orders of  $10^{-4} - 10^{-5}$ , that is not appreciable at all with the cited techniques. Also we must consider that such a small quantity sometimes could be just slightly bigger or comparable with the system noise. The solution adopted is to perform a measurement with a lock-in amplifier.

### 3.1.1. Lock-in working principle

Consider now for simplicity an input signal  $V_{in} = A \cdot \cos(\omega t + \theta)$ . To characterize it, we need to retrieve  $A$  and  $\theta$ . The lock-in will multiply, separately, the signal by two reference sinusoidal signals at the same angular frequency of  $V_{in}$ , shifted by  $\frac{\pi}{2}$  one from each other. We can assume, without loss of generality, a cosine and a sine with unitary amplitude:  $V_{refX} = \cos(\omega t)$  and  $V_{refY} = \sin(\omega t) = \cos(\omega t + \frac{\pi}{2})$ . We will achieve two signals

$$\begin{cases} X' = V_{in} \cdot V_{refX} = \frac{A}{2}\cos(2\omega t + \theta) + \frac{A}{2}\cos(\theta) \\ Y' = V_{in} \cdot V_{refY} = \frac{A}{2}\cos(2\omega t + \theta + \frac{\pi}{2}) + \frac{A}{2}\cos(\theta + \frac{\pi}{2}) \end{cases} \quad (3.1)$$

Both signals are now composed by a term oscillating at a frequency that is the double of the initial frequency  $2\omega$ , and a constant term. Those signals then pass through a low-pass filter (LPF) in order to isolate the constant terms (Fig. 3.1). Naturally it requires that the bandwidth of the LPF is smaller than  $2\omega$ . Once this condition is satisfied, we remain with the following terms

$$\begin{cases} X = \frac{A}{2}\cos(\theta) \\ Y = \frac{A}{2}\cos(\theta + \frac{\pi}{2}) = \frac{A}{2}\sin(\theta) \end{cases} \quad (3.2)$$

We can finally retrieve the information required by using simple trigonometric equations

$$\begin{cases} A = 2\sqrt{X^2 + Y^2} \\ \theta = \operatorname{tg}^{-1}\left(\frac{X}{Y}\right) \end{cases} \quad (3.3)$$

In a real case naturally we will never have a pure sinusoidal signal as input, but every signal, from the fourier theory [3], can be seen as an infinite sum of sinusoidal terms. The lock-in purpose is to extract the component at the reference frequency. Naturally the lock-in will not extract precisely that frequency, but also all the frequency around it in a window wide as the LPF width. Therefore, there is a trade-off between precision and measurement time, since the latter is proportional to the inverse of the LPF width. Just for a matter of nomenclature, this extraction of a single frequency is called demodulation, and the reference signal is called demodulation reference.

### 3.1.2. Lock-in for $\Delta I$ measurement

As we said before the typical values for  $\Delta I$  are up to 4-5 orders of magnitude smaller with respect to the intensity  $I$ . Involving a lock-in is a smart solution since it allows one to extract just the signal cutting away all the others frequencies, that are just noise. We must understand at which frequency the signal is. If we use just pulses with constant amplitude the SRS signal will be just a constant increase, so with frequency  $\omega = 0$ . In this case the demodulation reference will be just a unitary constant signal, and the LPF would extract the zero frequency. Note that in this case we could substitute the lock-in and use just an integrator. The real problem in using the zero frequency is noise. Typically noise

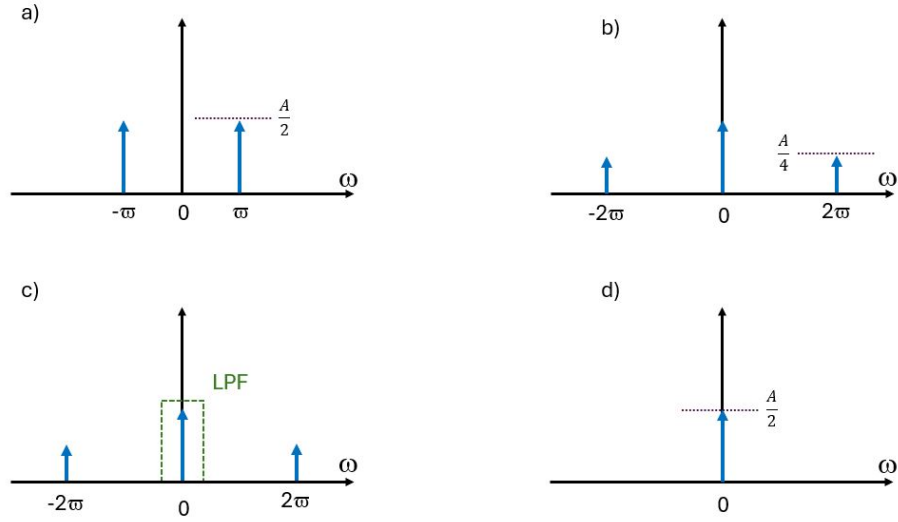


Figure 3.1: Lock-in operation in the spectrum domain. Note that also the negative frequencies are considered. a) Spectrum representation of  $V_{in}$  b) Signal after the multiplication for the reference one ( $X'$ ) c) LPF action d) Output of the lock-in ( $X$ )

is composed by a white noise, that is constant for all the frequencies, and a  $\frac{1}{f}$  noise (Fig. 3.2). As the name can suggest  $\frac{1}{f}$  noise increase in the small frequency region. Leaving the signal, and so extract it, at the zero frequency would make the measurement really noisy.

The solution is to modulate the SRS signal at a certain frequency where the noise is low, and then demodulate it with the lock-in. To better understand how to modulate the SRS signal we now consider the SRG process. The idea is to modulate the pump  $I_p = I_p^0 \cdot \cos(\omega t)$  while keeping the Stokes constant  $I_s = I_s^0$ . From the theory we know that  $\Delta I \propto I_p I_s \propto I_p^0 I_s^0 \cos(\omega t)$ . Therefore the Stokes intensity after the material will be made of a small oscillating signal ( $\Delta I$ ), plus a big constant one ( $I$ ). Demodulating the Stokes signal at  $\omega$ , the lock-in extracts just the  $\Delta I$  cutting away the  $I$ . In SRL process we modulate the Stokes and keep the pump constant, demodulating the pump.

## 3.2. Introducing a corrective factor: the filling factor

We now consider a practical scenario where a pulsed laser is used to perform SRG. The laser pulses are detected with a photodiode, and the generated signal is sent to the lock-in amplifier. Since photodiodes lack the bandwidth to resolve picosecond pulses (requiring THz bandwidth, while current technology reaches only GHz), we model the pulse train as a series of delta functions. Because of this, the photodiode's output will represent a train of its own pulse response,  $h(t)$ . Consider now the case where the photodiode bandwidth

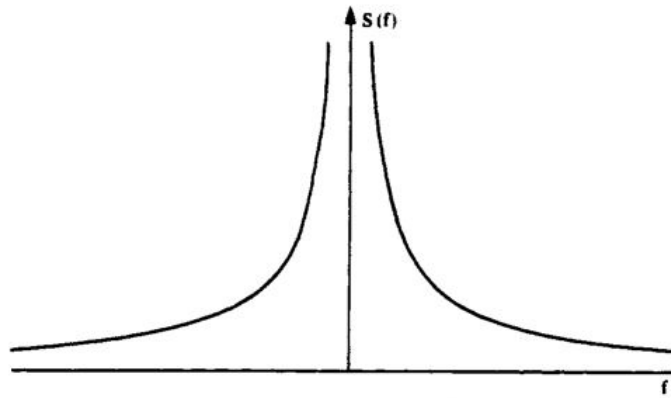


Figure 3.2: Typical shape of  $1/f$  noise in frequency domain. We can note how in the low frequency region the noise increases, contrarily to the white noise that remains constant everywhere. [13]

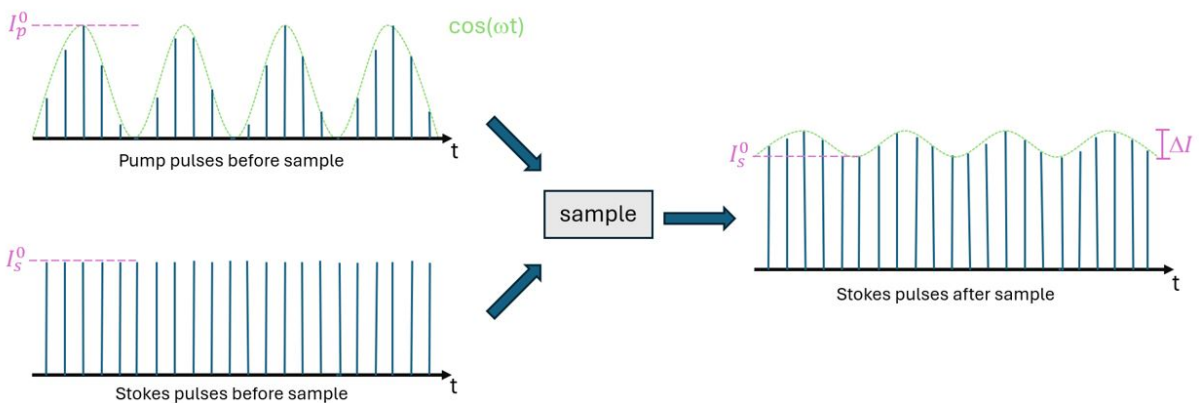


Figure 3.3: Scheme of the pulses intensities in a modulated SRG process.

is bigger than the laser repetition rate. The resulting signal at the photodiode, let us call it  $S(t)$ , thus consists of a sequence of  $h(t)$  responses, with a small sinusoidal modulation in their amplitudes, as shown in Fig. 3.4a. The key information we aim to extract with the lock-in amplifier is the peak-to-peak amplitude of this sinusoidal modulation.

Consider a scenario in which, instead of the pulsed signal  $S(t)$ , there is a *filled signal* represented by the modulation sinusoid raised by a pedestal, the value of  $I_s^0$  (Fig. 3.4b). In this case, the lock-in amplifier would accurately retrieve its full amplitude. However, when analyzing the actual pulsed signal  $S(t)$ , the amplitude retrieved will be **smaller**. This reduction occurs because, as previously discussed, the lock-in operation involves multiplying the input signal by a reference sinusoid followed by integration (the low-pass filter operation). In the ideal case, we are multiplying two sinusoidal signals, demodulation and modulation, which align to give a maximal response. In contrast, with the real signal  $S(t)$ , the lock-in multiplies a modulated pulse train by the reference sinusoid. Since the pulse train amplitude is often less than that of the modulation sinusoid (and can even be zero for extended periods, depending on the shape of  $h(t)$ ), the outcome of this integral will inevitably be smaller than in the *filled signal* case.

The ratio between the first and the second result is the **Filling Factor**. The name comes from the fact that multiplying the lock-in measurement for this Filling Factor (FF) we retrieve the amplitude of that *full* sinusoid that is our real aim.

At first sight this could seem irrelevant since up to now we just said to correct the measurement by multiplying the inaccurate result by the ratio of the correct and incorrect values. It's important to remember that the lock-in amplifier is used specifically when direct access to accurate values is impossible, leading us to ask how to determine the filling factor (FF). The answer lies in a useful property of the FF: it is independent of both amplitude modulation and the pedestal height  $I_s^0$ , and so on their ratio, depending only on the shape of  $h(t)$  and the modulation frequency. Details in Appendix A. This property allows us to calculate the FF before the SRG experiment by using a dummy signal with high modulation. In this setup, the correct *full* amplitude is easily observed with an oscilloscope, enabling the FF calculation. We then proceed with the actual experiment, where the modulation is small, measuring the inaccurate amplitude with the lock-in and finally applying the pre-calculated FF to retrieve the correct amplitude.

In the next section we will present the set-up made ad hoc in order to create those dummy signal trying to reproduce the shape of a real SRS signal. Basically we can see the SRS signal as formed by two different component: the pedestal and the top modulated signal. The ratio between the first and the second is the  $\Delta I/I$ . We will firstly present all the set-

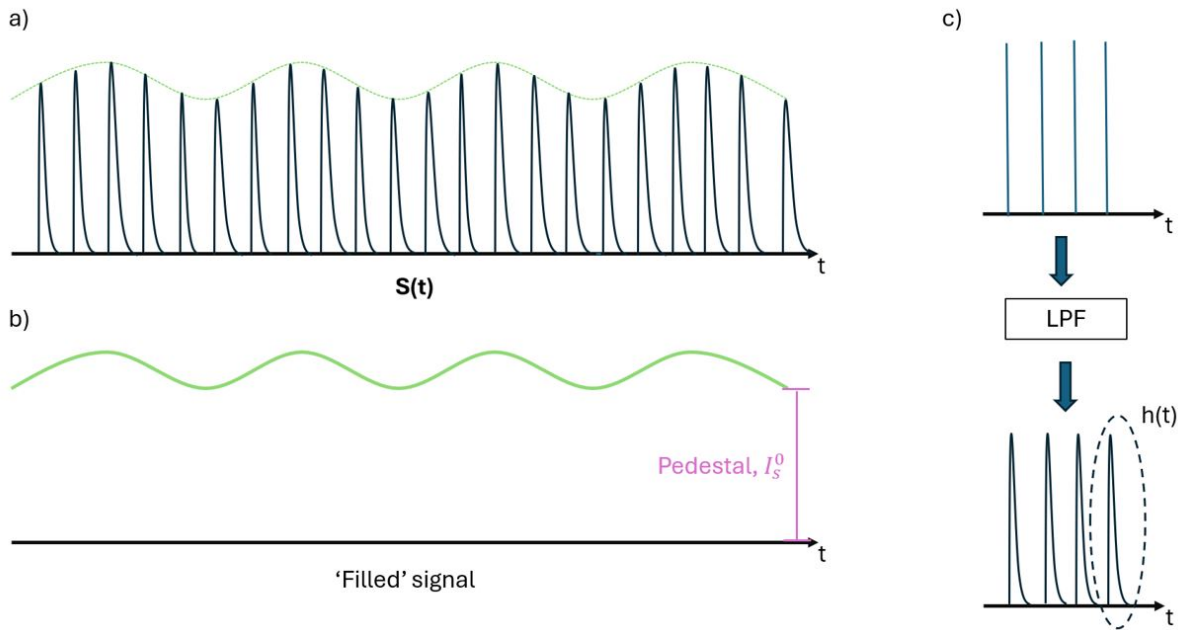


Figure 3.4: a)  $S(t)$ . We can see the train of  $h(t)$  with the small modulation b) The *filled* signal. Is the modulation signal raised by a pedestal c) The action of a LPF that transform a delta into is pulse response  $h(t)$

up components. We will then go through the practical FF measure step-by-step. Finally we will present the data analysis trying to show how the FF does not vary while changing  $\Delta I/I$ , and in particular to show how the FF acquires importance while decreasing the  $\Delta I/I$  ratio.

### 3.3. Experimental set-up for FF measurement

In Fig. 3.5 we can observe the set-up used for the experiment. The principal elements are:

- Pulsed laser
- Beam splitter (BS)
- Acusto-optic moulator (AOM)
- Delay line
- Neutral density attenuator
- Photodiode
- Oscilloscope

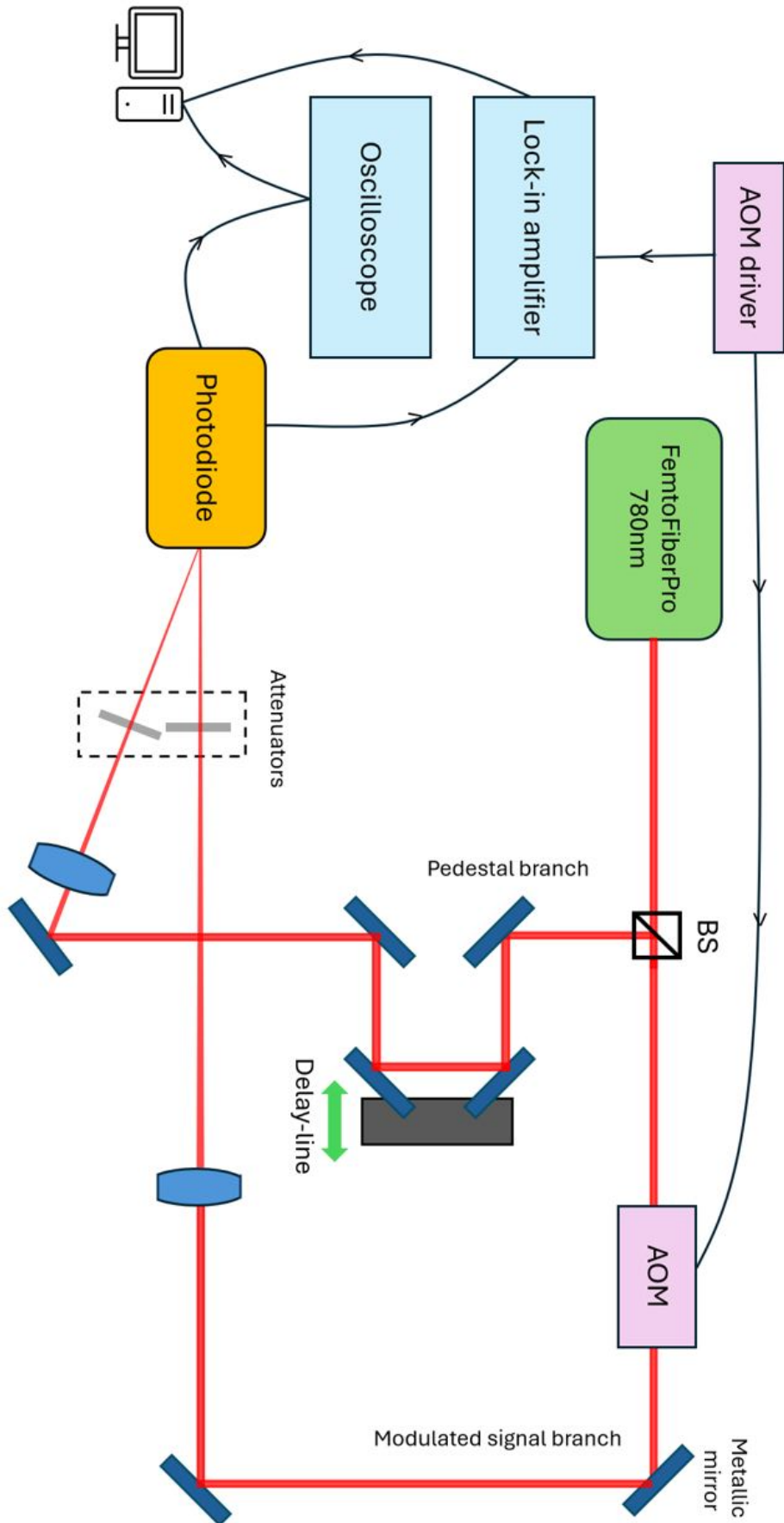


Figure 3.5: Set-up implied for the FF measurements. BS = Beam Splitter.

- Lock-in amplifier

The underlying idea is to split the beam in two, with the BS, in order to have separate control of the pedestal and the modulated part. The starting point is the laser. It is used the *FemtoFiber ProM40* from Toptica Photonics. It is a erbium fiber laser with emission wavelength at  $1560nm$ , capable to perform internally the second harmonic generation (SHG). Due to wavelength response of the employed photodiode, the  $780nm$  beam is used. The first beam branch is responsible for the pedestal. In this branch, the beam travels through a delay line, which is critical, as constructing the dummy signal requires the precise temporal overlap of two pulses. This overlap allows the photodiode to detect only a single pulse, as it would in the actual SRS case. Without temporal overlap, the photodiode would detect two separate delta signals, resulting in a signal that is wider and shorter than the desired simple  $h(t)$ . The beam then passes through a lens, ensuring that it reaches the photodiode in a nearly collimated state, and through an attenuator to control the pedestal amplitude and prevent potential damage to the detector. The second branch is the one responsible for the modulated part. The beam passes from an acousto-optic modulator (AOM-80-D from A.P.E) capable of modulate the signal from 10KHz to 10MHz. Again the pulse the passes through a lens and an attenuator for the same reasons as the other branch. The photodiode employed is the OE-300-SI-30 from FEMTO, is a photodiode with variable gain and bandwidth (see Fig. 3.6) very useful for our purpose. The wavelength detected are between  $320nm$  and  $1000nm$ . Finally there are the oscilloscope (HDO6104 from Teledyne Lecroy) and the lock-in amplifier (H2FLI-50 from Zurich Instrument) to collect the data. Data are then analyzed digitally from a PC.

### Acousto-optic modulator

Acousto-optic modulators (AOMs) are useful devices which allow the frequency, intensity and direction of a laser beam to be modulated. AOMs are based on made an acoustic wave travel through a crystal. The reason behind is that sound waves travelling through a crystal can be modelled as crests of increased refractive index alternating with troughs of decreased refractive index. Light incident on gradients in refractive index is scattered, therefore the light scatters from the acoustic wavefronts. Modulation of this incoming light can be achieved by varying the amplitude and frequency of the acoustic waves traveling through the crystal.[6]

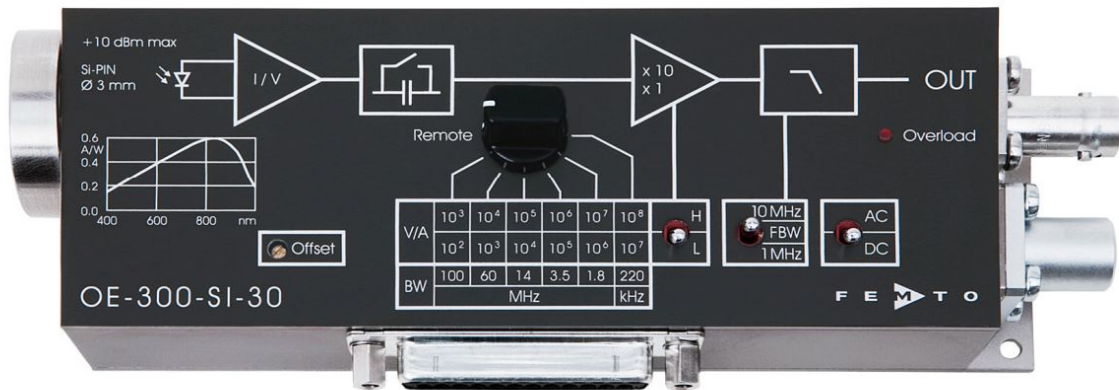


Figure 3.6: The OE-300-SI-30 photodiode. We can observe the different gains and relative bandwidth

## Delay line

To achieve temporal overlap between the two branches it was used a simple method. The laser trigger was connected to the oscilloscope in order to obtain a fixed oscilloscope triggering. Then the first branch was sent into the photodiode and the temporal position of one pulse was fixed with a cursor. Then was send the second branch, no pulses was aligned with the cursor, but this was not surprising since the two had different optical path. At this point the delay line was manually shifted, thanks to a micrometer translation stage, up to when one pulse was overlapped with the cursor. The precision that could be reached was given by the oscilloscope sampling. The sampling was  $2.5 \text{ Gsample/s}$ , giving us a precision of  $400 \text{ ps}$ . That was considered acceptable since the maximum photodiode bandwidth used was  $100 \text{ MHz}$ , so not sufficient to appreciate that delay between pulses.

## 3.4. Experimental results

In the first part of this chapter we talked about the case when the photodiode bandwidth (BW) is bigger than the laser repetition rate (RR). In this case it is easy to observe that the pulsed nature of the beam leads to an *empty* signal (Fig. 3.4a) with respect to the modulation sinusoid, and so we used that case for the FF introduction. There is however also the case where the photodiode bandwidth is much smaller than the RR. In this situation the output of a train of constant deltas would be a constant and the output of a train of modulated deltas would be a simple sinusoid raised up, like the ideal *full* signal. Note that the bandwidth has to be much smaller than the RR but bigger

than the modulation frequency  $\omega$  in order to not cut away also it. At this point one could argue that the FF in this last case is useless. So we decided to observe the behavior of FF in three different scenario:

- 1)  $BW > RR \gg \omega$
- 2)  $RR > BW \gg \omega$
- 3)  $RR \gg BW > \omega$

that are the two cases presented and an intermediate one. For any of those cases were taken into account different value of the ratio: sinusoid amplitude/total amplitude. In particular the *modus operandi* is to calculate the FF in the case of 100% ratio (no pedestal), then we use it in the other ratio scenarios to retrieve the amplitude modulation starting from the lock-in measurement and finally check how much the measure from the oscilloscope its close to our measurement.

Before presenting the data acquired we must talk about a detail in the lock-in measurement, that must be took into account. What we are interested in, is the the peak-to-peak amplitude while what the lock-in returns is the amplitude of oscillation, also the lock-in used in our set-up returns the rms value. So even if we give the lock-in a perfect sinusoid with a peak-to-peak amplitude  $A$ , this would return a value of  $A/2\sqrt{2}$ . The FF intrinsically incorporates this  $2\sqrt{2}$  term.

The modulation frequency chosen is  $\omega = 400KHz$ . This value was chosen since it was suitable for all the three cases. The repetition rate was 40 MHz.

### 1) $BW = 100MHz$

Since our aim is also to provide a sort of tutorial on how to handle the FF, for this first case we will proceed step by step, instead for the other cases we will present just the data.

We start from the 96% case. In this case the pedestal was completely missing, anyway the modulation ratio was not exactly 100% due to the AOM non-ideality. The first step is to acquire the sinusoidal amplitude with the oscilloscope. This is a key point since we will use it for the FF calculation. In order to be the most precise possible is suggested to use any source that can improve the measurement. In this case it was used the oscilloscope internal function of averaging to acquire the signal. Those data were then analyzed with Matlab to extract the peak-to-peak amplitude. In this case the peak to peak amplitude was  $A_{1_{os}} = 359.3mV$ . The lock-in returns a demodulation value of  $A_{1_{i}} = 20.9mV$ . We can start to see how this last measurement lack of something. The filling factor is therefore

calculated as the ratio of the two and it was  $FF = \frac{A_{1os}}{A_{1li}} = 17.19$ . At this point, in order to change arbitrarily the ratio, both the pedestal and the modulated signal intensity were controlled thanks to the attenuators. In the second case, with 72% ratio, we started instead from the lock-in measurement,  $A_{2li} = 19.61mV$ . We multiply this value for the FF achieving a value of  $A_{2cal} = A_{2li} \cdot FF = 337.1mV$ . If we compare this value with the one acquired from the oscilloscope,  $A_{2os} = 338.6mV$  we can note how it is very similar to  $A_{2cal}$ , and that was what we were expecting. We now repeat the procedure for other two ratios. In the third case the ratio was 46%. The lock-in measurement was  $A_{3li} = 7.14mV$ , and so  $A_{3cal} = 122.7mV$ . The oscilloscope measurement was  $A_{3os} = 115.2mV$  Finally the last case, with a very small 1.25% ratio, gives  $A_{4li} = 2.26mV$ . The calculated value was  $A_{4cal} = 11.8mV$  and the oscilloscope measurement is  $A_{4os} = 9.4mV$  In the following images we can see the different ratio tracks. Image elaboration has been performed with custom made software in Matlab V2024. We can clearly see the 400KHz modulation. The sinusoid seems colored, but this is just a graphical effect due to the fact that below the sinusoid there are all the laser pulses. To better understand in Fig. 3.7 a zoom is presented, and the pulsed nature is easily observable.

Ratio	Lock-in measure	Oscilloscope measure	FF
96%	20.9 mV	359.3 mV	17.19
Ratio	Lock-in measure	Calculated value	Oscilloscope measure
72%	19.61 mV	337.1 mV	338.6 mV
46%	7.14 mV	122.7 mV	115.2 mV
1.25 %	686.4 $\mu$ V	11.8 mV	9.4 mV

Table 3.1: Data for the 100 MHz photodiode bandwidth

### Peak-to-peak calculation

As we said before, acquiring the peak-to-peak amplitude precisely is a key point. In order to do this, a Matlab post-processing was performed. the first step performed was to retrieve the modulation shape forgetting about the pulsed nature. In order to do this, for every pulse the peak was acquired. At this point what remains is just the modulation amplitude (Fig. 3.11)from which the peak-to-peak amplitude can be retrieved. Unfortunately in our set-up the laser presents other modulation and this is the reason why the modulation peak are not constant. In Fig. 3.12 is presented an image of just the pedestal where the laser intrinsic modulation can be observed. In order to overcome this issue, as maximum value for the peak-to-peak measure, the mean of the different

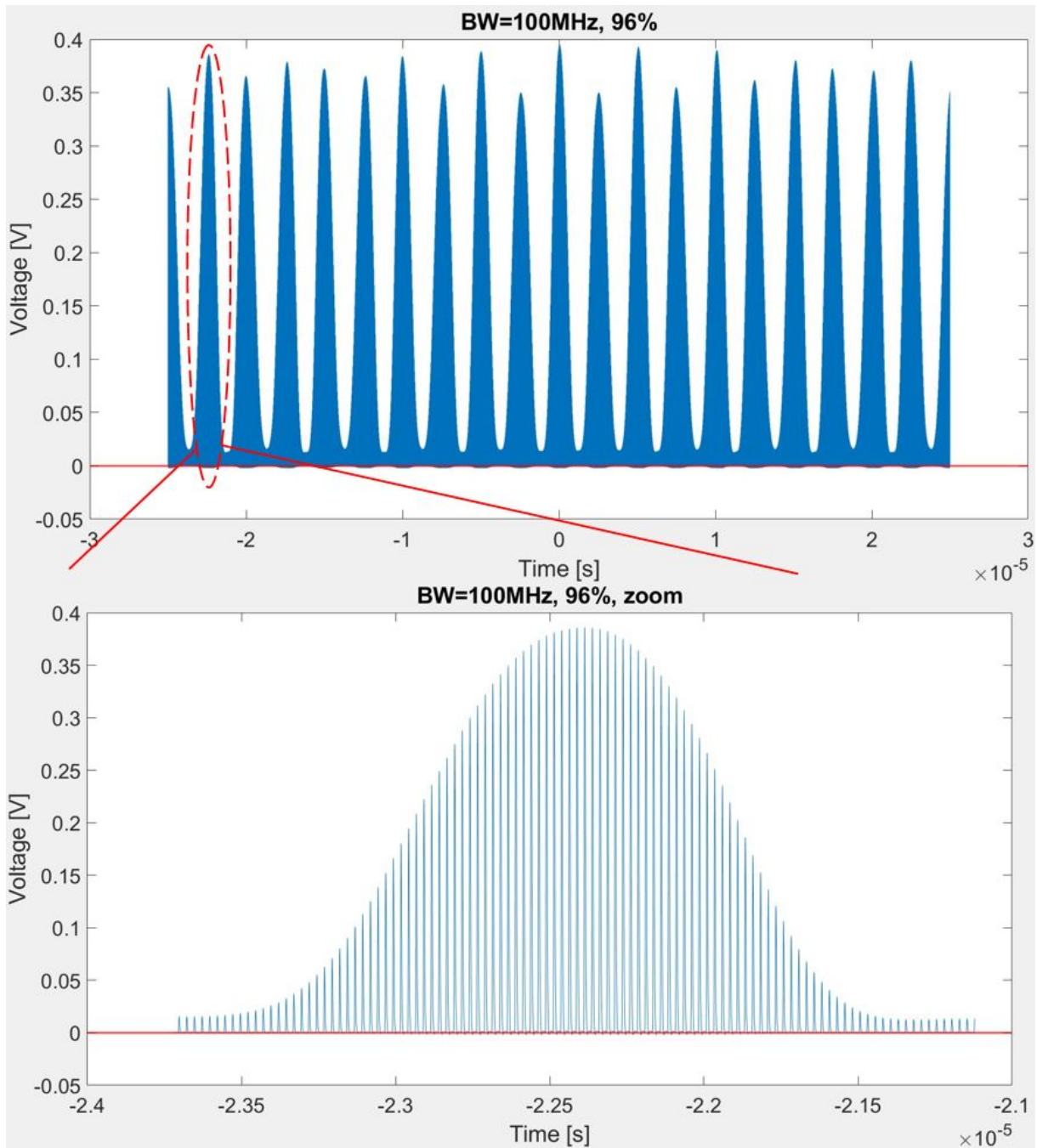


Figure 3.7: Oscilloscope track in the case of 100 MHz BW and 97% ratio

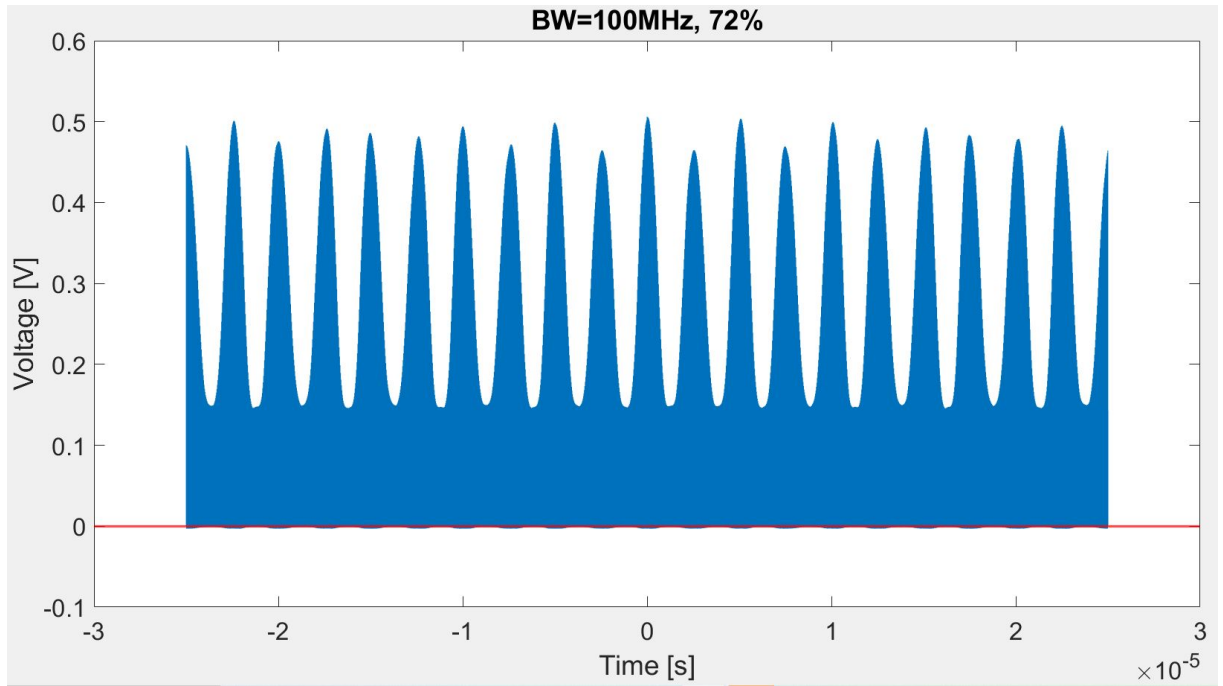


Figure 3.8: Oscilloscope track in the case of 100 MHz BW and 72% ratio

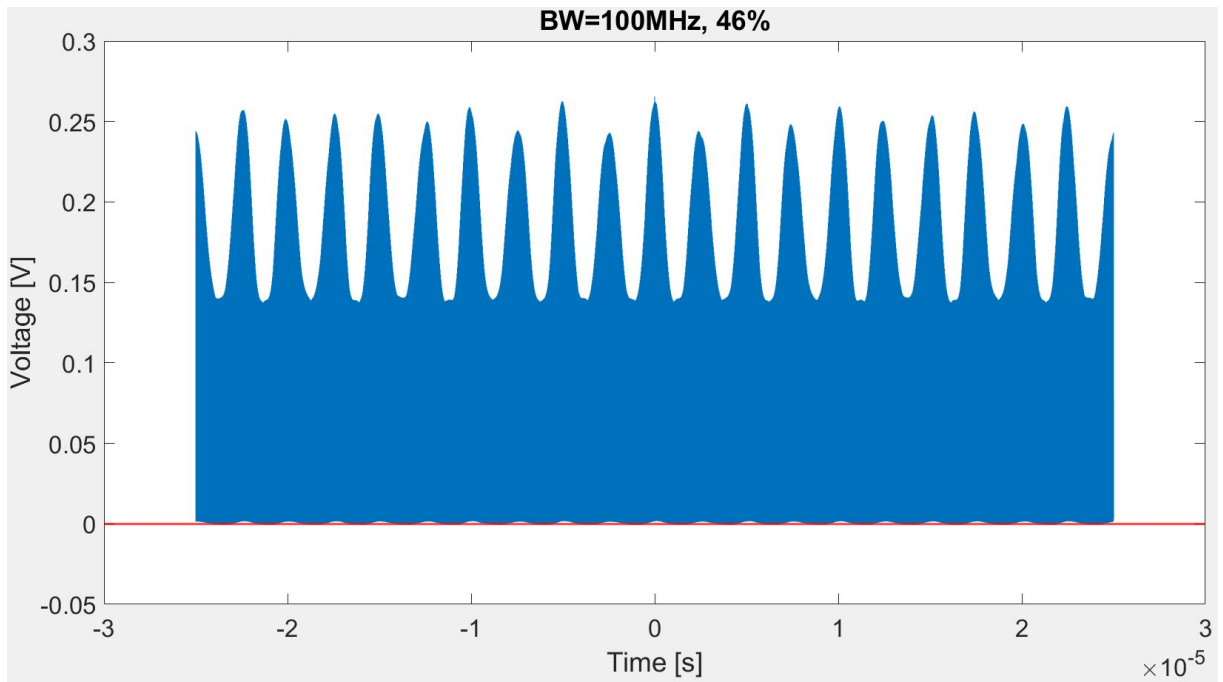


Figure 3.9: Oscilloscope track in the case of 100 MHz BW and 46% ratio

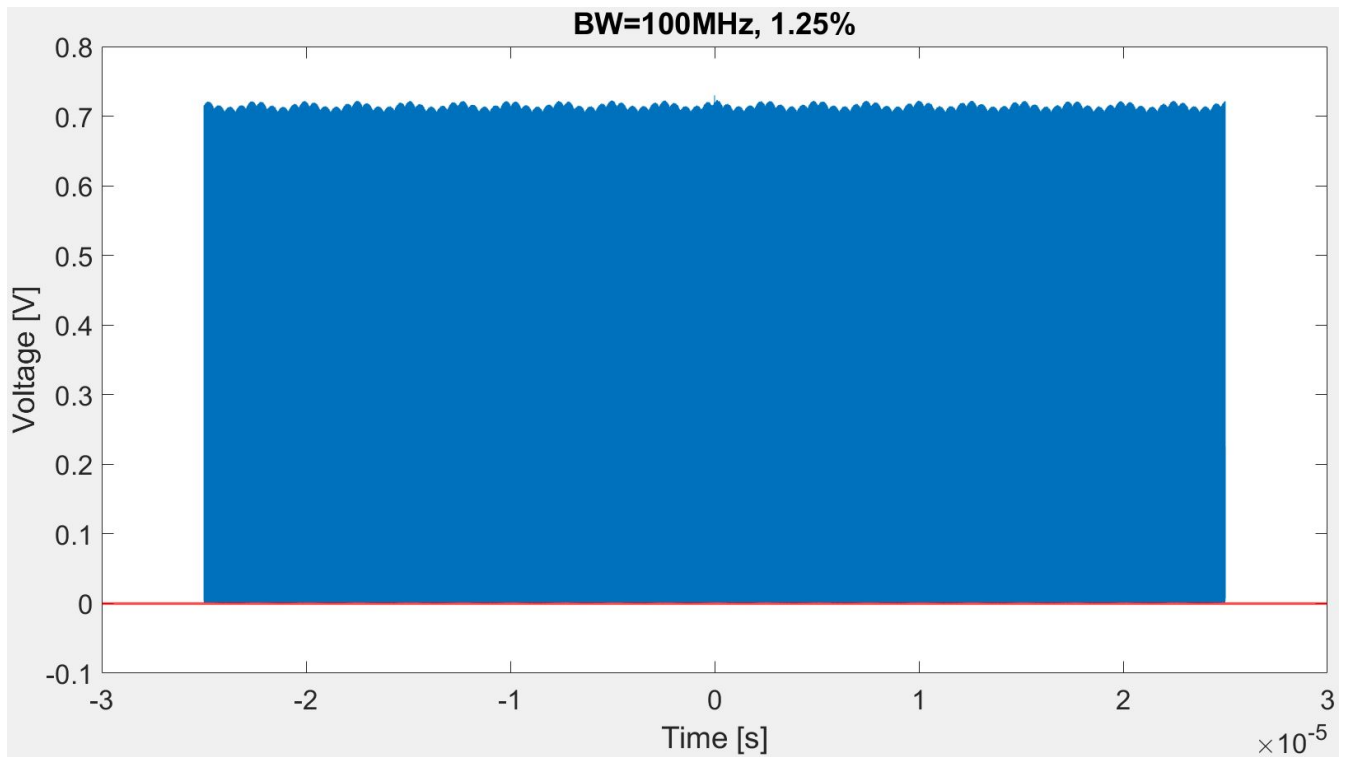


Figure 3.10: Oscilloscope track in the case of 100 MHz BW and 1.25% ratio

modulation peaks was considered. This was performed in order to cut away the additional modulations. The same procedure was performed for the minimum even though they were more stable. The peak-to-peak was the difference between those two values. Another possibility to retrieve the modulation shape was to consider, instead of the peak, the area of each pulse. The idea was that, due to the discrete sampling of the oscilloscope, the exact peak was not always captured. By considering the area under the curve rather than relying on a single data point, this issue could be mitigated. Anyway in this second case a normalization factor should be additionally considered. For this reason and for more interpretability we choose to use the peaks method.

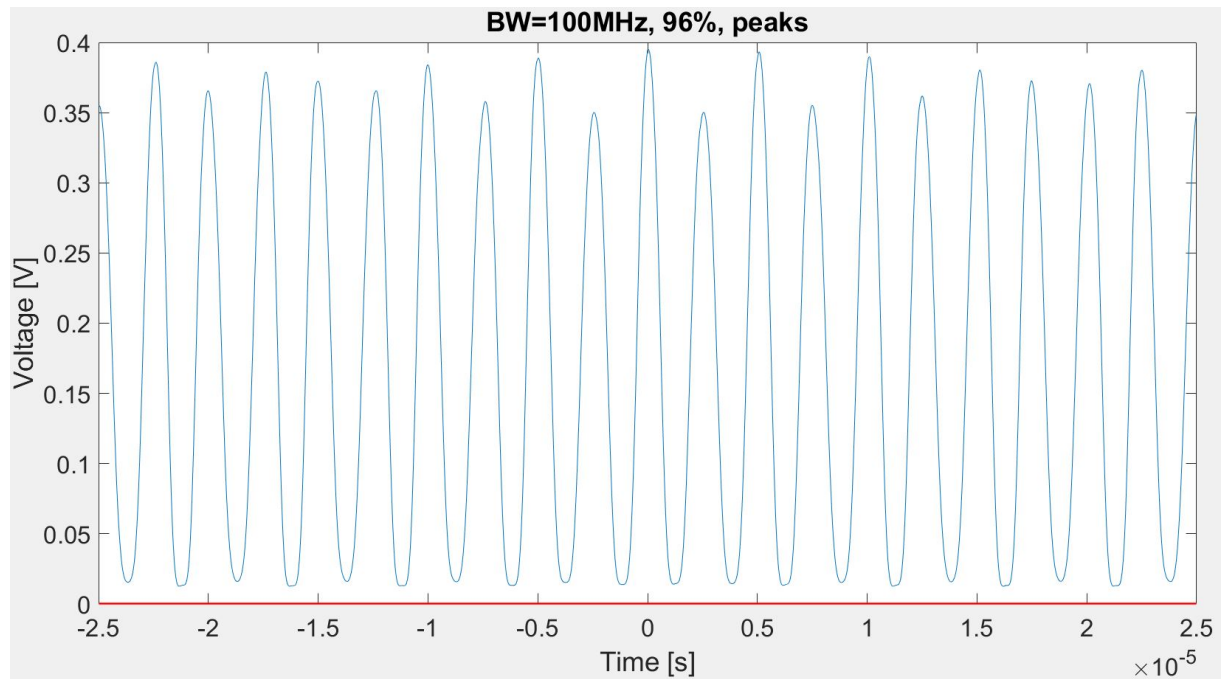


Figure 3.11: Modulation shape of the 100 MHz BW at 97% retrieved with peaks method

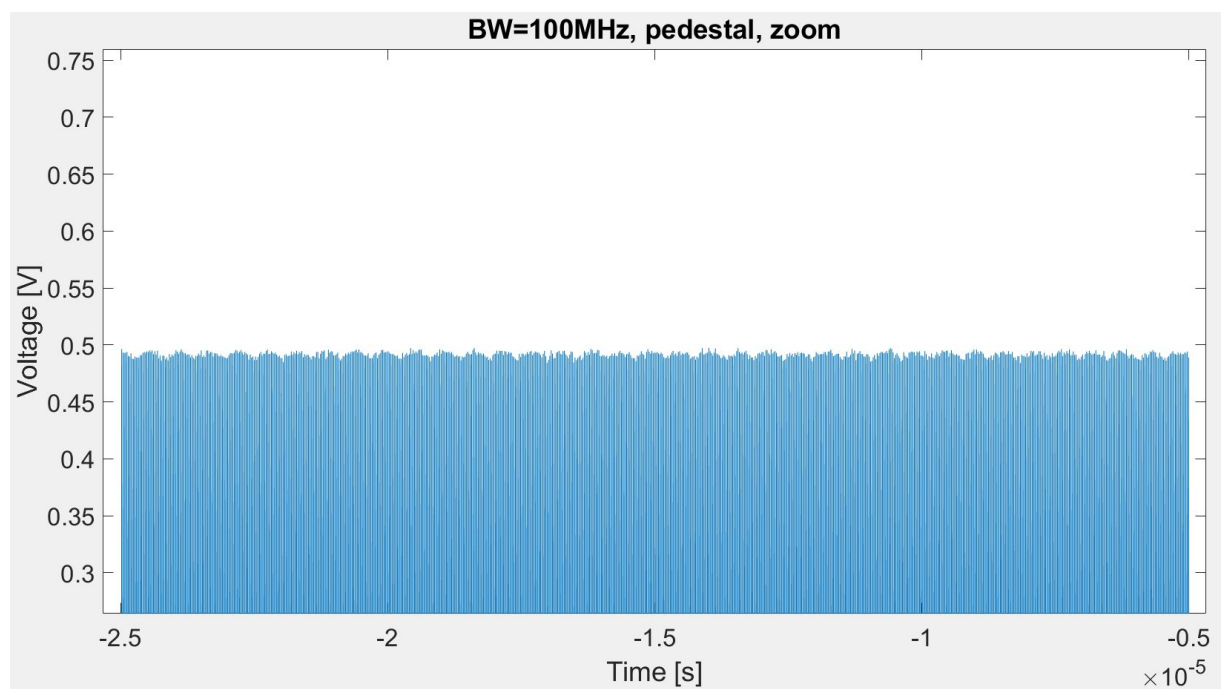


Figure 3.12: Image of just the pedestal where we can observe an intrinsic modulation coming from the laser

## 2) BW = 14 MHz

At this point what it was done is repeat the previous measurement changing the photodiode bandwidth to 14 MHz. The beams were attenuated more since the photodiode has an higher gain for a smaller BW.

Ratio	Lock-in measure	Oscilloscope measure	FF
95%	40.4 mV	154 mV	3.81
Ratio	Lock-in measure	Calculated value	Oscilloscope measure
52%	115.9 mV	441.8 mV	443.7 mV
32%	57 mV	217.2 mV	216.3 mV
1.23%	2.54 mV	9.68 mV	8.9 mV

Table 3.2: Data for the 14 MHz photodiode bandwidth

## 3) BW = 1.8 MHz

Ratio	Lock-in measure	Oscilloscope measure	FF
97%	60.31 mV	166.2 mV	2.75
Ratio	Lock-in measure	Calculated value	Oscilloscope measure
59%	88.55 mV	244 mV	242.6 mV
22%	59.07 mV	162.8 mV	163.8 mV
0.53%	2.26 mV	6.22 mV	5.3 mV

Table 3.3: Data for the 1.8 MHz photodiode bandwidth

In the following images it is important to pay attention to the voltage scale. In fact the images seems equals just because this is the case that simulate the *filled* sinusoid, but in every picture are varying both the modulated amplitude and the pedestal.

## 3.5. Data analysis

The first thing we can observe from the data, is that the calculated values closely align with the oscilloscope measurements as expected. Even though ideally the two values should remain the same, a slight error becomes more pronounced as the ratio decreases. The main source of this discrepancy is the oscilloscope's measurement accuracy. As the ratio

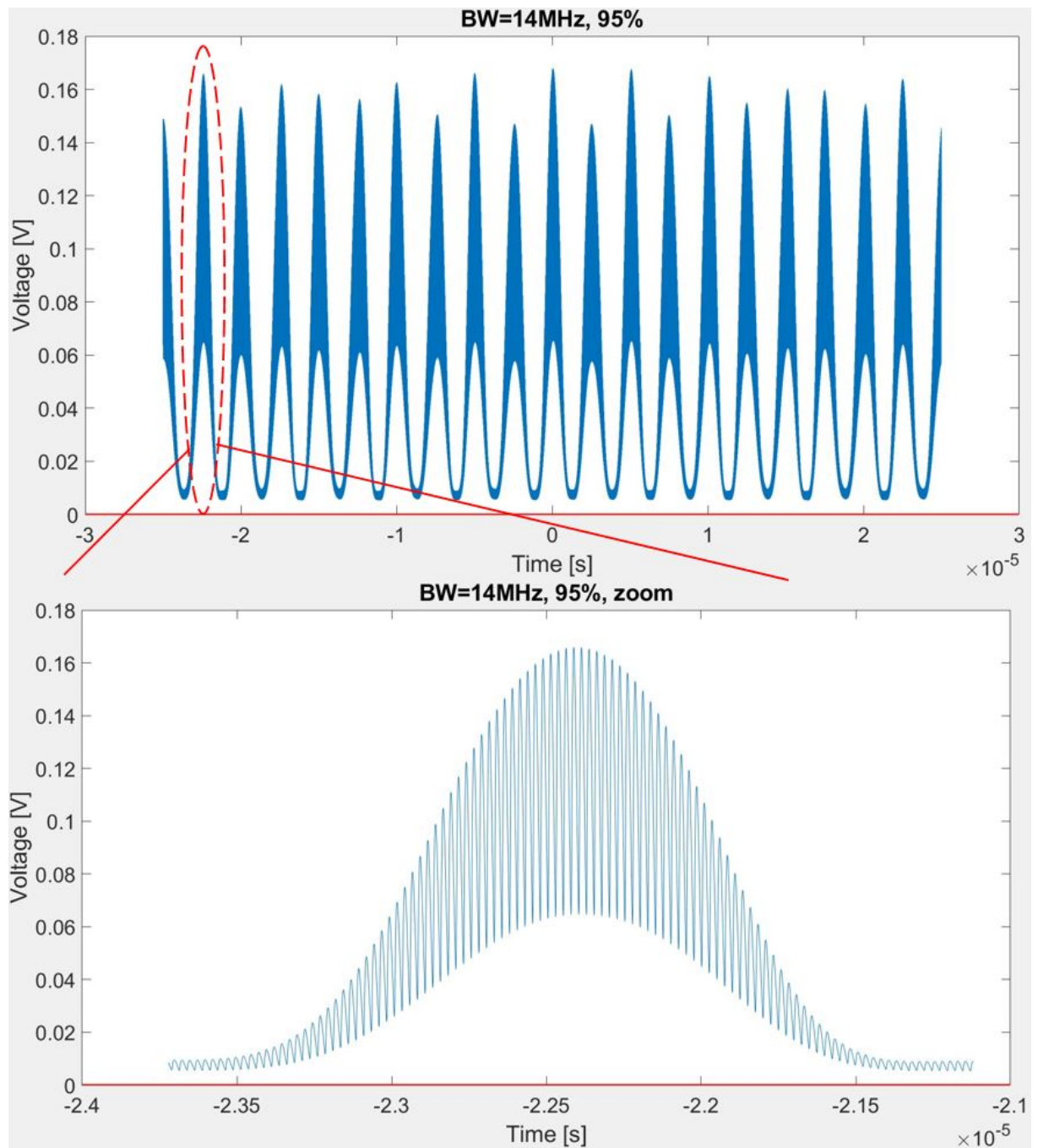


Figure 3.13: Oscilloscope track in the case of 100 MHz BW and 97% ratio

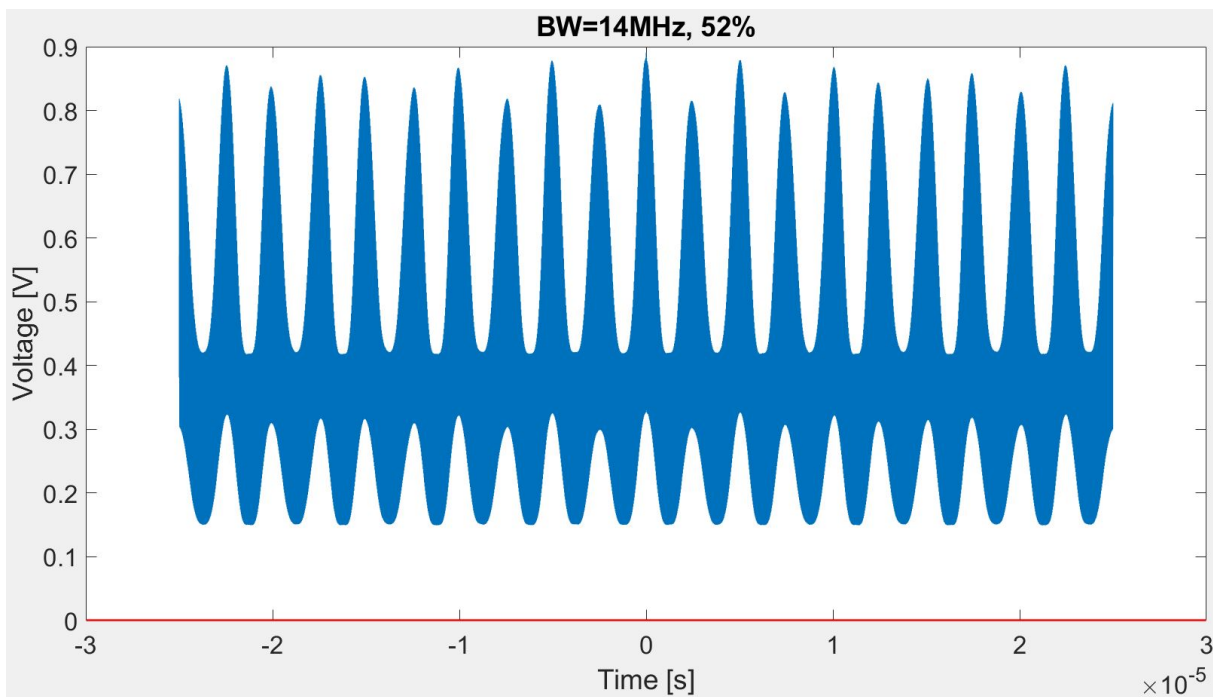


Figure 3.14: Oscilloscope track in the case of 100 MHz BW and 72% ratio

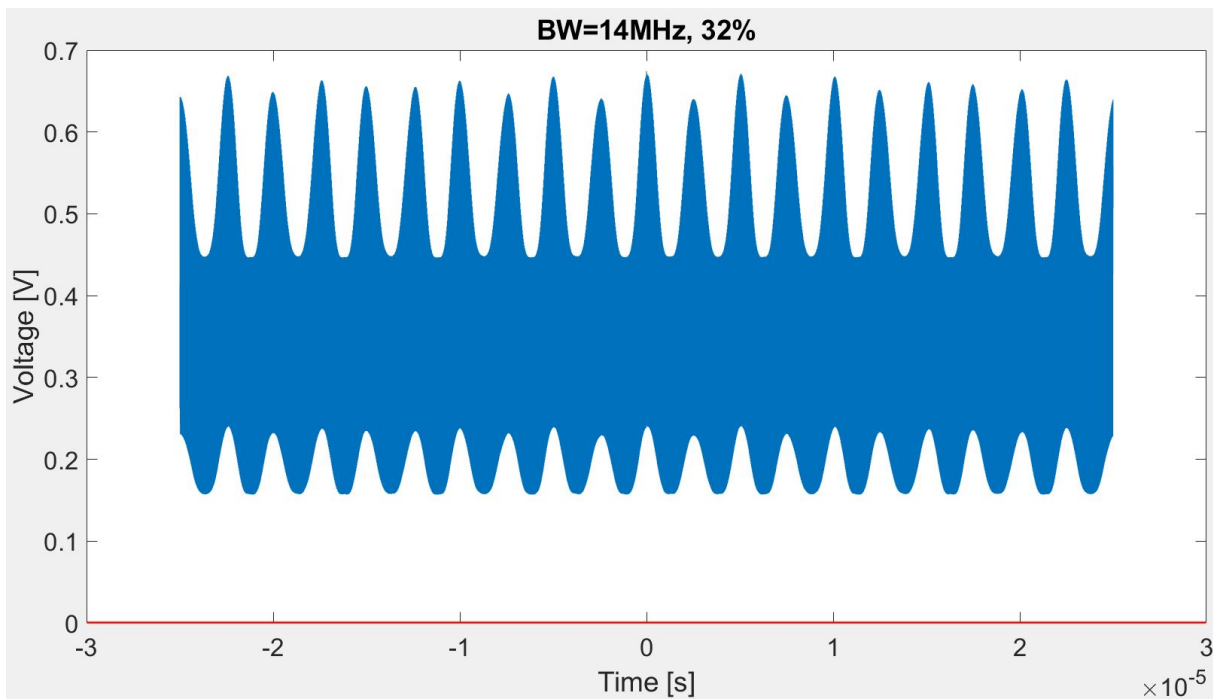


Figure 3.15: Oscilloscope track in the case of 100 MHz BW and 46% ratio

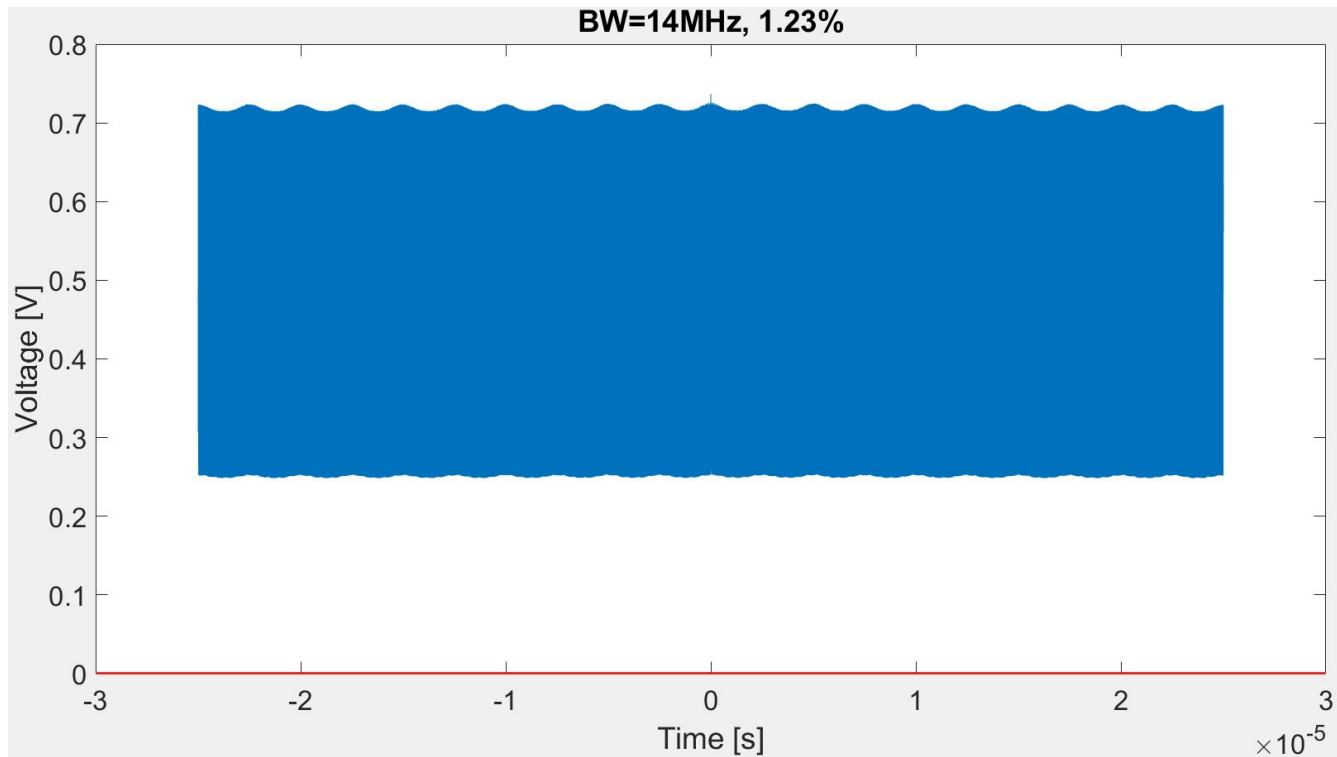


Figure 3.16: Oscilloscope track in the case of 100 MHz BW and 1.25% ratio

decreases, accurately acquiring the modulated amplitude becomes increasingly difficult and ambiguous. This reduction in the ratio can occur for two reasons: either the pedestal height increases, or the modulated amplitude decreases. In the first scenario, an increase in the pedestal height requires a larger voltage range on the oscilloscope, which decreases its resolution for detecting the smaller modulated amplitude since fewer bits are now assigned to the same signal range. In the second scenario, if the pedestal remains constant but the modulated amplitude decreases, the oscilloscope's relative bit error increases, resulting in reduced resolution because the same number of bits are now applied to a smaller signal. The idea is therefore to acquire the FF factor in a situation where the modulation amplitude can be well extracted from the oscilloscope, and then consider as truth the lock-in measure times the FF when instead the oscilloscope can not be employed. This naturally acquire even more importance when we take into account the true case of a SRS experiment where the modulated amplitude (the SRS signal) is 3-4 order of magnitude smaller than the pedestal.

The second thing we can notice is the fact that for the small BW case the filling factor value is almost just the constant term  $2\sqrt{2}$  that we discussed before. A question that might come to mind is if the FF in this case is useless, and if one could use always a small photodiode bandwidth to avoid all the question. The answer is no, and to enter

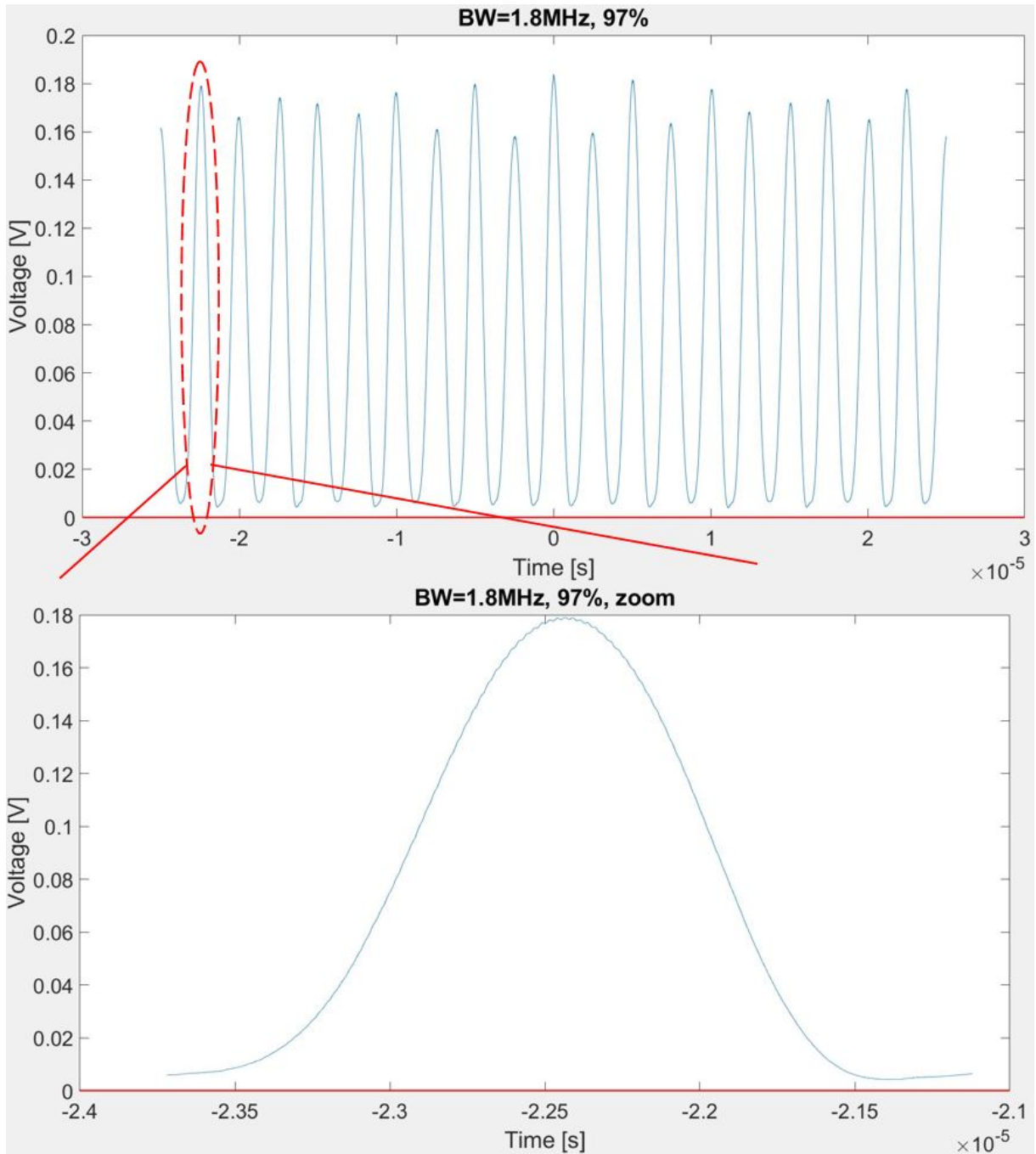


Figure 3.17: Oscilloscope track in the case of 100 MHz BW and 97% ratio

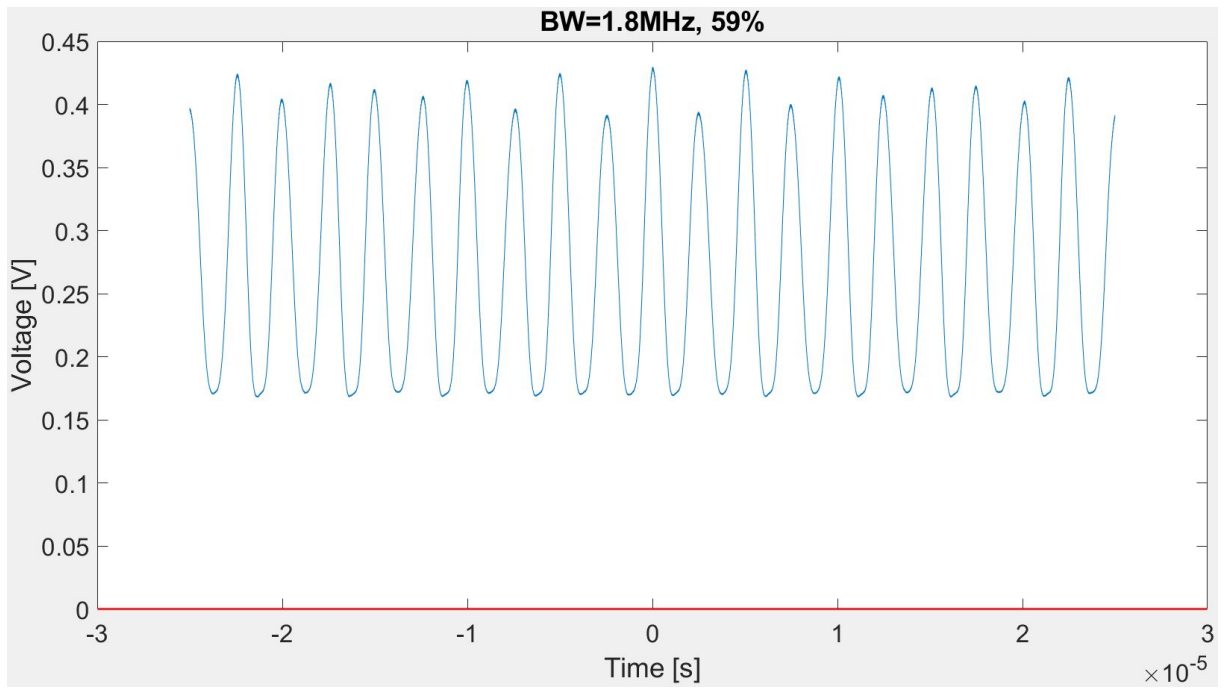


Figure 3.18: Oscilloscope track in the case of 100 MHz BW and 72% ratio

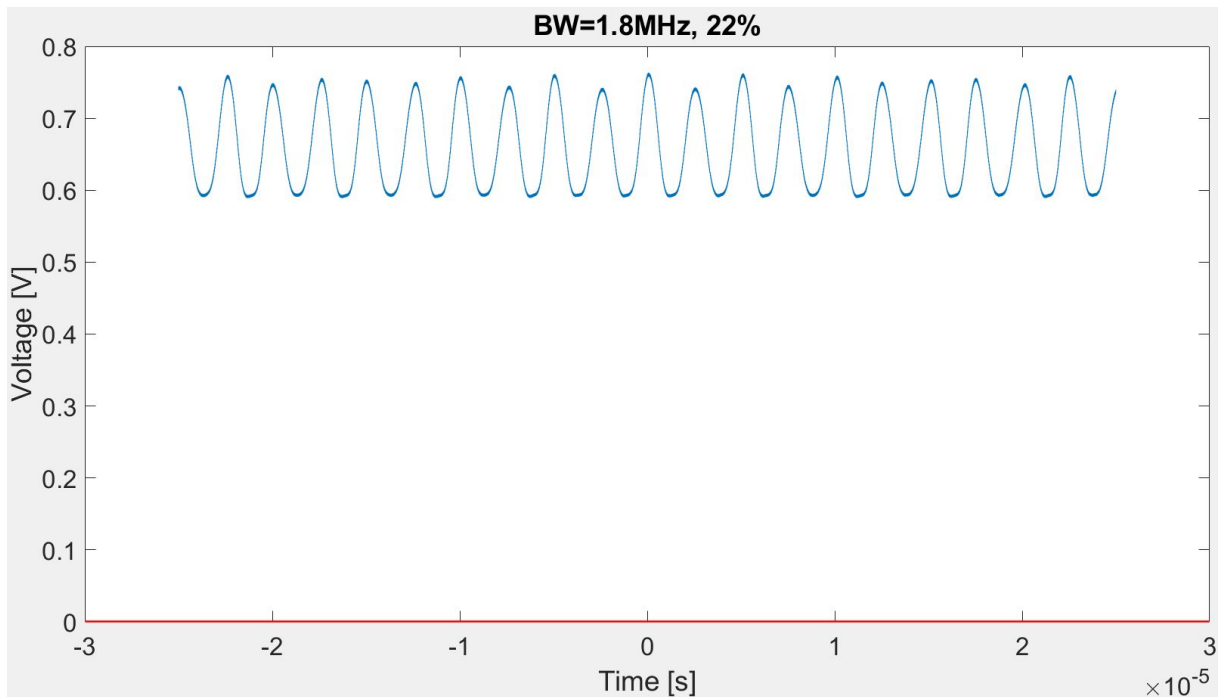


Figure 3.19: Oscilloscope track in the case of 100 MHz BW and 46% ratio

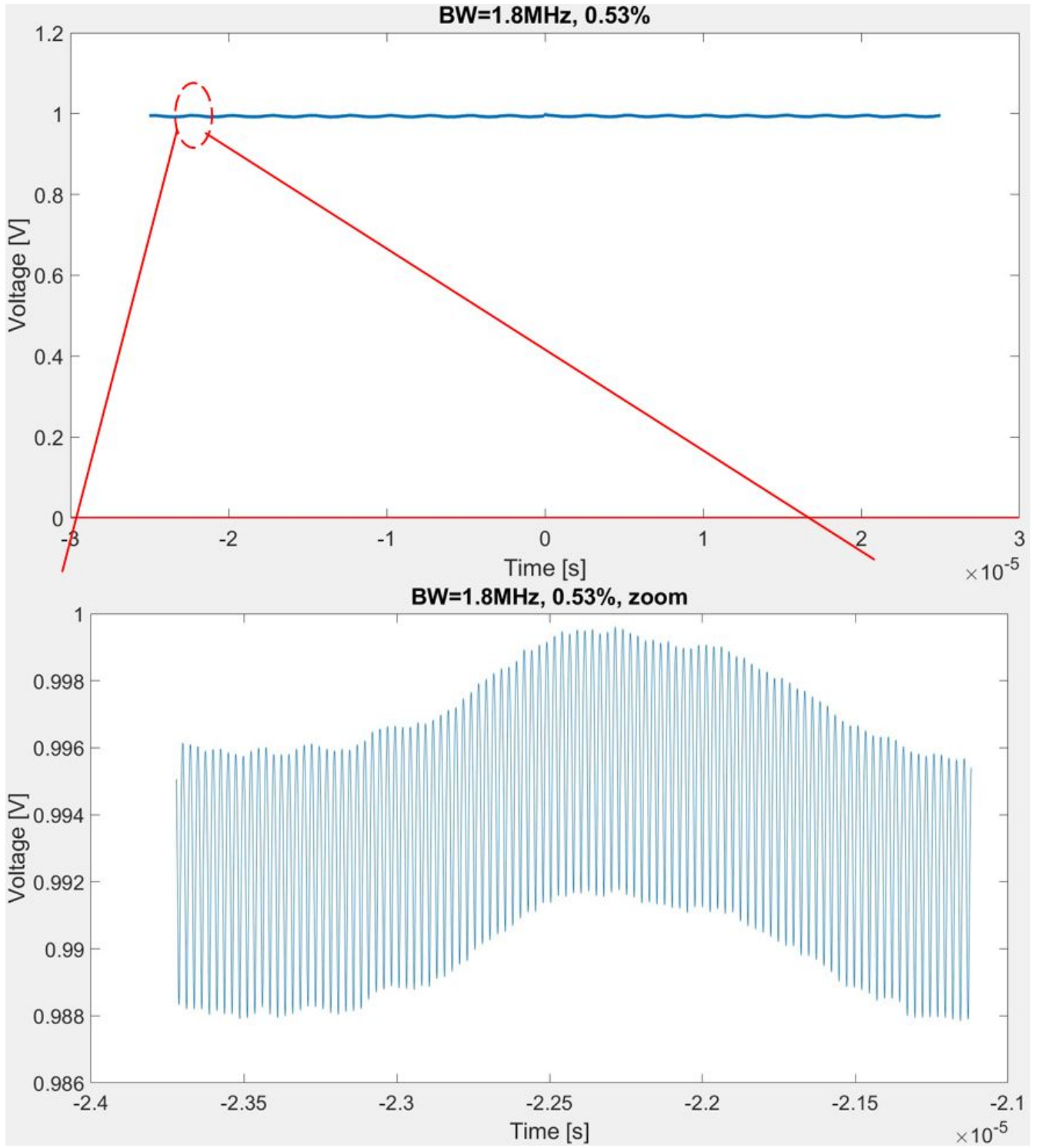


Figure 3.20: Oscilloscope track in the case of 100 MHz BW and 1.25% ratio

into details there are different reasons. As stated different times the main aim of this work is to proceed toward a quantitative and set-up independent SRS, this also implies to achieve any precision possible. The simplest reason is the fact that someone could not be aware of this  $2\sqrt{2}$  factor or maybe forgot it. The Filling Factor does not allow this option since it is intrinsically included in it. Then there is the fact that even if the FF is similar, it does not perfectly match the  $2\sqrt{2}$  factor. This is not just due to noise but there are two different sources. The first source is the fact that even if the photodiode bandwidth is much smaller than the laser repetition rate, it is almost impossible to completely delete the pulsed nature of the beam. In fig Fig. 3.20 is showed a zoom where we can clearly see this phenomenon. In the first picture, what is left of the pulsed nature is really small in comparison to the modulation amplitude. Instead, in the last one those pulses are almost comparable to the modulation amplitude. The second source is the fact that is difficult that the modulator is able to modulate with a perfect sinusoid. This is also the reason why the FF is **smaller** than  $2\sqrt{2}$ . At first sight this could seem strange since one could expect the FF to be always bigger considering its *filling* nature. In reality this is not so strange and it is not a measure error. To understand the concept we now consider the case of a square modulation. Assume that the modulation signal is a square wave at frequency  $\omega$  with peak-to-peak amplitude  $2A$ . From Fourier theory[3], its frequency component at  $\omega$  is  $\frac{4A}{\pi}$ . This means that our lock-in, demodulating at  $\omega$ , would return  $\frac{4A}{\sqrt{2}\pi}$ . In this case the FF would be  $2\sqrt{2} \cdot \frac{\pi}{4}$  that is smaller than  $2\sqrt{2}$ . This is a case where this 'contradictory' smaller FF factor is clearly explained. In our real case the modulation is not a square wave but neither a perfect sinusoid, and this is the reason behind the small difference of FF from  $2\sqrt{2}$ .

There is another point to consider that could add even more importance to the question for practical reason. As we saw the FF factor, even though it cannot be avoided, finds its minimum relevance in the case of low bandwidth, since its value, except for the  $2\sqrt{2}$  factor is close to one. Instead FF reach its maximum, and so its maximum of importance in the first case. From math[5, 18] it comes out that using a modulation sinusoid with frequency equal to half of the repetition rate, increase the signal-to-noise ratio (SNR) by  $3dB$ . In this case is literally impossible to have a photodiode bandwidth that is some factor smaller than the RR, but bigger than the modulation frequency. In this configuration therefore the first case, big photodiode bandwidth, is principally the one implied, and so the FF finds the best relevance.

The final point I want to consider is another practical consideration. For this experiment we used a separate oscilloscope to be more precise, since in terms of bandwidth and sampling rate (1 GHz and 2.5 Gsample/s respectively) is better than our lock-in (50 GHz

and 210Gsample/s). Of course one could use directly the scope function of the lock-in to perform the FF measure. Anyway there is a detail to consider. In the case of  $BW = 100$  GHz the signal seen from the oscilloscope and from the lock-in scope are different. This happens because in the first case the oscilloscope considering its big BW does not influence the signal, instead the lock-in, with a smaller BW, changes the signal. The pulse shape and height are different. Acquiring the modulated amplitude from the two would give different values, and considering that the lock-in demodulation measure is the same, we would find two different filling factor. This does not mean that one is correct and the other is wrong. They are both correct. The key point is to remain coherent and use always the same instrument for the entire SRS measure. This means that if the FF is acquired from the lock-in scope, this must be used also to measure the pedestal  $I$  in order to retrieve the correct  $\Delta I/I$ .

# 4 | SRS cross-section

## 4.1. Experimental set-up for $\sigma_{SRS}$ measurement

As we can see from equation (2.65), in order to measure the absolute  $\sigma_{SRS}$  it is previously required to measure the more standard  $\Delta I/I$  ratio. This was our starting point and in this first section we will present the set-up employed for the SRS measurement. The principal component are:

- Picus Duo Laser
- Half wave plate
- Polarized Beam splitter
- Illumination(L1) and collection(L2) lenses
- FELH-1000
- Photodiode
- Lock-in amplifier

### Laser

The employed laser was the Picus Duo from Refined Laser System, a commercial laser specifically designed for CRS application. The laser is capable to emit two laser beams, pump and Stokes, with exciting wavelength  $\Omega$  tunable within a large range of wavenumbers, from 700 to 3100 $cm^{-1}$ . Pump and Stokes are respectively tunable from 770 – 980 $nm$  and 1022 – 1053 $nm$ . The pulse repetition rate is 40.5 $MHz$ . One of its best feature is the possibility to set, directly from its dedicated software (Fig. 4.2), a relative delay between the two beams, allowing to achieve temporal overlap despite the fact that they have different optical paths. Picus Duo also has an internal modulator that allows to modulate just the pump beam choosing between a modulation frequency of 20.25 $MHz$  (half of the repetition rate), 10 $MHz$  and 6 $MHz$ . We decided to use the  $RR/2$  modulation to achieve

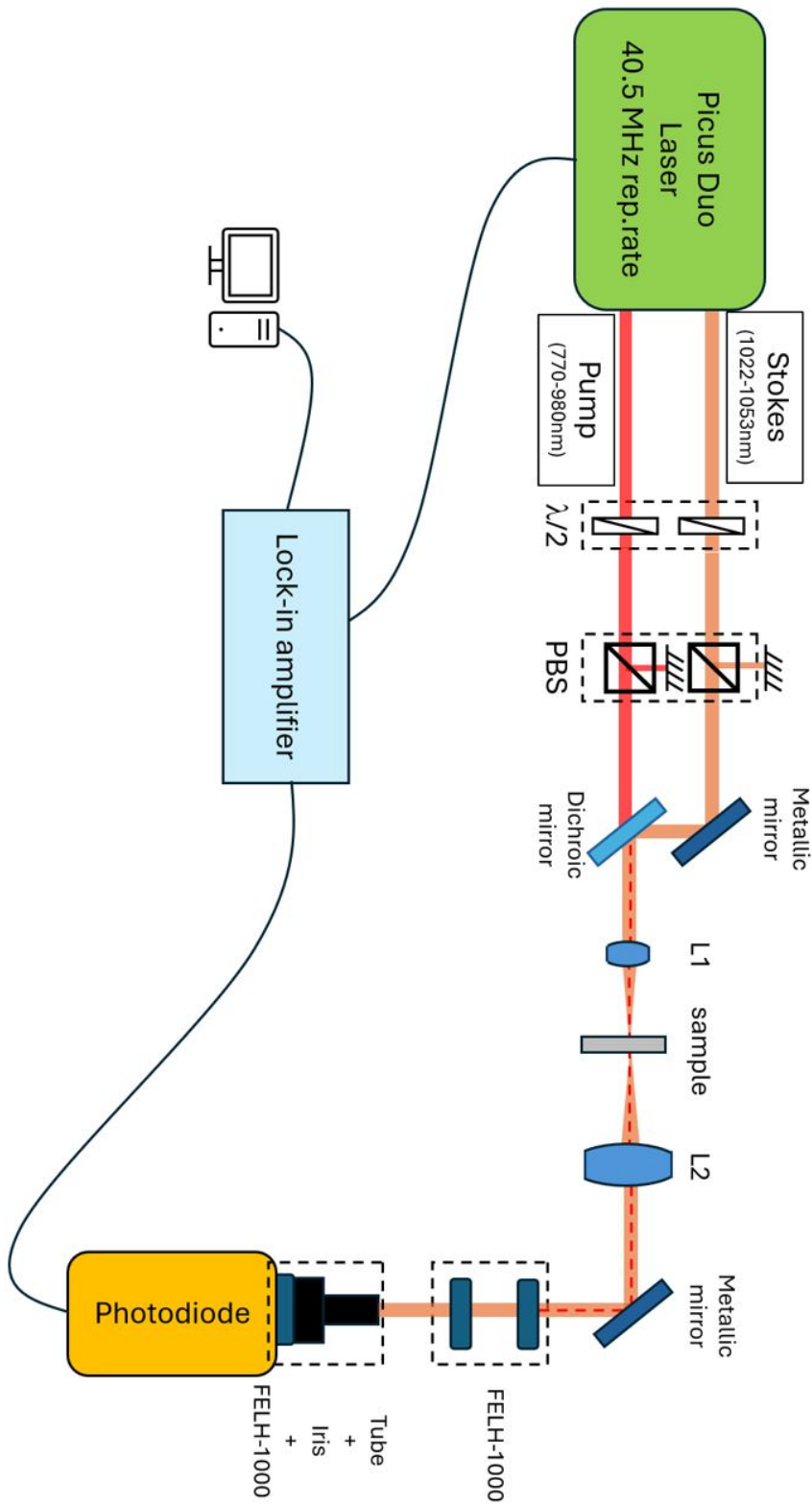


Figure 4.1: Set-up implied for the SRS measurements.  $\lambda/2$  = half wave plate, PBS = Polarized Beam Splitter, FELH-1000 = High performance long-pass filter from 1000 nm, L = lens.

a better SNR ratio[5, 18]. Since just the pump can be modulated, the performed SRS experiment was the SRG.

### Power control

The next part is the combination of a half wave plate  $\lambda/2$  followed by a polarized beam splitter (PBS). Their function is to control the power arriving to the sample. In particular the  $\lambda/2$  rotate the polarization direction of the field while the PBS transmits the vertical polarization and reflects the horizontal one. In this way, by manually rotating the polarization with the  $\lambda/2$ , we could control the vertical component in the polarization and so the fraction of power transmitted. The reflected components were discarded.

### Beam combiner

There is then a dichroic mirror, an optical component capable of transmitting certain wavelength and reflect others. Its function was basically to recombine the two beams.

### Sample

We have then the illumination lens (L1) to focus the light into the sample and a collection lens (L2) to collect the light. L1 is the *AC080-016-B-ML* from Thorlabs. It is a small (8mm diameters), B coated (transmission in the 650–1050nm range), achromatic doublet with a focal length of 16mm. The achromatic doublet is a type of lens designed to reduce chromatic aberration, a common optical issue where light of different colors (in this case pump and Stokes) focuses at different distances. We decided to use this type of lens and not an objective to achieve a smooth focused beam, but at the same time to correct the most possible chromatic aberrations. For collecting light instead, we had less restrictions since we just needed to take all the light coming from the sample, and almost focus it on the photodiode. L2 is a simple plane-convex lens with 3.5cm focus, always B-coated.

The sample was contained in a 1mm cuvette.

### Pump cutting

Since we are performing an SRG experiment, the beam we want to detect is just the Stokes. The pump is the one modulated, so also a minimum component entering the photodiode, can be detected and well demodulated by the lock-in leading to an overestimation of  $\Delta I$ . For this reason is important to **completely** cut away the pump. We used three long-pass filter at 1000nm to remove the majority of the pump. Since the pump wavelength

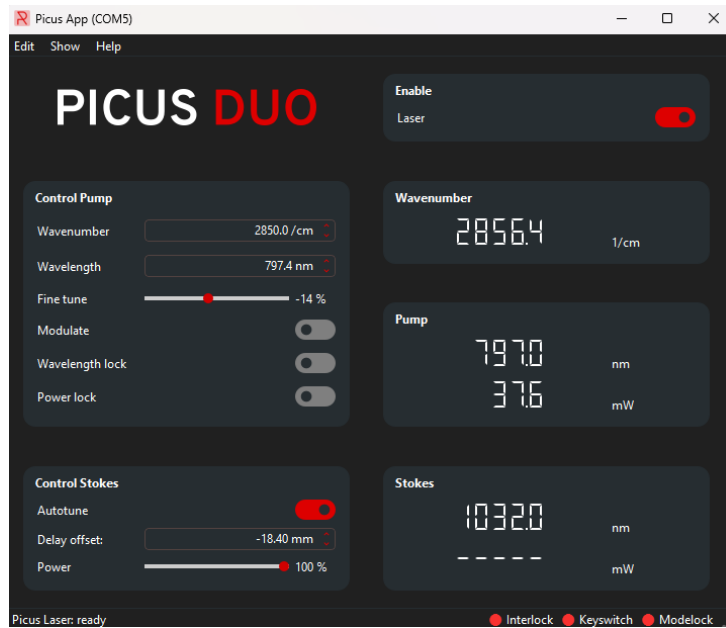


Figure 4.2: Picus software used to control the various parameters like wavenumber and delay

was slightly below  $1000\text{nm}$  and the Stokes instead slightly above, we needed to use high quality filters (FELH-1000) with a sharp wavelength response (Fig. 4.3). The third one was screwed onto the photodiode in order to cut away all the environmental scattering of the pump. Even in this configuration some pump was able to enter the photodiode from the environment. The solution was to screw on a tube and an iris to reduce the possible angle of arriving at the minimum.

### Photodiode

The photodiode employed was once again the OE-300-SI-30 used in the previous chapter. For this experiment the photodiode bandwidth was set to  $60\text{MHz}$  since it was sufficient to acquire both the pulses and the modulation.

### Lock-in amplifier

Also in this case the lock-in was the one used in the previous chapter, the HF2LI-50. For this experiment we did not use an external oscilloscope but we calculated the FF and acquired the  $I$  value, directly from the lock-in scope.

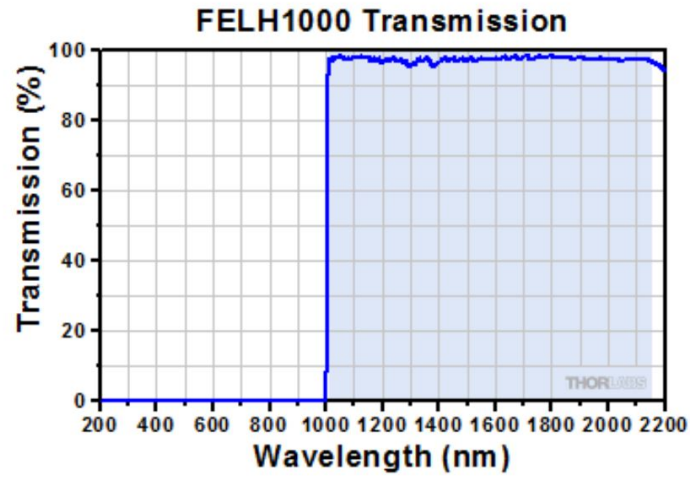


Figure 4.3: FELH-1000 transmission in function of the wavelength. The blue shaded region in the graph represents the transmission region of the filter, 1013 – 2150nm. Image acquired from Thorlabs website.

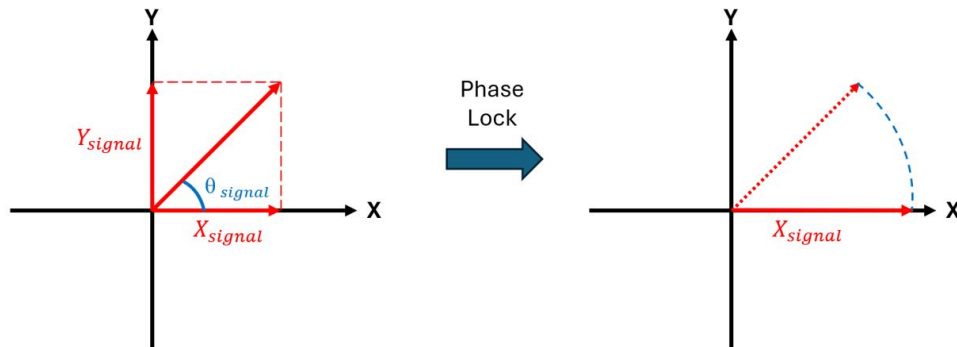


Figure 4.4: Schematic representation of the phase lock operation. The signal with random phase  $\theta$  is brought on the X axis.

## 4.2. $\Delta I/I$ measurement

Our final aim is to measure the SRS cross-section of a sample. In order to have a ground truth and be able to check the result, we decided to consider the methanol C-O vibrational mode used as reference also in the Gao and Min papers [9, 17]. The peak of this bond is in the fingerprint region, in particular at  $1033\text{cm}^{-1}$  [15]. For this wavelength the Picus sets the pump at  $\lambda_{\text{pump}} = 949.3\text{nm}$  and  $\lambda_{\text{Stokes}} = 1052.7\text{nm}$ . We optimized the system for those wavelengths. As preliminary operation we wanted to find the correct time delay to set between the two. In order to do that we placed a BBO crystal in the sample position and modified the delay up to when we observed the Sum Frequency Generation. In this way we found the right delay to achieve temporal overlap, and we also checked the spatial overlap. At this point we started to work with the sample. As we said in Chapter 3 ((3.2)) the lock-in amplifier operation captures two signals, X and Y, to accurately retrieve the amplitude information. This dual-signal approach is necessary because the demodulation signal may be phase-shifted relatively to the modulation signal. However, using two signals can introduce more noise compared to single-signal measurements. A common technique to reduce noise is to match the phase between modulation and demodulation, so that the entire signal aligns with the X component, while Y remains at zero. In an SRG experiment, the modulating signal is the pump, which transfers both the modulation and the **same** phase to the Stokes signal. In practice, the pump is sent to the lock-in to *lock the phase*, operation that is simply performed by the lock-in itself. This phase is then used to demodulate the Stokes signal, allowing for the capture of only the X component (Fig. 4.4). Naturally when the pump was sent onto the photodiode we removed the FELH-1000. At this stage, we also conducted the FF measurement using the pump beam. Ideally, since we are demodulating the Stokes signal, the FF should be evaluated for that beam. However, as discussed in the previous chapter, the precise FF measurement requires a fully modulated signal. Since the Picus system only allows modulation of the pump, evaluating the FF directly from the Stokes beam is not possible. Fortunately, because both the pump and Stokes are picoseconds pulses, they appear as equivalent to the photodiode, even if their temporal shapes is slightly different. Thus, the photodiode response remains consistent for both beams, ensuring that the FF is effectively the same for both. In this configuration the scope measure returned  $M_{sc} = 568\text{mV}$  and while the demodulation value was  $M_{dem} = 123\text{mV}$ . So the Filling Factor we used for the experiment was  $FF = M_{sc}/M_{dem} = 4.62$ . At this point we placed back the filters and started looking at the signal. Operationally we firstly send just the Stokes and note the X value, then we add the pump monitoring the X increase  $\Delta X$ . This increase is the SRG signal. The initial value of X was not zero, from our observation it was probably due to the coupling

of electromagnetic waves emitted from the modulator, with the BCN cables. Anyway this led to just a simple off-set. Before acquiring the data we performed a fine tuning of the delay and of the sample positioning, maximizing the  $\Delta X$  observed. The sample position tuning was performed thanks to a manual translator where the sample was placed on. We also optimized the power employed thanks to the  $\lambda/2$  and PBS system. Since the  $(\frac{\Delta I}{I})_{SRS}$  is proportional just to the pump intensity, we decided to maximize the pump power while keeping a low the Stokes power. The Stokes power minimization allows to achieve the same  $\Delta I/I$  value, but at the same time reduce all the other non-linear effect that could take place. Those background signals are for example cross-phase modulation (XPM), two-photon absorption (TPA) and thermal lensing (TL), that at the end reduce the contrast in SRS microscopy[1]. The power employed were  $P_{pump} = 56.9mW$  and  $P_{Stokes} = 542\mu W$ . To be the most precise possible we set the time constant of the LPF to  $1s$ . In this configuration we measured a  $\Delta X$  of  $2.05\mu V$  where the standard deviation on the single X measurements were around  $15nV$ . The Stokes intensity, acquired from the lock-in scope was  $I_0 = 83.5mV$ . This leads to a final results of  $\Delta I/I = \Delta X \cdot FF/I_0 = 1.13 \cdot 10^{-4}$ .

We also did a full spectrum measurement of the calibrated  $\Delta I/I$  for the methanol (Fig. 4.5). In Fig. 4.6 it is shown the emitted pump power in function of the wavenumber, automatically setted by the laser. What we want to highlight is that the spectrum alone has no meaning. Since the  $\Delta I/I$  is proportional to the pump power, the proportions between different peaks in the spectrum are wrong and the spectrum does not really represent the shape of the material Raman response. Instead a  $\sigma_{SRS}$  spectrum would represent correctly the spectrum shape and additionally it would do it in a quantitative way.

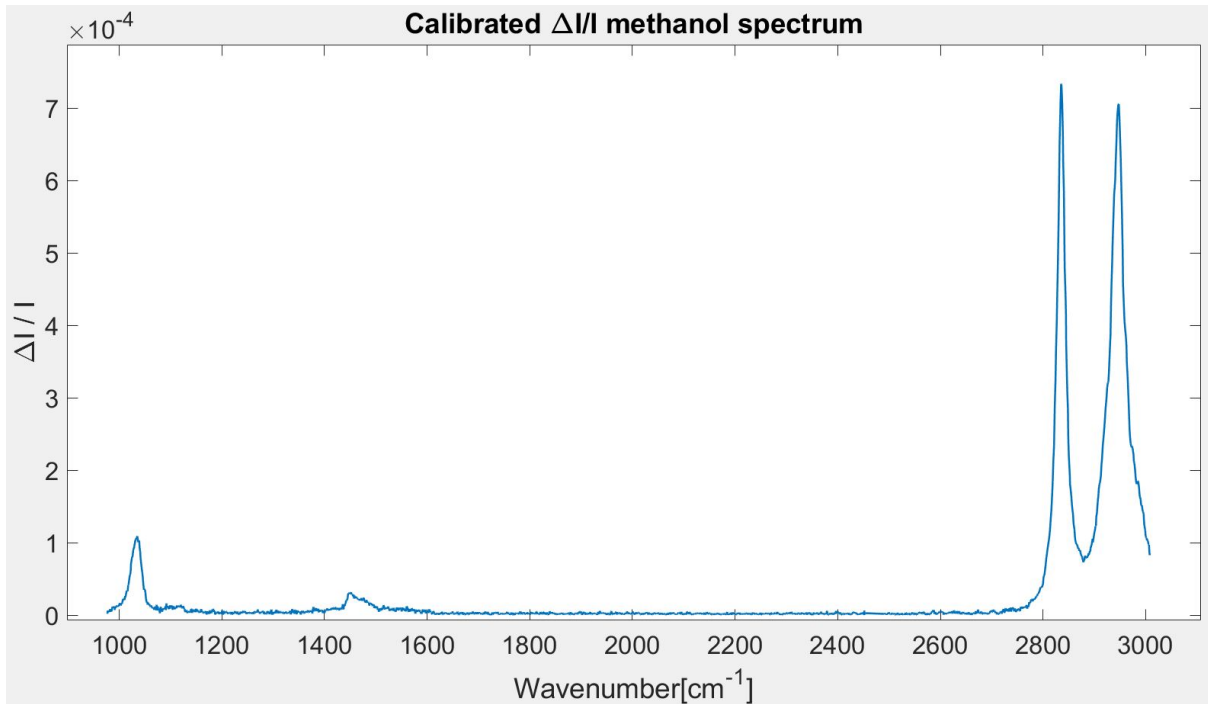
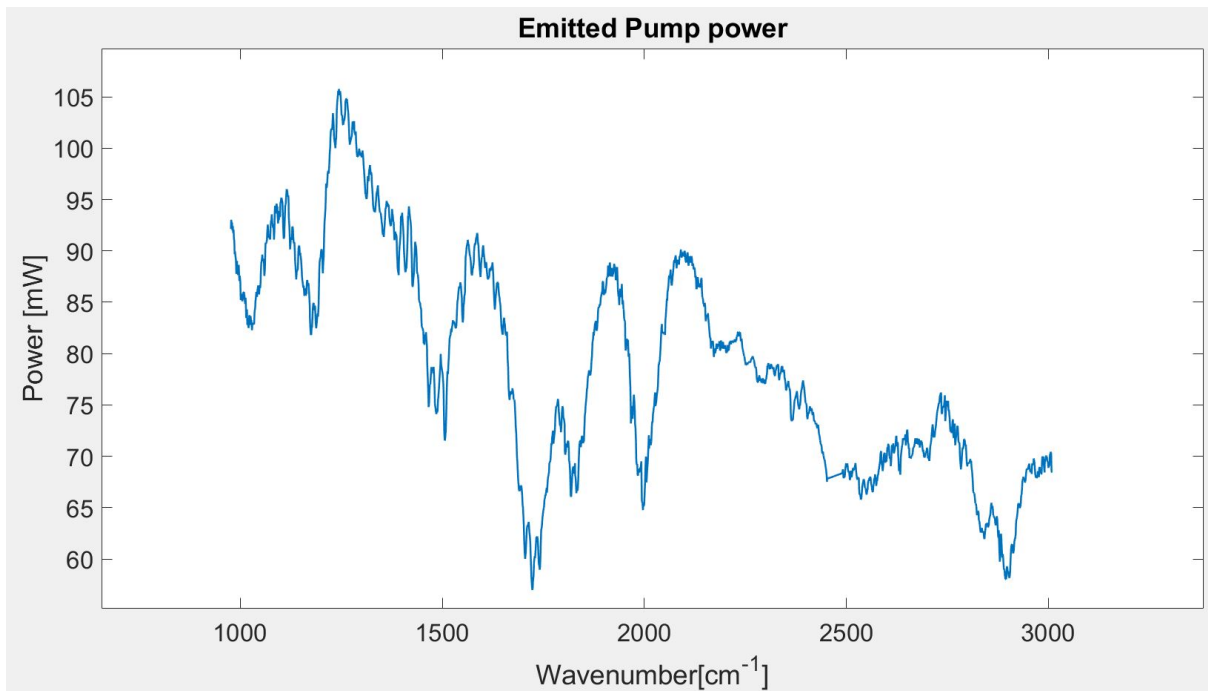
Figure 4.5: Calibrated  $\Delta I/I$  spectrum of methanol

Figure 4.6: Emitted pump power in function of the wavenumber

### 4.3. SRS cross-section

We enter now in the most important part of the work, the  $\sigma_{SRS}$  measure. Before starting in necessary to explain the method, and the reason behind them, that was used. As said many time along this thesis our aim was to achieve quantitative SRS. The introduction of this new parameter  $\sigma_{SRS}$  is for sure a big step toward this aim. We finally have a parameter that can really represent the SRS response of a certain material, that reflects its third order nature and owns its unit of measure. Anyway, as always, the measure procedure perturb the result itself leading to value that it is not just material dependent but also set-up dependent. Our aim is to perform a SRS cross-section calibration, that is completely, or at least up to our possibilities, set-up independent.

We now take into account the equation (2.62). As we said what one typically do is to cancel out the  $\Phi_s$  leading to the equation

$$\left(\frac{\Delta I}{I}\right)_{SRG} = \frac{[c] \cdot N_a \cdot V \cdot \sigma_{SRS}(\Omega) \cdot \Phi_p}{A} = \sigma_{SRS}(\Omega) \cdot K \quad (4.1)$$

where K is a term that encloses the set-up parameters, introduced just for understanding the next step.

Imagine to perform a  $\sigma_{SRS}$  measure achieving a certain value for it. Now imagine to have a slightly different shape for Stokes beam, keeping all the rest unchanged. Since the spatial overlap is changed also the  $(\frac{\Delta I}{I})_{SRG}$  will slightly vary. The factor K instead would be unchanged. This would lead to a different value of  $\sigma_{SRS}$  even if it should be an univocal material property. This oversimplified example shows how equation (4.1) is not sufficient and that it could be improved. We decided to consider three key element that should be taken into account in order to achieve a more set-up independent value. Those three elements are:

- 1) Spatial distribution
- 2) Temporal distribution
- 3) Spectral distribution

What is done up to now is to avoid considering those three element in details but a simplified version of them. In particular for the spatial component, using the intensity value, it is just considered an average/uniform value of the power within the whole focal volume of one beam [25]. In this way all the x, y and z distribution are avoided , but also the overlap between the two. Regarding the temporal distribution instead what is

implicitly done is to assume a simple square temporal distribution, with temporal length equal for both. Finally regarding the spectrum, what is implicitly considered is that the two beams have a perfect delta distribution at their central wavelength. We will show now how we managed those three elements and pass from the approximated situation to a real one.

### 4.3.1. Spatial distribution

The more intuitive correction is the spatial distribution. Instead of assuming a uniform distribution for the photon flux of both beams, we consider their x,y, and z dependence,  $\Phi(x, y, z)$ . In equation (2.62), we have

$$\left(\frac{\Delta I}{I}\right)_{SRG} \propto \frac{\Phi_p \cdot \Phi_s}{\Phi_s} \quad (4.2)$$

The key point is to **not** cancel out the  $\Phi_s$ . We will instead do a step back to equation (2.61) ( $(\Delta I/I)_{SRG} = rate_{SRS}/\Phi_s A$ ). Since the  $rate_{SRS}$  is the number of photons per seconds generated via SRG, it is an additive quantity. Therefore we see it as the sum (integral) of the contribution of each point.

$$rate_{SRS} = \int_x \int_y \int_z [c] N_a \sigma_{SRS} \Phi_p(x, y, z) \Phi_s(x, y, z) dx dy dz \quad (4.3)$$

The right hand denominator ( $\Phi_s A$ ) is the the number of photons arriving from the Stokes and it can be also seen as an integral

$$\Phi_s A = \int_x \int_y \Phi_s(x, y, \bar{z}) dx dy \quad (4.4)$$

note that now we have used a generic  $\bar{z}$ , because the number of photons arriving is always the same at each z.

We now combine equation (2.61) with (4.3) and (4.4). Considering that  $[c]$  and  $\sigma_{SRS}$  are uniform, and also the fact that the denominator is z independent, we can reframe an interesting equation

$$\left(\frac{\Delta I}{I}\right)_{SRG} = [c] N_a \sigma_{SRS} \int_z \left( \frac{\int_x \int_y \Phi_p(x, y, z) \Phi_s(x, y, z) dx dy}{\int_x \int_y \Phi_s(x, y, z) dx dy} \right) dz \quad (4.5)$$

Note that now we can not cancel out the  $\Phi_s$ . It is very important to understand the logical

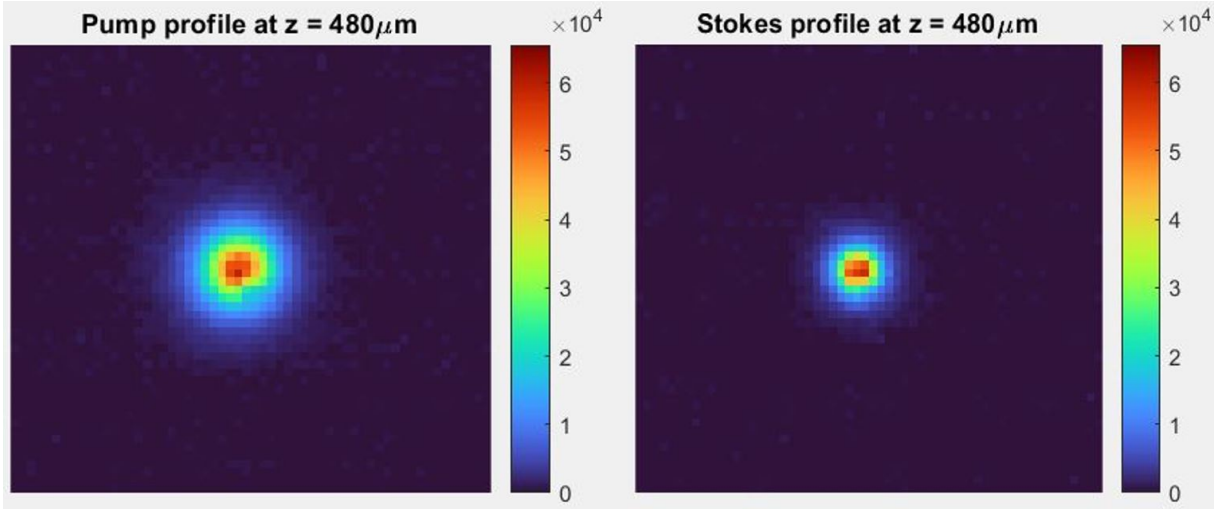


Figure 4.7: Beam profiler maps of Pump (left) and Stokes (right). Images are taken with power just below saturation. The higher value in the pixels are around 65000 ( $2^{16}$ ). Images acquired at  $480\mu m$  away from the focus.

passage performed here. In the previous case we were canceling out the  $\Phi_s$  leading to a  $(\frac{\Delta I}{I})_{SRG}$  proportional to  $\Phi_p$ . Now instead the  $(\frac{\Delta I}{I})_{SRG}$  is proportional to a **weighted average** of  $\Phi_p$ , where the weights are  $\Phi_s$ . In this way the spatial distribution and so the overlapping between the two it is completely taken into account.

Equation (4.5) was presented in this way to better get the point, but for sake of simplicity the denominator can also be written as  $P_s/h\nu_s$ .

## Practical consideration

We arrive now to the practical part of measure where it is essential to acquire the photon flux distribution. To achieve this, we chose to use a beam profiler to capture the spatial characteristics of the beam. The beam profiler, essentially a camera, provides a visual map of the beam's profile, size, shape, and intensity distribution. The beam profiler used was the LaserCam-HR from Coherent, with a pixel resolution of  $6.7\mu m$ . This is the reason why we decide to not use objective, that would gave focus of few, or even less,  $\mu m$  spot size. In practice, we positioned the beam profiler at the sample location, mounted on a manual translator. For each axial position the profiler captured an x,y map of the beam, denoted as  $S(x,y,z)$ . We scanned the full  $1mm$  range of the sample using an axial step size of  $\Delta z = 30\mu m$  facilitated by the translator.

Before proceeding, we need to interpret the map produced by the profiler and establish a link between  $S(x,y,z)$  and the photon flux  $\Phi(x,y,z)$ . Each pixel on the profiler outputs

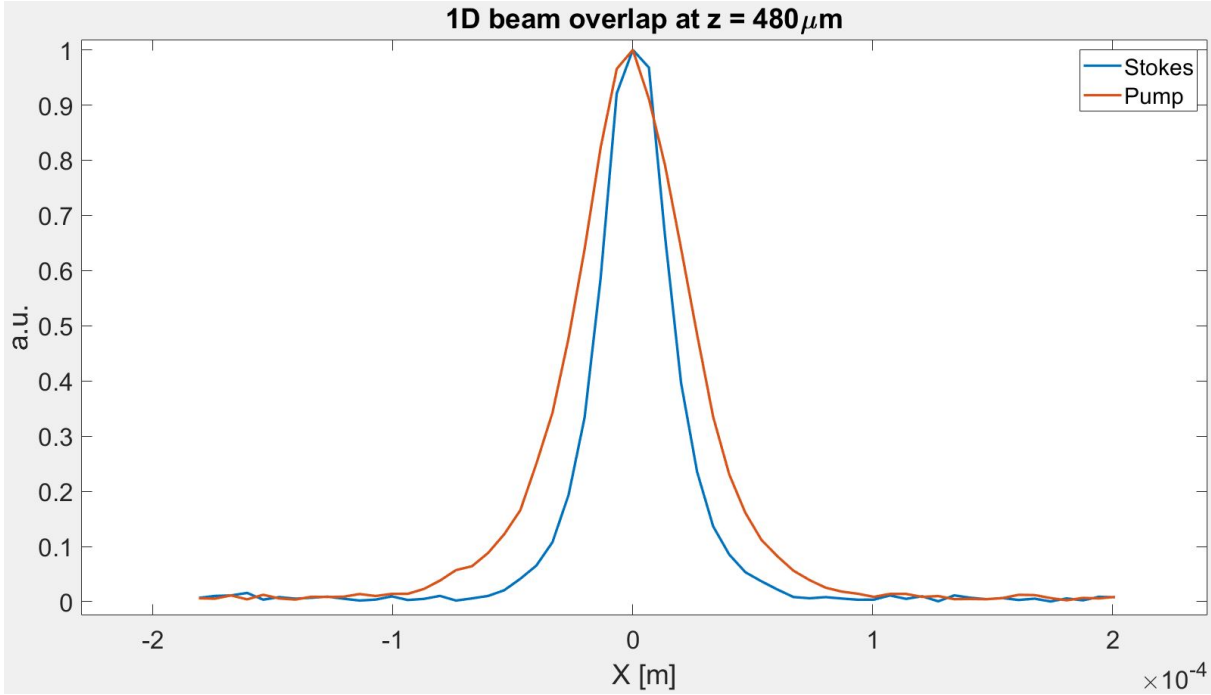


Figure 4.8: 1D profiles of the beams. We can observe how they are well spatially overlapped, but also their different widths. Beam profiles of images acquired at  $480\mu\text{m}$  away from the focus.

a value between 0 and  $(2^{16} - 1)$ . Physically, this value represents a **relative** measure of power. For example, if we send a  $100\mu\text{W}$  beam to the profiler and a specific pixel accounts for 10% of the total pixel sum, this implies that on this pixel are arrived  $10\mu\text{W}$ . So this is the link between pixel value and power. If we want now to achieve the photon flux, we should take into account also the photon energy  $hc/\lambda n_{mat}$  and the pixel area  $A_{pixel}$ . The complete link is

$$\Phi(x, y, z) = \frac{S(x, y, z) \cdot \left( \frac{P\lambda n_{mat}}{hcA_{pixel}} \right)}{\sum_{xy} S(x, y, z)} \quad (4.6)$$

For the calculations it is important to consider a correct number of pixels from the image. The camera is made of  $1024 \times 1280$  pixels, while the beam is always contained in around 50-100 pixels. This means that the large majority of pixels are made of just background noise. Considering all the pixels would spread the power along all of them. Even if the value produce by the noise is much smaller than the ones where the beams is present, the huge number of black pixels would reduce by lot the power really present in the beam. For this reason, the during the images processing we used a circular mask(Fig. 4.7) to cut away the black pixels leaving just a small arbitrary number of pixels to consider. Anyway to further improve the results, in the data processing we removed the background from the remaining pixels, by subtracting the mean value of a region with just black pixels.

The relative nature of the beam profile map also allows us to use different power levels for the beam profiler compared to the power in the actual experiment, as the spatial distribution of intensity stays the same. This flexibility provides two main benefits. First, it makes it possible to use the beam profiler safely, without risking damage from the experimental high pump power. Second, it allows us to adjust the power level for each z-plane map, which helps improve the accuracy of measurements. To illustrate why this is useful, imagine what would happen keeping a fixed along the z acquisition. At the focus, where intensity is highest, the values in the pixels directly hit by the beam are high in comparison to the background. This results in a clear map of the beam shape, capturing most of the beam structure with only slight loss at the edges. However, as we move the profiler further from the focus, the beam spreads out and intensity drops across more pixels, each one seeing a weaker signal. This reduced intensity can make it harder to accurately capture the shape of the beam, especially further from the focus, where more details might be lost in the background noise. So before acquiring each map we changed the power arriving onto the camera, in order to stay close to saturation each time. A final practical consideration. The beam profile acquired by camera, so in the air, is for sure different, due to Fresnel laws, from the one that is really inside the sample. Thanks to the fact that our system does not focus the beam too tightly, the angle with whom the beam enters the sample is very small. Therefore the variation introduced by fresnel law can be neglected. To be more precise we extracted for each map the beam waist, this by performing a gaussian fit to the 1D beam profile (Fig. 4.8). Those profiles were obtained by the summation of the pixel value along the columns. From those beam waist values, we retrieved the entering angle. It turns out that the entering angle for both beams is smaller than 1 degree.

## Formula used

We pass now to the final formula used to retrieve the SRS cross-section inserting equation (4.6) into (4.5). In a natural way we substituted the integral with a summation since the distribution acquired are discrete.

$$\left(\frac{\Delta I}{I}\right)_{SRG} = [c]N_a\sigma_{SRS} \frac{\sum_z \left[ \sum_{x,y} \left( \frac{S_p(x,y,z) \cdot \left(\frac{P_p \lambda_p n_{mat}}{hc A_{pixel}}\right)}{\sum_{xy} S_p(x,y,z)} \right) \cdot \left( \frac{S_s(x,y,z) \cdot \left(\frac{P_s \lambda_s n_{mat}}{hc A_{pixel}}\right)}{\sum_{xy} S_s(x,y,z)} \right) A_{pixel} \right] \Delta z}{\left(\frac{P_s \lambda_s n_{mat}}{hc}\right)} \quad (4.7)$$

At this point we can cancel out some terms relative to the Stokes. Note that the results is still independent on the Stokes power but just on the pump one. Regarding the pump we should consider also here the peak power instead of the simple average power. The two are linked by  $P_{peak} = P_{ave}/\tau RR$  where  $\tau$  is the pump pulse duration and  $RR$  is the laser repetition rate. Additionally we must consider the transmittance, so the power losses, between media. We have a transmission  $T_1 = 96\%$  between air and glass, and a transmittance  $T_2 = 99.6\%$  between glass and methanol. Bringing out of the constant terms the formula become

$$\left(\frac{\Delta I}{I}\right)_{SRG} = \left(\frac{[c]N_a\sigma_{SRS}P_{p,ave}T_1T_2\lambda_p n_{mat}}{\tau_p RR hc A_{pixel} A_{pixel}}\right) \cdot \sum_z \left[ \sum_{x,y} \left( \frac{S_p(x,y,z)}{\sum_{xy} S_p(x,y,z)} \right) \cdot \left( \frac{S_s(x,y,z)}{\sum_{xy} S_s(x,y,z)} \right) A_{pixel} \right] \Delta z \quad (4.8)$$

We decided to not cancel out  $A_{pixel}$  to explicitly show the correct unit of measure to use. At the numerator  $A_{pixel}$  is in  $dm^2$  and  $\Delta z$  in  $dm$ . This to have at the numerator a volume in  $dm^3$  and so in  $L$ . This is important since the concentration  $[c]$  is given in  $mol/L$ . The two  $A_{pixel}$  at the denominator instead are in  $cm^2$  since the  $\sigma_{SRS}$  is expressed in  $GM$  that is equal to  $10^{-50} \cdot cm^4 \cdot s$ .

After isolating  $\sigma_{SRS}$ , the resulting expression aligns closely with equation (2.62), as expected. The main distinction appears in the spatial component, where  $A^2/V$  is replaced by the summation term that reflects the beam's spatial distribution.

### 4.3.2. Temporal distribution

The starting procedure is the same followed for the spatial distribution. We arrive to an equation very similar (4.5) where now we take into account also the temporal dependence of the pulse. Since the photon flux is proportional to the intensity, assuming a gaussian

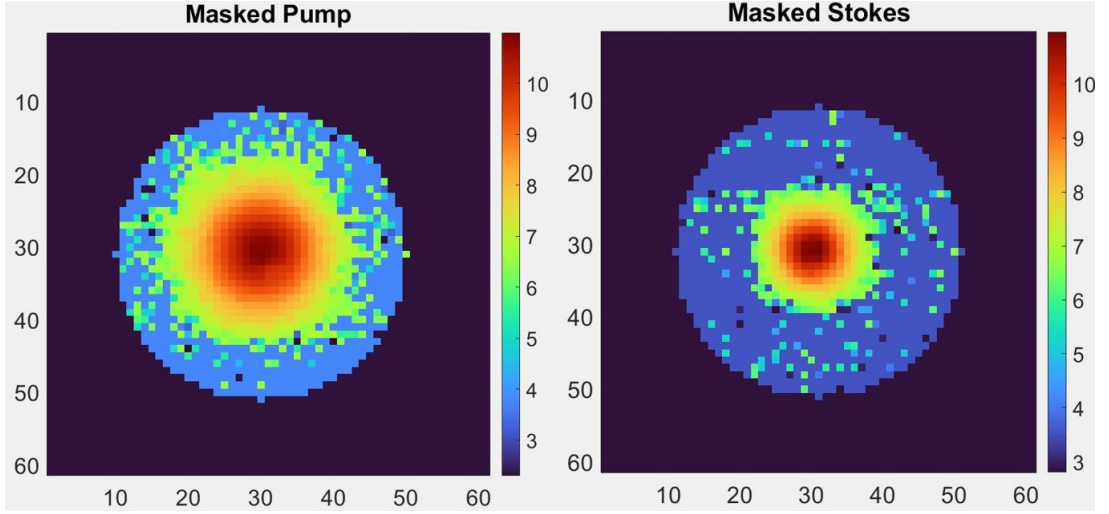


Figure 4.9: Logarithmic representation of the images acquired by the beam viewer, after the application of a circular mask

temporal profile for the pulse, we can write

$$\beta(x, y, z, t) = \Phi(x, y, z) \exp(-t^2/2\tau^2) \quad (4.9)$$

Where  $\tau$  is the pulse width. The only difference with equation (4.5) is that, before we started imposing  $\Delta I/I$  equal to the ratio between the number of photons per second generated by SRG and the number of photons per second arriving from the Stokes (equation (2.61)). Now in the right hand side, we put the ration between the number of photons generated by SRG in a single pulse and the number of photons arriving from the Stokes in a single pulse. To consider the number of photons in a pulse instead of the number of photon per second is necessary a temporal integration.

$$\begin{aligned} \left(\frac{\Delta I}{I}\right)_{SRG} &= \\ &= \frac{\int_t \text{rate}_{SRS} dt}{\int_t \Phi_s A dt} \end{aligned} \quad (4.10)$$

$$= [c] N_a \sigma_{SRS} \int_z \left( \frac{\int_t \int_x \int_y \beta_p(x, y, z, t) \beta_s(x, y, z, t) dt dx dy}{\int_t \int_x \int_y \beta_s(x, y, z, t) dt dx dy} \right) dz \quad (4.11)$$

Where  $\int_t()dt$  is the temporal integration over a single pulse. Since in our simplified case the temporal dependence is separated from the spatial one, we can modify the equation

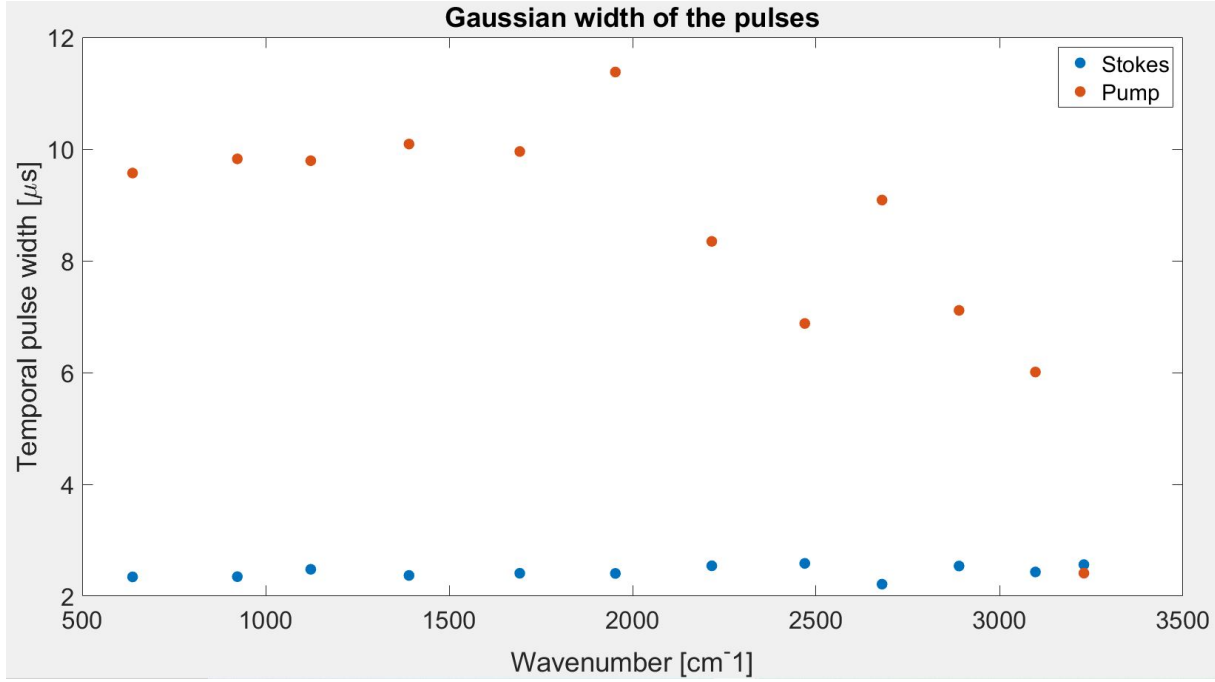


Figure 4.10: Temporal pulse duration assuming a gaussian profile in function of the wavenumbers. Data provided by the laser producer (Refined Laser System).

writing

$$\left(\frac{\Delta I}{I}\right)_{SRG} = [c]N_a\sigma_{SRS} \int_z \left( \frac{\int_x \int_y \Phi_p(x, y, z)\Phi_s(x, y, z)dxdy}{\int_x \int_y \Phi_s(x, y, z)dxdy} \right) dz \cdot \frac{\int_t \exp(-(t^2/2\tau_p^2)) \cdot \exp(-(t^2/2\tau_s^2))dt}{\int_s \exp(-(t^2/2\tau_s^2))} \quad (4.12)$$

The formula is exactly the same as equation(4.5) except for and additional term

$$K_1 \equiv \frac{\int_t \exp(-(t^2/2\tau_p^2)) \cdot \exp(-(t^2/2\tau_s^2))dt}{\int_s \exp(-(t^2/2\tau_s^2))} \quad (4.13)$$

From now on the mathematical development is the same arriving to equation (4.8) with the additional term  $K_1$ .

In our case we did not directly measure the temporal length of the pulse but we trusted the data directly provided by laser producers, measured on our laser Fig. 4.10.

At this point we have done two assumption: the first regards the temporal width of the pump. The data provided are just of 12 wavenumbers. Fortunately around  $1033\text{cm}^{-1}$  the pulse width seems to be quite steady. For this reason we considered the average value

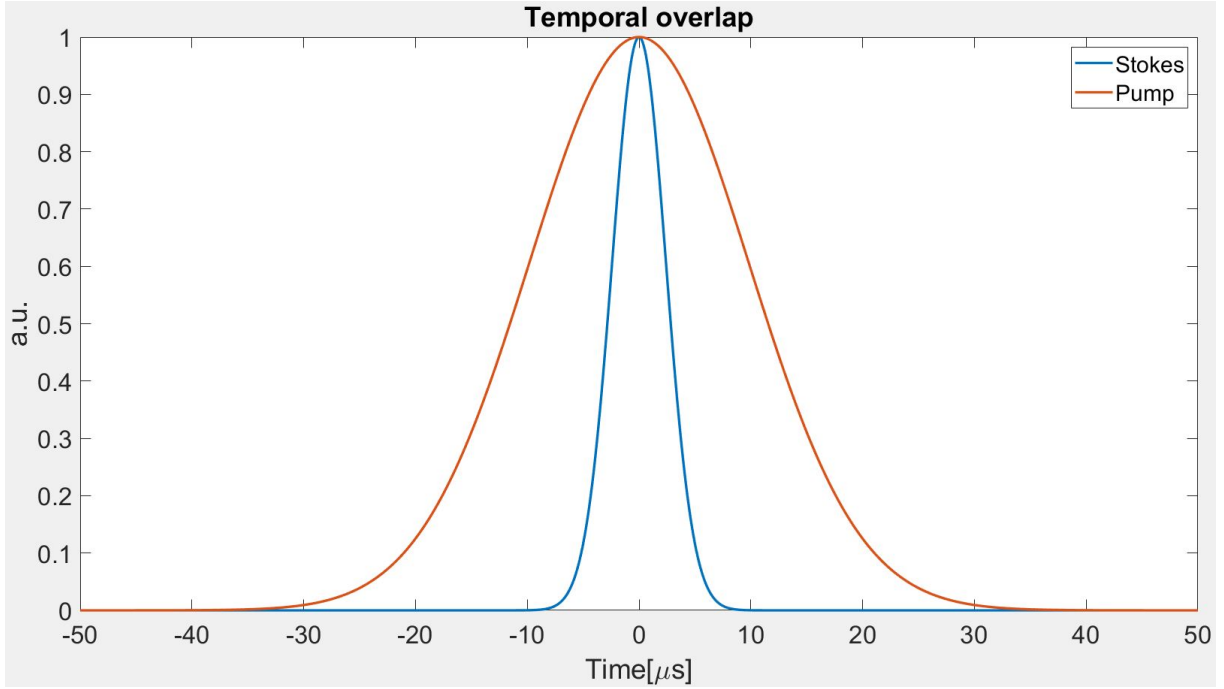


Figure 4.11: Temporal overlap setting  $\Omega = 1033 \text{ cm}^{-1}$  between the two pulses assuming a gaussian profile and perfect overlap.

between the two nearest point around  $1033 \text{ cm}^{-1}$ . This gave us a temporal width for the pump of  $\tau_p = 9.81 \mu\text{s}$  and for the Stokes  $\tau_s = 2.41 \mu\text{s}$ . The second assumption is the perfect overlap. As we said previously we looked for the best  $\Delta I$  signal in order to achieve the best temporal overlap, but except for this we could not look directly at it, so we assumed to have reached the perfect overlap between the two.

The calculus of  $K_1$  is quite simple since we are using perfect gaussian. We start from the well known result

$$\int_t \exp(-(t^2/2\tau^2)) dt = \sqrt{2\pi\tau^2} \quad (4.14)$$

At the numerator the product of two gaussian can be seen as a single gaussian with variance  $\tau_{num}^2 = \left(\frac{1}{\tau_p^2} + \frac{1}{\tau_s^2}\right)^{-1}$ . Note how this formula as the same expression of a reduced mass. This means

$$K_1 = \frac{\sqrt{2\pi\tau_{num}^2}}{\sqrt{2\pi\tau_s^2}} = \frac{1}{\sqrt{\tau_s^2 \cdot \left(\frac{1}{\tau_p^2} + \frac{1}{\tau_s^2}\right)}} = 0.97 \quad (4.15)$$

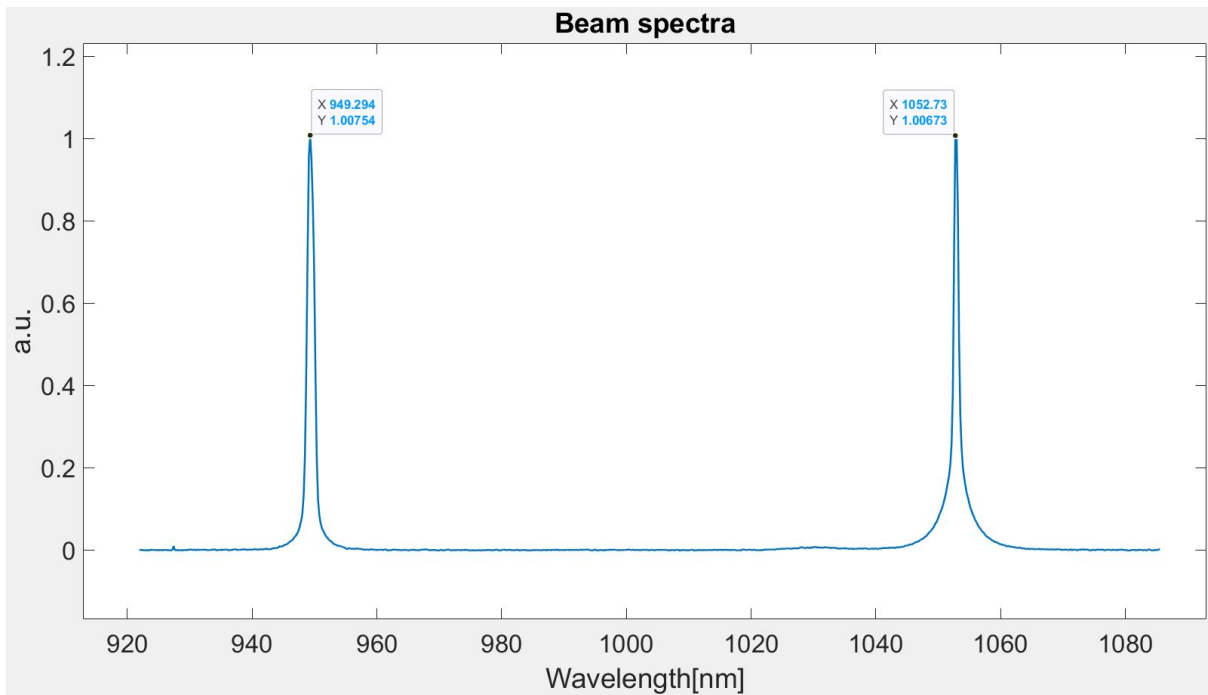


Figure 4.12: The pump(left) and Stokes(right) acquired with a spectrometer. We can observe how the beam spectra are centered at the nominal central frequency.

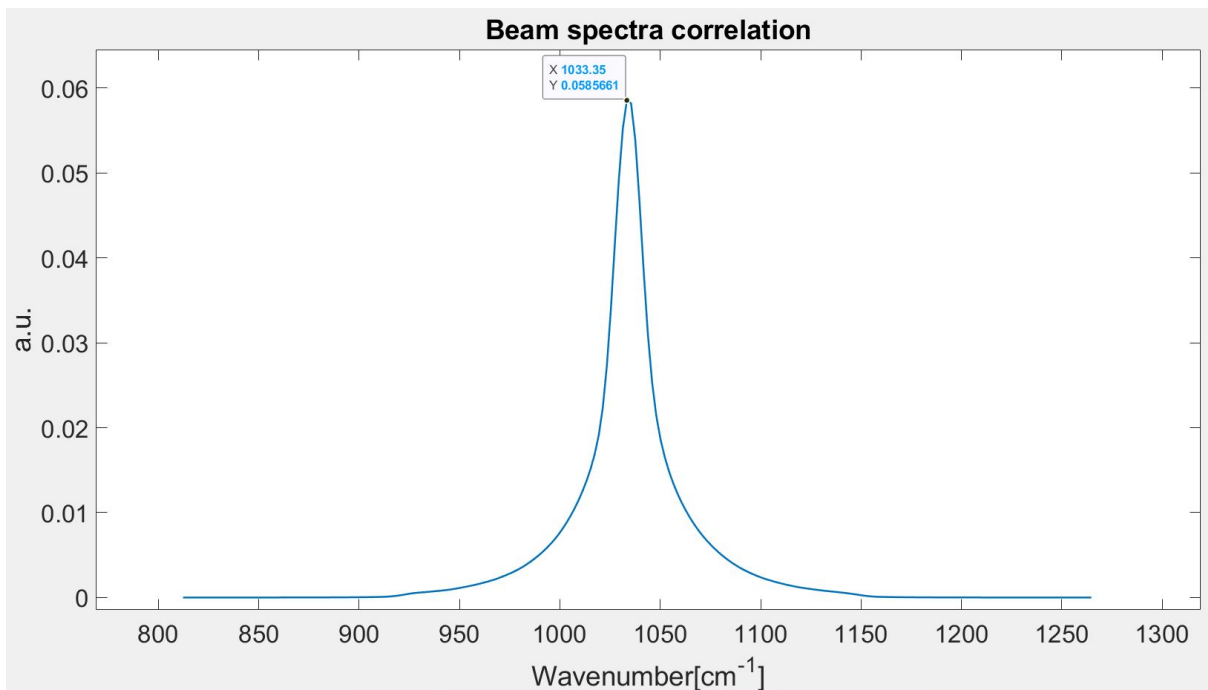


Figure 4.13: Spectral correlation between the pump and the Stokes centered at  $\Omega = 1033\text{cm}^{-1}$

### 4.3.3. Spectral distribution

We now also consider the spectral distribution of the beams. In an ideal scenario where the beam spectra are delta functions at  $\omega_p$  and  $\omega_s$ , we could accurately retrieve  $\Omega = \omega_p - \omega_s$ . However, the spectra are not ideal delta functions; instead, they are typically Gaussian functions centered at  $\omega_p$  and  $\omega_s$  with a finite width. This implies that, in addition to the target frequency  $\Omega$ , all possible frequency differences generated by the various combinations of frequencies within these Gaussian distributions are also excited. We should introduce an additional corrective factor,  $K_2$ , which multiplies the right-hand side of equation (4.5) to account for the fact that the measured value is not the actual  $\sigma_{SRS}(\Omega)$ , but rather an approximation. Specifically, the measured value represents the integral of the true Raman spectrum and the correlation between the spectra of the two beams. In Fig. 4.14, we can clearly observe how the correlation between the pump and Stokes spectra, overlap almost all the vibration peak, in contrast to the ideal scenario where a delta function would be involved.  $K_2$  is nothing more than the ratio between the measured value and the true  $\sigma_{SRS}(\Omega)$ . This substitution allows us to concretely replace  $\sigma_{SRS}(\Omega)$  in (4.5) with the measured value but practically retaining the same formulation, simply by adding a multiplicative term. For this reason what

$$K_2 \equiv \frac{\int_{\theta} \sigma_{SRS}(\theta) \cdot C(\theta) d\theta}{\sigma_{SRS}(\Omega)} \quad (4.16)$$

where  $C(\theta)$  is the correlation between pump and Stokes spectra. Naturally in practice for  $K_2$  we do not need the real value of  $\sigma_{SRS}(\theta)$  that is our final aim. It is sufficient to have an arbitrary unit spectrum  $S(\theta)$  and put at denominator its value when  $\theta = \Omega$ . To obtain  $S(\theta)$  it is very useful the spontaneous Raman since it gives, in arbitrary unit, the precise shape of the Raman spectrum. About the correlation  $C(\theta)$  is important to have its area normalized to 1. In fact we could see the denominator as the integral of  $S(\theta)$  times the ideal deltas correlation with amplitude, and so area for a delta, equal to 1. From the calculation the value of  $K_2$  is 0.548.

### 4.3.4. Results and considerations

We can finally unify all the elements considered going to multiply the right hand side of equation (4.8) with  $K_1$  and  $K_2$ . We proceed isolating the  $\sigma_{SRS}$  achieving the final formula

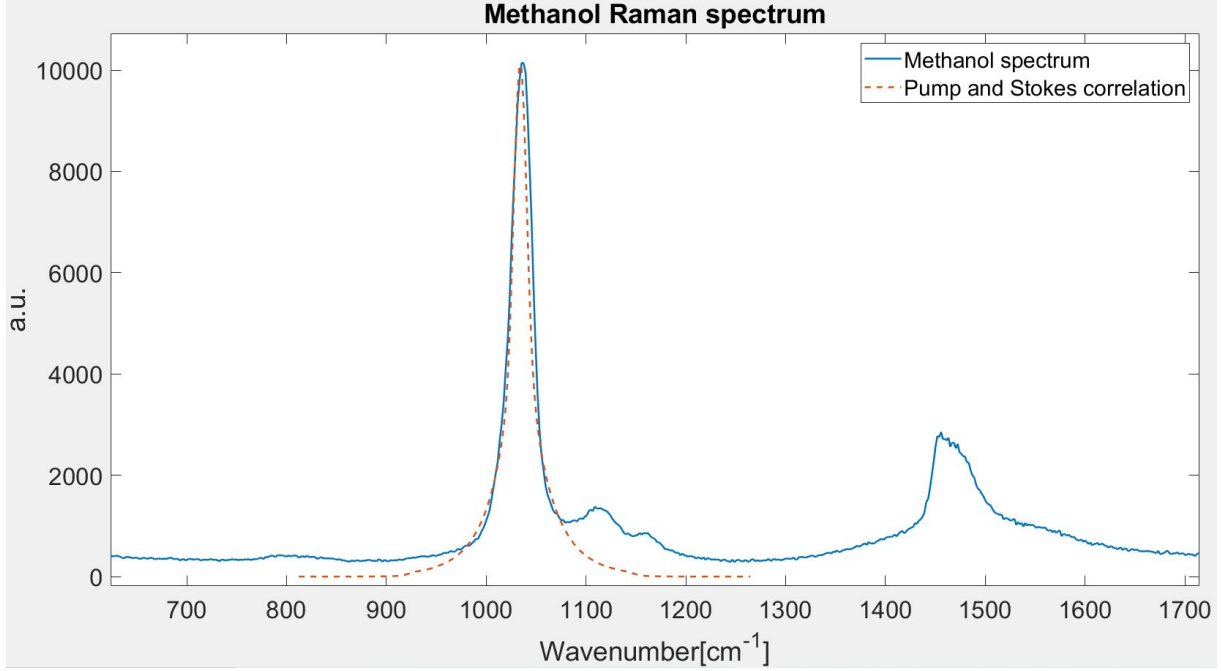


Figure 4.14: Raman spectrum of the methanol. The orange dashed line represent the spectral correlation.

used.

$$\sigma_{SRS} = \left( \frac{\Delta I}{I} \right)_{SRG} \cdot \left( \frac{\tau R R h c A_{pixel} A_{pixel}}{[c] N_a P_{p,ave} T_1 T_2 \lambda_p n_{mat} K_1 K_2} \right). \quad (4.17)$$

$$\cdot \left( \sum_z \left[ \sum_{x,y} \left( \frac{S_p(x,y,z)}{\sum_{xy} S_p(x,y,z)} \right) \cdot \left( \frac{S_s(x,y,z)}{\sum_{xy} S_s(x,y,z)} \right) A_{pixel} \right] \Delta z \right)^{-1} \quad (4.18)$$

Inserting all data, we obtain from the calculation a value for the  $\sigma_{SRS} = 0.367 \text{ GM}$ . In the previous paper [9, 16] they achieved a numerical value of  $0.04 \text{ GM}$ . The difference comes from, looking at equation (4.18), the different values at the denominator for  $K_1$ ,  $K_2$  and the spatial summation. As also previously stated they used an approximated version, in particular:

- In the spatial domain the pulses are uniform squares: canceling of  $\Phi_s$
- In the temporal domain the pulses are uniform squares:  $K_1 = 1$
- The beam spectra are perfect deltas:  $K_2 = 1$

All those factors lead to a bigger denominator and consequently to a bigger value for  $\sigma_{SRS}$ . We also performed a calculation with the standard formula (2.65) using as volume

a simple cylinder, with a radius equal to the mean value (along  $z$ ) of the beam waist. In this way we retrieved a value  $\sigma'_{SRS} = 0.055 GM$ . This value is slightly different from  $0.04 GM$  but probably just for the incorrect volume considered, anyway using the same approach and approximation we retrieved the same result.



## Conclusions and future perspectives

This master thesis focuses on advancing the quantitative measurement of Stimulated Raman Scattering (SRS). In the first part, it explores the necessity of the newly introduced parameter, the Filling Factor (FF), to calibrate the  $\Delta I/I$  value. The second part regards the calibration of a recently proposed parameter, the SRS cross-section  $\sigma_{SRS}$ . The significance of this work lies in the measure of a universal parameter capable of describing the material SRS response, considering all the perturbations introduced by the measurement process itself. The first part of the thesis highlights the role of the Filling Factor in calibrating  $\sigma_{SRS}$ , but it is crucial to note that FF has broader applications beyond SRS. It applies more generally to lock-in amplifier measurements. For instance, FF could also be used to calibrate the Relative Intensity Noise (RIN) when measured with a lock-in amplifier. In such cases, normalization with respect to laser power, as in  $\Delta I/I$ , remains essential to avoid underestimating noise levels. In the second part, regarding the spatial aspects, some might argue that the summation volumes used for calibration ( $A_{pixel} \cdot \Delta z$ ) are larger than the typical focal volume in SRS, potentially reducing precision. However, the purpose of this approach is not to achieve higher resolution but to directly visualize how the two beams are spatially distributed and overlap, a task impossible in small volumes. Temporal aspects could be improved in future work. In this study, we used laser manufacturer data, assuming a Gaussian temporal profile with perfect overlap. The next step would involve directly measuring the temporal profiles of the two beams, perhaps using an autocorrelator, to calculate the corrective factor  $K_1$  more accurately. For the spectral component, the current procedure appears satisfactory and aligns with established methods.

The numerical results offer valuable insights. The variations in numerical values arise from the fact that our procedure accounted for the characteristics of the pulses to derive a  $\sigma_{SRS}$  value that depends only on the material being studied, rather than the specific setup employed. While there is room for improvement in the experimental setup, we are satisfied with the results obtained, especially given the alignment of values when similar methodologies were applied.

One practical application of SRS, considering its 3D sectioning capability, is reconstruct-

ing material concentration maps. Such imaging is valuable in fields like diagnostics, pharmaceuticals, material science, and quality control. The introduction of an absolute SRS cross-section enhances precision in these measurements and ensures more accurate proportions between the concentrations of different material components. This leads to higher-quality images and improved evaluations across those fields.

## Bibliography

- [1] M. Andreana, M.-A. Houle, D. J. Moffatt, A. Ridsdale, E. Buettner, F. Légaré, and A. Stolow. Amplitude and polarization modulated hyperspectral stimulated raman scattering microscopy. *Optics express*, 23(22):28119–28131, 2015.
- [2] R. W. Boyd, A. L. Gaeta, and E. Giese. Nonlinear optics. In *Springer Handbook of Atomic, Molecular, and Optical Physics*, pages 1097–1110. Springer, 2008.
- [3] R. Bracewell and P. B. Kahn. The fourier transform and its applications. *American Journal of Physics*, 34(8):712–712, 1966.
- [4] J.-X. Cheng and X. S. Xie. *Coherent Raman scattering microscopy*. CRC press, 2016.
- [5] J.-X. Cheng, W. Min, Y. Ozeki, and D. Polli. *Stimulated Raman scattering microscopy: Techniques and applications*. Elsevier, 2021.
- [6] E. A. Donley, T. P. Heavner, F. Levi, M. Tataw, and S. R. Jefferts. Double-pass acousto-optic modulator system. *Review of Scientific Instruments*, 76(6), 2005.
- [7] K. G. E. Der Smekal-Raman-Effekt. *Nature*, 128(3242):1026–1026, 1931.
- [8] J. W. Fleming and C. S. Johnson Jr. A practical analysis for coherent anti-stokes raman scattering (cars) spectra. *Journal of Raman Spectroscopy*, 8(5):284–290, 1979.
- [9] X. Gao, X. Li, and W. Min. Absolute stimulated raman cross sections of molecules. *The Journal of Physical Chemistry Letters*, 14(24):5701–5708, 2023.
- [10] M. Goppert-Mayer. Uber elementarakte mit zwei quantensprungen. *Ann. Phys.*, 9: 273–295, 1931.
- [11] R. Hellwarth. Third-order optical susceptibilities of liquids and solids. *Progress in Quantum Electronics*, 5:1–68, 1977.
- [12] W. Kaiser and C. Garrett. Two-photon excitation in ca f 2: Eu 2+. *Physical review letters*, 7(6):229, 1961.
- [13] M. S. Keshner. 1/f noise. *Proceedings of the IEEE*, 70(3):212–218, 1982.

- [14] Y. Li, B. Shen, S. Li, Y. Zhao, J. Qu, and L. Liu. Review of stimulated raman scattering microscopy techniques and applications in the biosciences. *Advanced Biology*, 5(1):2000184, 2021.
- [15] J. Mammone, S. Sharma, and M. Nicol. Raman spectra of methanol and ethanol at pressures up to 100 kbar. *The Journal of Physical Chemistry*, 84(23):3130–3134, 1980.
- [16] W. Min and X. Gao. Raman scattering and vacuum fluctuation: An einstein-coefficient-like equation for raman cross sections. *The Journal of Chemical Physics*, 159(19), 2023.
- [17] W. Min and X. Gao. The duality of raman scattering. *Accounts of Chemical Research*, 57(14):1896–1905, 2024.
- [18] Y. Ozeki, Y. Kitagawa, K. Sumimura, N. Nishizawa, W. Umemura, S. Kajiyama, K. Fukui, and K. Itoh. Stimulated raman scattering microscope with shot noise limited sensitivity using subharmonically synchronized laser pulses. *Optics express*, 18(13):13708–13719, 2010.
- [19] C. V. Raman and K. S. Krishnan. A new type of secondary radiation. *Nature*, 121(3048):501–502, 1928.
- [20] H. Rigneault and P. Berto. Tutorial: Coherent raman light matter interaction processes. *Apl Photonics*, 3(9), 2018.
- [21] A. Smekal. Zur quantentheorie der dispersion. *Naturwissenschaften*, 11(43):873–875, 1923.
- [22] A. Volkmer. Coherent raman scattering microscopy. *Emerging Raman Applications and Techniques in Biomedical and Pharmaceutical Fields*, pages 111–152, 2009.
- [23] M. Young. Principles and technique of fluorescence microscopy. *Journal of Cell Science*, 3(60):419–449, 1961.
- [24] C. Zhang and J. A. Aldana-Mendoza. Coherent raman scattering microscopy for chemical imaging of biological systems. *Journal of Physics: Photonics*, 3(3):032002, 2021.
- [25] W. R. Zipfel, R. M. Williams, and W. W. Webb. Nonlinear magic: multiphoton microscopy in the biosciences. *Nature biotechnology*, 21(11):1369–1377, 2003.

# A | Appendix A: FF independence on modulated over total amplitude

The signal entering the photodiode ( $S(t)$ ) can be seen as the summation of two terms, the modulated part ( $M(t)$ ) and the pedestal ( $P(t)$ ):

$$M(t) = A \cos(\omega t) \cdot \sum_{n=-\infty}^{+\infty} \delta(t - n\tau) = A \cdot \sum_{n=-\infty}^{+\infty} \cos[\omega(t - n\tau)] \quad (\text{A.1})$$

$$P(t) = B \cdot \sum_{n=-\infty}^{+\infty} \delta(t - n\tau) \quad (\text{A.2})$$

$$S(t) = M(t) + P(t) \quad (\text{A.3})$$

where  $\tau$  is the inverse of the laser repetition rate. We assumed the laser pulses as deltas considering the not sufficient bandwidth of the photodiode.

The output of the photodiode, and so the signal entering the lock-in ( $LI(t)$ ), is the convolution between  $S(t)$  and the photodiode pulse response ( $h(t)$ ).

$$LI(t) = S(t) * h(t) = A \cdot \sum_{n=-\infty}^{+\infty} \cos[\omega(t - n\tau)] \cdot h(t - n\tau) + B \cdot \sum_{n=-\infty}^{+\infty} h(t - n\tau) \quad (\text{A.4})$$

The Filling Factor ( $FF$ ) is the ratio between the lock-in output ( $LO(t)$ ) and the peak-to-peak modulation amplitude ( $2A$ ).

The lock-in operation cuts away the second term of  $LI(t)$ . Precisely keeps just the  $\omega$

component of  $h(t)$  but it can be neglected. The first term of  $LI(t)$  instead gives rise to

$$LO(t) = \int_{-\tau_{LPF}}^{+\tau_{LPF}} A \cdot \left[ \sum_{n=-\infty}^{+\infty} \cos[\omega(t - n\tau)] \cdot h(t - n\tau) \right] \cdot \cos(\omega t) dt \quad (\text{A.5})$$

where we assumed, without loss of generality, the same phase for the modulating and demodulating signals, and approximated the LPF operation as an integration inside a temporal window wide as its time constant. The FF is therefore

$$FF = \frac{LO(t)}{2A} = \frac{\int_{-\tau_{LPF}}^{+\tau_{LPF}} \left[ \sum_{n=-\infty}^{+\infty} \cos[\omega(t - n\tau)] \cdot h(t - n\tau) \right] \cdot \cos(\omega t) dt}{2} \quad (\text{A.6})$$

As we can see the Filling Factor is independent on both A and B, but just depends on  $\omega$  and  $h(t)$ .

## List of Figures

1.1	Raman spectrum of a single cell of human primary glioblastoma U87 cell line. The different highlighted regions shows the cell components. . . . .	2
1.2	Cross-sections of spontaneous Raman scattering (in and off resonance) and linear absorption (IR and UV) for various molecules and bond. The difference in strength between the two process is easily observable. [9] . . . . .	3
1.3	Different Raman processes in Jablonski representation.a) Spontaneous Raman off-resonance b)Spontaneous Raman on-resonance c) Stimulated Raman Scattering d) Coherent Anti-Stokes Raman Scattering . . . . .	4
2.1	A body with mass $m$ attached to a spring with stiffness $k$ in presence of the gravitational acceleration $g$ . . . . .	7
2.2	Damped forced harmonic oscillator close to resonance. a) Representation in the complex plane of $x$ b) Amplitude of $x$ ( $\rho$ ) in function of $\omega$ c) Phase of $x$ ( $\phi$ ) in function of $\omega$ d) Time domain description of the three regimes: below, at, and above resonance [5] . . . . .	9
2.3	Representation of three vibrational modes of $H_2O$ with their respective wavenumber and wavelength.[5] . . . . .	10
2.4	Schematization of a simple diatomic molecule. . . . .	11
2.5	Angular frequency dependance of $\chi^{(1)}$ . a) Representation in the complex plane b) The real part of $\chi^{(1)}$ linked to the material dispersion c) The imaginary part of $\chi^{(1)}$ linked to the material absorption[5] . . . . .	13
2.6	Relationship between the incident electric field and induced polarization. With weak electric fields (illustrated by the black sinusoidal line), only the harmonic part of the potential is significant, resulting in polarization that is directly proportional to the field. As the field strength increases (shown by the gray sinusoidal line), the anharmonic components of the potential begin to play a role, causing the polarization to respond nonlinearly to the applied field. In this regime, the polarization profile no longer follows the sinusoidal shape of the incoming field. [4] . . . . .	15

2.7	jablonski representatio of a)Rayleigh Scattering b)Stokes Raman Scattering c)Anti-Stokes Raman Scattering . . . . .	16
2.8	Representation of the CRS processes in the spectral domain. The dotted lines represent the intensity variation due to the SRS processes. . . . .	22
2.9	Comparison of $\sigma_{TPA}$ and $\sigma_{SRS}$ under the common GM framework. We can note how the two share a large window of value contrarily to their spontaneous counterpart [9] . . . . .	27
3.1	Lock-in operation in the spectrum domain. Note that also the negative frequencies are considered. a) Spectrum representation of $V_{in}$ b) Signal after the multiplication for the reference one ( $X'$ ) c) LPF action d) Output of the lock-in ( $X$ ) . . . . .	33
3.2	Typical shape of $1/f$ noise in frequency domain. We can note how in the low frequency region the noise increases, contrarily to the white noise that remains constant everywhere. [13] . . . . .	34
3.3	Scheme of the pulses intensities in a modulated SRG process. . . . .	34
3.4	a) $S(t)$ . We can see the train of $h(t)$ with the small modulation b) The <i>filled</i> signal. Is the modulation signal raised by a pedestal c) The action of a LPF that transform a delta into is pulse response $h(t)$ . . . . .	36
3.5	Set-up implied for the FF measurements. BS = Beam Splitter. . . . .	37
3.6	The OE-300-SI-30 photodiode. We can observe the different gains and relative bandwidth . . . . .	39
3.7	Oscilloscope track in the case of 100 MHz BW and 97% ratio . . . . .	42
3.8	Oscilloscope track in the case of 100 MHz BW and 72% ratio . . . . .	43
3.9	Oscilloscope track in the case of 100 MHz BW and 46% ratio . . . . .	43
3.10	Oscilloscope track in the case of 100 MHz BW and 1.25% ratio . . . . .	44
3.11	Modulation shape of the 100 MHz BW at 97% retrieved with peaks method	45
3.12	Image of just the pedestal where we can observe an intrinsic modulation coming from the laser . . . . .	45
3.13	Oscilloscope track in the case of 100 MHz BW and 97% ratio . . . . .	47
3.14	Oscilloscope track in the case of 100 MHz BW and 72% ratio . . . . .	48
3.15	Oscilloscope track in the case of 100 MHz BW and 46% ratio . . . . .	48
3.16	Oscilloscope track in the case of 100 MHz BW and 1.25% ratio . . . . .	49
3.17	Oscilloscope track in the case of 100 MHz BW and 97% ratio . . . . .	50
3.18	Oscilloscope track in the case of 100 MHz BW and 72% ratio . . . . .	51
3.19	Oscilloscope track in the case of 100 MHz BW and 46% ratio . . . . .	51
3.20	Oscilloscope track in the case of 100 MHz BW and 1.25% ratio . . . . .	52

4.1	Set-up implied for the SRS measurements. $\lambda/2$ = half wave plate, PBS = Polarized Beam Splitter, FELH-1000 = High performance long-pass filter from 1000 nm, L = lens. . . . .	56
4.2	Picus software used to control the various parameters like wavenumber and delay	58
4.3	FELH-1000 transmission in function of the wavelength. The blue shaded region in the graph represents the transmission region of the filter, 1013 – 2150nm. Image acquired from Thorlabs website. . . . .	59
4.4	Schematic representation of the phase lock operation. The signal with random phase $\theta$ is brought on the X axis. . . . .	59
4.5	Calibrated $\Delta I/I$ spectrum of methanol . . . . .	62
4.6	Emitted pump power in function of the wavenumber . . . . .	62
4.7	Beam profiler maps of Pump (left) and Stokes (right). Images are taken with power just below saturation. The higher value in the pixels are around 65000 ( $2^{16}$ ). Images acquired at $480\mu m$ away from the focus. . . . .	65
4.8	1D profiles of the beams. We can observe how they are well spatially overlapped, but also their different widths. Beam profiles of images acquired at $480\mu m$ away from the focus. . . . .	66
4.9	Logarithmic representation of the images acquired by the beam viewer, after the application of a circular mask . . . . .	69
4.10	Temporal pulse duration assuming a gaussian profile in function of the wavenumber. Data provided by the laser producer (Refined Laser System). . . . .	70
4.11	Temporal overlap setting $\Omega = 1033\text{ cm}^{-1}$ between the two pulses assuming a gaussian profile and perfect overlap. . . . .	71
4.12	The pump(left) and Stokes(right) acquired with a spectrometer. We can observe how the beam spectra are centered at the nominal central frequency. . . . .	72
4.13	Spectral correlation between the pump and the Stokes centered at $\Omega = 1033\text{ cm}^{-1}$	72
4.14	Raman spectrum of the methanol. The orange dashed line represent the spectral correlation. . . . .	74



## List of Tables

3.1	Data for the 100 MHz photodiode bandwidth . . . . .	41
3.2	Data for the 14 MHz photodiode bandwidth . . . . .	46
3.3	Data for the 1.8 MHz photodiode bandwidth . . . . .	46

